Westfälische
Wilhelms-Universität
Münster

INSTITUT FÜR KERNPHYSIK

Bachelor Thesis

Characteristics of the Pixirad Detector

Johannes Beckhoff

First Supervisor: Prof. Dr. J. P. Wessels
Second Supervisor: Dr. Cyrano Bergmann

— September 2016 —

Contents

List of Figures

List of Tables

Introduction

The Compressed Baryon Matter experiment (CBM) at the FAIR in Darmstadt uses high energy nucleus-nucleus collisions researching the phase space of the strong interaction of matter, among others the Quark-Gluon Plasma in the region of high baryon densities. For these investigations several detectors are used, such as the CBM Transition Radiation Detector (TRD). As the name implies, the TRD uses transition radiation to detect high energetic particles. If a high relativistic particle transits layers of different permittivities, it emits electromagnetic radiation, which can be detected by a multi-wire proportional chamber (MWPC) afterwards. Because the intensity of the radiation is linearly dependent on the Lorentz factor $\gamma = \frac{E}{mc^2}$, the mass and therefore, knowing the particle energy, the type of the particle can be identified. Furthermore, the track of a particle can be reconstructed with many of these layers. [1]
A MWPC consists of multiple layers with parallel wires of high voltage surrounded by gas. These layers work in the same way as a proportional counter. If a particle passes the chamber, it ionises the gas. The resulting ions are attracted by the nearest wire and generate a current pulse which can be detected individually for each wire. Another option is to detect the current pulse by a segmented cathode pad-plane. This method is used at the CBM-TRD. The track and the energy of the ionising particles can be identified by many of these layers.
Altogether, the track and the identity of a particle can be specified by an arrangement of both presented detectors.

In order to receive a reference measurement of the original particle beam, another, commercial detector is used, the Pixirad I. The Pixirad is a 2-D imaging X-ray detector. Due to an array arrangement of many semiconductor detectors, an image of the radioactive source dependent on the energy can be taken. By putting a radiator between the beam and the detector, the emitted radiation can be detected with the Pixirad. The intention of this bachelor thesis is to automatise the measurement of the Pixirad I and its characteristics. Hence, the spectra of two different radioactive sources are measured with different detector settings.

The required theoretical knowledge is given in chapter 1.
In chapter 2, the experimental settings are described including the hardware

and the software of the detector. The modifications of this software are described afterwards.
Chapter 3 contains the measured spectra of the sources ^{55}Fe and ^{241}Am and their analyses. Regarding the iron source, several measurement conditions are altered in order to characterise the detector: the temperature, the measurement time and the collimator.
A conclusion of the results and an outlook about the usability of the Pixirad I as a reference detector of TR-photons are given in chapter 3.

1 Theoretical Background

The PixiRad detector uses an array of semiconductor sensors to detect X-ray photons. Hence, this chapter explains the theoretical background of the interactions of photons in the detector and the function of semiconductor sensors. In addition, the general different radioactive decays and the decay schemata of the used radioactive sources are specified.

1.1 Interactions of Photons with Matter

Interactions of photons with matter can be categorised in three effects dependent on the photon energy $\hbar\omega$. The intensity of a photon after a distance x in matter is weakened exponentially with x: $I(x) = I_0 e^{-x\mu}$. μ is the attenuation coefficient of the material and I_0 the initial intensity of the photon.
The three most important mechanisms of interaction are

1. the photoelectric effect,
2. the Compton scattering
3. and the pair production. [2]

1.1.1 Photoelectric Effect

A photon can transfer all its energy to an electron in the atomic shell causing it to move out of the shell. In this process the whole photon is absorbed:

$$\gamma + A \rightarrow A^+ + e^-. \tag{1.1}$$

The energy of the emitted electron is $E_e = \hbar\omega - E_B$, where E_B is the binding energy of the electron.
The cross section of the photoelectric effect is proportional to $\sigma_{ph} \sim Z^5$ with Z being the proton number of the material. The photoelectric effect mainly arises at photon energies up to 0.5 MeV. [2]

1.1.2 Compton Scattering

In the Compton scattering, a photon scatters on an electron from the outer atomic shell. The photon loses some of its energy while the electron is solved from the shell:

$$\gamma + A \rightarrow A^+ + e^- + \gamma'. \tag{1.2}$$

With the energy conversation $\hbar\omega = \hbar\omega' + E_e$ and the momentum conversation $\overrightarrow{p}_\gamma = \overrightarrow{p}_e + \overrightarrow{p}_{\gamma'}$ the energy of the electron after the scattering is [2]

$$E_e = \hbar\omega \frac{\frac{\hbar\omega}{m_e c^2}(1 - \cos\vartheta)}{1 + \frac{\hbar\omega}{m_e c^2}(1 - \cos\vartheta)}, \tag{1.3}$$

where m_e is the electron mass and c is the speed of light. The cross section is proportional to the proton number $\sigma_c \sim Z$. The Compton scattering is the dominating interaction process at photon energies between 0.5 MeV and 5.0 MeV.
The energy transferred to the electron is described by a continuous function of the scattering angle ϑ. The function shows a significant edge at $\vartheta = 180\,^\circ$. At this angle the photon loses the most energy to the electron. This socalled Compton edge obeys from equation (1.3) as

$$E_e(180\,^\circ) = \frac{\hbar\omega}{1 + \frac{m_e c^2}{2\hbar\omega}}. \tag{1.4}$$

In case of the photoelectric effect and the Compton scattering, unpopulated states remain in the electron shell. They are filled by other more weakly bound electrons causing two different types of radiation. Characteristical X-rays with the energy of the difference of the binding energies of the two electrons can be emitted. These photons are called K_α, L_β etc. The letter K and L stand for the inner shell where the electron is moved. The index describes the difference between the main quantum number n and the initial shell of the electron. In this case, α is equal to $\Delta n = 1$ and β to $\Delta n = 2$.
Another option is the transferring of the released energy to another slightly bound electron (Auger electron) in the shell, which is emitted with the certain energy $E_{Auger} = E_{hole} - E_{B1} - E_{B2}$, where E_{hole} is the binding energy of the unpopulated state and $E_{B1/2}$ are the binding energies of the two electrons. [2]

1.1.3 Pair Production

If the photon's energy is greater than twice the rest energy of an electron ($\hbar\omega \geq 2m_e c^2 = 1.022\,\text{MeV}$), the photon can convert into a particle-antiparticle pair. Due to the momentum conservation, a third particle

is needed within this process, usually the nucleus, taking some of the momentum.
The cross section of the pair production is proportional to $\sigma_p \sim Z^2$. [2]

1.2 Radioactive Decays

One cannot predict, at which time one single radioactive nucleus decays, but one can describe the statistic characteristics of many nuclei. The number of nuclei after a decent time is given by

$$N(t) = N_0 \cdot e^{-t\lambda} = N_0 \cdot e^{-t/\tau}, \tag{1.5}$$

where N_0 is the initial number of nuclei and λ the decay probability. The half life $t_{1/2}$ is the time after which half of the nuclei decayed:

$$t_{1/2} = \frac{1}{\lambda} \ln 2 = \tau \ln 2. \tag{1.6}$$

There are different ways a radioactive isotope can decay. Some of them are explained below, as they are especially chosen for this thesis.

1.2.1 α Decay

A heavy nucleus can decay by emitting a helium nucleus, an α particle:

$${}^{A}_{Z}\mathrm{X}_N \rightarrow {}^{A-4}_{Z-2}\mathrm{X}_{N-2} + {}^{4}_{2}\mathrm{He}_2. \tag{1.7}$$

This decay has a discrete energy of about 5.5 MeV, which is not high enough to conquer the Coulomb barrier of the nucleus. Thus, in classical mechanics this decay is actually forbidden, but due to quantum mechanics, it is possible for the α particle to tunnel through this barrier. [2]

1.2.2 β Decay

Another possible decay is the β decay where a neutron decays into a proton or a proton into a neutron by emitting an electron or positron. Due to the conservation of the angular momentum, a third particle has to be emitted, the electron neutrino ν_e, postulated by W. Pauli in 1930 and verified by Cowan and Reines in 1956.
There are three different kinds of β decays [2]:

1. β^- decay

$$n \rightarrow p + e^- + \bar{\nu}_e$$
$$\text{energy :} \qquad Q(\beta^-) = B(Z+1, A) - B(Z, A) + \underbrace{(m_n - m_p - m_{e^-})c^2}_{+0.78\,\mathrm{MeV/c^2}} \tag{1.8}$$

2. β^+ decay

$$p \rightarrow n + e^+ + \nu_e$$
$$\text{energy :} \qquad Q(\beta^+) = B(Z-1, A) - B(Z, A) + \underbrace{(m_p - m_n - m_{e^+})c^2}_{-1.8\,\mathrm{MeV/c^2}} \tag{1.9}$$

3. electron capture (EC)

$$p + e^- \rightarrow n + \nu_e$$
$$\text{energy :} \qquad Q(EC) = B(Z-1, A) - B(Z, A) + \underbrace{(m_p + m_{e^-} - m_n)c^2}_{-0.78\,\mathrm{MeV/c^2}} \tag{1.10}$$

The Bethe-Weizsäcker energy balance of the three decays indicates that the β^- decay is the only decay that can happen without any additional energy. Furthermore, the electron capture is preferred compared to the β^+ decay. In the electron capture, an electron from the atomic shell is captured by a proton of the nucleus. The proton converts into a neutron under the emission of an electron neutrino. [2]

1.2.3 Electromagnetic Transitions

In consequence of the β and the α decays, the nucleus remains in an excited state. By returning into the ground state, the energy difference can be released in several ways. One way is the emission of some kind of particle. Among others γ quanta can be emitted. Furthermore, the excitation energy can be transmitted to an electron (conversion electron) in the shell. As a result the conversion electron is knocked out of the atom just like in the photoelectric effect. Because an unpopulated state remains in the electron shell after the emission of a conversion electron, other electrons of the shell occupy this state. The difference of the binding energies can be emitted in terms of characteristic X-rays or an Auger electron, as explained in chapter 1.1.2.
If the energy is higher than twice the rest mass of an electron (1.022 MeV), an electron positron pair can be created inside the nucleus and emitted out of it. [2]

1.3 Semiconductors

The outer electrons (valence electrons) of an atom in a crystal grid determine the electric properties of a material. These electrons are not bound to any atom in a metal, hence they can stream through the solid. In insulators the valence electrons are tightly linked to an individual atom and cannot move freely, preventing an electrical current. The semiconductor silicon has four outer electrons shared with the four nearest neighbour atoms. At low temperatures the electrons are not able to be shared with different atoms, but at higher temperatures the bounds between the nucleus and the electrons can be broken and the electrons can move in the crystal lattice.
Describing the energetic state of electrons requires the energy-band diagram (figure 1.1) where the possible energies captured by an electron are divided into two socalled energy bands. The valence electrons in a semiconductor can occupy a limited number of energy levels, the valence band. The higher energetic band, the conduction band, is empty and not filled with electrons. These energy bands are separated by an energy gap, so the electrons cannot move from the valence into the conduction band without energy. In a conductor this forbidden energy gap is missing due to the overlap of the energy bands. As a result, the electrons can move freely. In an insulator the energy gap is much larger than in a semiconductor. Due to this distance, the energy of an electron also has to be high to overcome the gap. The Fermi level describes the highest energy, which can be occupied by the electrons in the ground state of the system. [3]

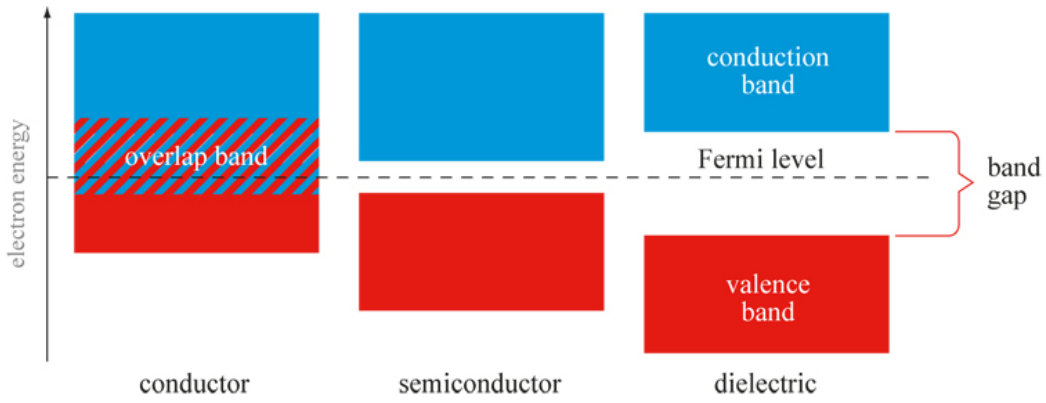

Figure 1.1: Presented is the energy-band diagram of different types of materials, on the left side a conductor with overlapping valence and conduction bands, a semiconductor in the middle with a small energy band gap and on the right side an insulator with a bigger band gap. [4]

1.3.1 Doping

By impurifying a semiconductor with atoms of another element, its conductivity can be controlled. Silicon for example, has four valence electrons bound to each nucleus. By adding a pentavalent element including five valence electrons (usually phosphor), one additional electron is needed to bound with every silicon electron. The remaining electron is just slightly bound to its nucleus and can easily be separated from it. This type of doped semiconductor is called an n-type semiconductor and the impurifying element is called a donor.
However, substituting some of the silicon atoms with atoms of a trivalent element, like boron, results in one absent electron to bound to a silicon valence electron. Thus, a socalled electron hole remains. This type of semiconductor is called a p-type semiconductor and the trivalent element is called an acceptor.
Because an additional less tightly bound electron exists for each impurifying atom in an n-semiconductor, it is much easier to lift the electrons into the conduction band. Accordingly, the Fermi energy is shifted up near to the conduction band (figure 1.2). In a p-semiconductor it works the other way around, as it is easy to lift the electrons from the valence band into the energy level of the electron holes, leaving holes in the valence band and shifting the Fermi level down. [3]

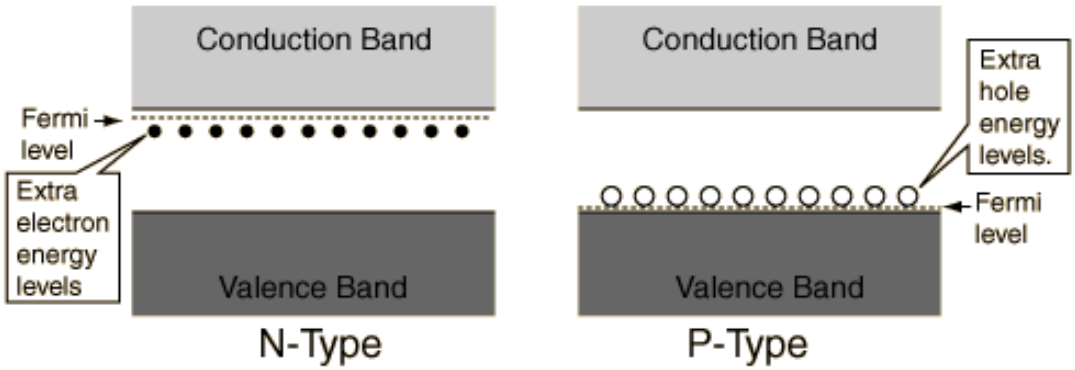

Figure 1.2: An energy-band diagram of an n-type (left) and a p-type (right) semiconductor is pictured. The Fermi level is risen to the conduction band in the n-semiconductor and lowered near to the valence band in the p-semiconductor. [5]

1.3.2 p-n Junction and Diode

By attaching a p-type to an n-type semiconductor an instantly current flow is arising. Both, the free electrons from the n-layer and the free movable electron holes from the p-layer diffuse into the opposite layer simultaneously. In addition, the electrons are recombining with the holes in the p-layer and the holes are recombining with the electrons in the n-layer. Due to this, charge carriers in the p- and n-regions near by the junction are missing. This region is called the depletion region. As a result of the depletion region an electric field is created countering the diffusion current. These two concurrent effects neutralise each other after some time, so no current flows after an equilibration time. A p-n junction is the basic component of a semiconductor diode.
Applying a voltage on a p-n junction, it can work in forward or reverse bias. In the forward bias mode, the p-layer is connected with the positive and the n-layer with the negative potential. The holes in the p-layer and the electrons in the n-layer are flowing towards the depletion region by restricting this zone. If the applied voltage is high enough, the depletion region is thin enough to enable the charge carriers to cross the junction, letting an electric current flow.
In the revers bias mode, the p-layer is connected with the negative and the n-layer with the positive terminal. In this case, the charge carriers are pushed away from the depletion zone and expand it. Thus, the energy gap to cross the p-n junction is higher and no current flows.
Nevertheless, even in revers junction a current, called leakage current, can flow due to the quantum mechanical probability allowing electrons or holes to tunnel through the space charge region. The tunnel probability depends on the thermal and kinetic energy of a charge carrier and therefore, increases with higher temperature and lower thickness of the depletion region.

1.3.3 Schottky Diode

Schottky diodes do not have a p-n junction like a normal diode but a metal-semiconductor junction. n-type semiconductors are usually used here. If an n-semiconductor is attached to a metal, electrons from the n-layer diffuse into the metal and leave holes in the semiconductor creating a depletion zone. By applying a voltage in forward bias (negative terminal on n-layer), electrons from the semiconductor are pushed into the barrier layer and can flow into the metal.
The sensors used in the Pixirad detector are cadmium telluride Schottky diodes, which are known for very low leakage currents.

1.3.4 Semiconductor Detectors

A semiconductor detector works like a normal diode with a thicker barrier layer. This diode operates in reverse direction preventing a current flow. If a particle crosses this barrier layer, it causes the appearance of electron-hole pairs which immediately are divided due to the applied voltage. Every electron-hole pair leads to a small current pulse which can be detected.
Because many pairs are created by one single particle, the energy resolution of the detectors is addicted to its energy. The higher it is, the more pairs are produced and the energy resolution will fall with $\sqrt{N}$, where N is the number of created electron-hole pairs. To act on the assumption, that a Poisson distribution is the basis of the statistics of the events n of a nuclear decay, the measurement error is $\sqrt{n}$. [2]

2 Experimental Setup

This chapter explains the experimental setup including the applied measurements. Hence, the hardware and the software of the detector and the used nuclear sources are specified.

2.1 Hardware of the Pixirad I Detector

The Pixirad I detector of the Company PIXIRAD Imaging Counters s.r.l. is used for all following measurements. The Pixirad is based on many CdTe (cadmium telluride) Schottky type diodes as detectors, arranged in a 512×476 array with an energy range from 0.5 keV to 89.0 keV. Following this array arrangement, pictures from the measured radioactive source can be taken with one detector as one pixel. One pixel can detect up to 10^6 counts per second. [6]
The detector operates with deionised water mixed with anitfreeze for cooling. Dry carbondioxid is used for drying the detector. The complete setup of the experiment is pictured in figure 2.1 illustrating the cooler on the left, the power electronics of the detector in the middle and the actual detector on the right side.

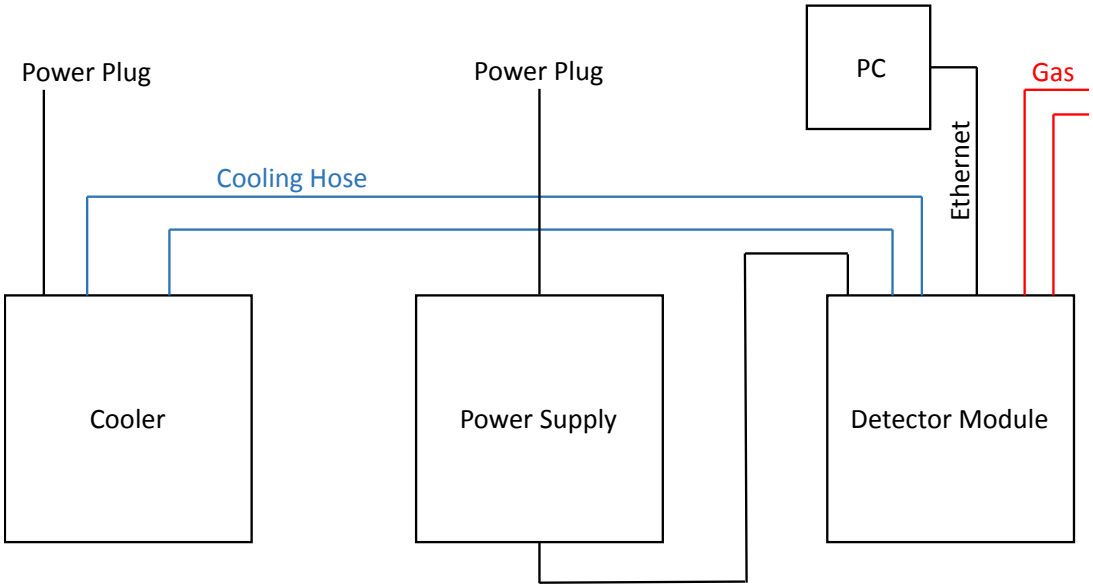

Figure 2.1: The theoretical setup of the experiment is presented: the cooler is pictured on the left, the power interface in the middle and the Pixirad detector module on the right with the cooling hoses, the gas supplies, the Ethernet cable and the power cable connected.

2.2 Software of the Pixirad I Detector

The program version *Pixirad I Monitor 4.25* is the basis for controlling the detector. The most relevant parts of the graphical user interface and the program including the modifications which have been made, are explained below.

2.2.1 Graphical User Interface

The Pixirad detector can mainly run in two different modes which are relevant for the measurements. The first one is the manual mode where one has to make the adjustments for one single measuring. After this measuring is ended, one receives the integrated sum of elements counted by the detector and a .dat file. The .dat file can be analysed with the Pixirad analysing software obtaining a picture of the radioactive source. The manual mode can be activated in the '*Detector settings*' window in the LabView frontpanel as pictured in figure 2.2. The most interesting settings for the measurements are the '*Shutter width [ms]*', the '*Modality*' and the '*Threshold*' blocks. The shutter width sets the measurement time

in milliseconds, the modality the detection mode and the threshold the energy in keV, above which the incoming particles are counted. Regarding the detection mode, the Pixirad has two different registers, a low and a high register, which thresholds can be set independent from each other. One can choose between a '*One color*', a '*Two color*' and a '*Four color*' option. In the '*One color*' mode only the particles of the chosen low or high register are counted. If one chooses the '*Two color*' option, both registers are read out simultaneously. The '*Four Color*' modality is redundant for the measurements. The '*High voltage settings*' are usually set to automatic, so no changes have to be made here. A measurement can be started by pushing the '*START*' button in the left down corner of the window given that an automatic calibration has been done before. This is conducted automatically by the detector after the '*AUTOCAL*' button has been acitvated.

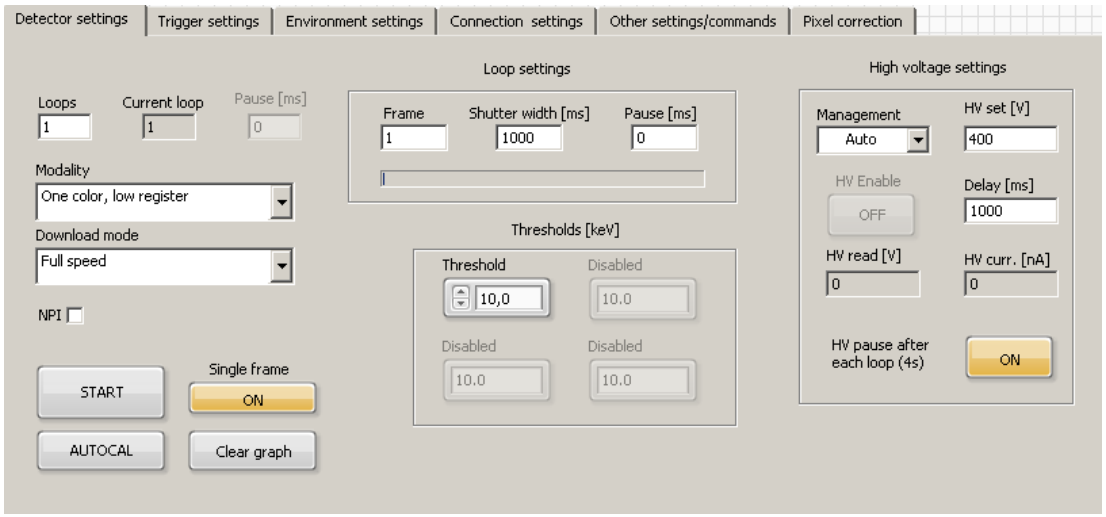

Figure 2.2: Presented is the '*Detector settings*' window, where one can make the adjustments for a measurement. The most relevant parts are: the '*Modality*' field setting the detection mode, the '*Shutter width [s]*' field setting the measurement time and the '*Threshold*' field setting the energy in keV, above which every coincidence is measured. Pushing the '*START*' button starts a measurement and pushing the '*AUTOCAL*' button causes an automatic calibration.

The second mode is the energy scan where one has to adjust a minimum ('*Min [keV]*') threshold, a maximum ('*Max [keV]*') threshold and an energy step width ('*Step [keV]*'). In this energy scan mode the detector takes many measurements with all thresholds between the minimum and maximum threshold with the given energy step width. In the end, one obtains an info text file and a .dat file of all thresholds combined. The info file contains information about the detector settings at every energy step, but misses information about the counts or the temperature. The energy scan can be selected in the '*Other settings/commands*' window (figure 2.3). The detection mode of the energy scan is automatically set to '*One Color, low register*' while the measurement time per energy step is taken from time shutter width of the '*Detector settings*' window.

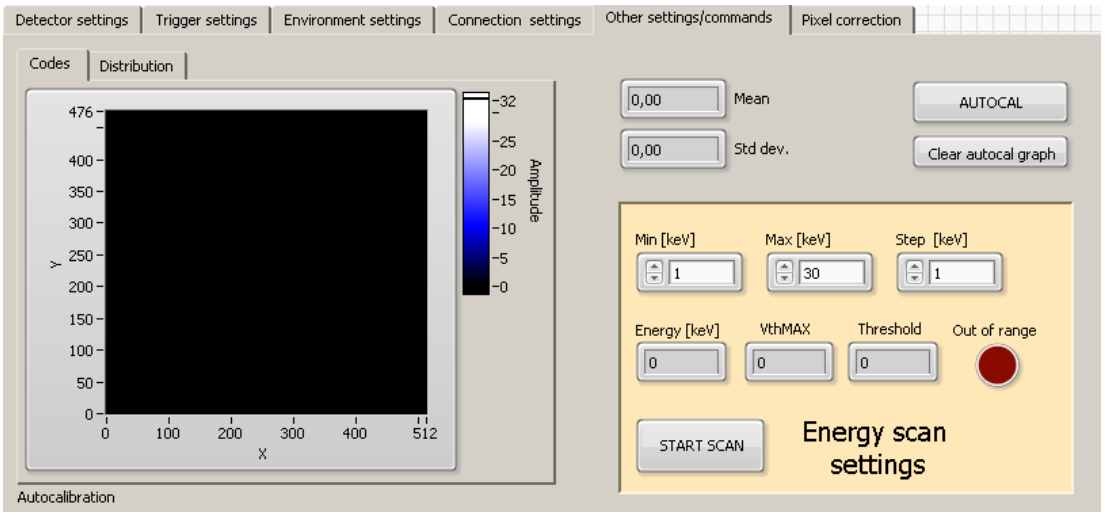

Figure 2.3: Presented is the '*Other settings/commands*' window, where one can make the adjustements for an energy scan. The minimum energy, the maximum energy and the energy step width can be set via the '*Min [keV]*', '*Max[keV]*' and '*Step [keV]*' fields. The current energy step is displayed in the box below. The energy scan is started with the '*START SCAN*' button.

Furthermore, the internal cooling of the detector can be set in the '*Environment settings*' window (figure 2.4). The Pixirad contains a peltier element regulated by the software. One can also enable or disable the peltier cooling and see different temperatures of the detector. The '*Detector temp. [°C]*' block indicates the actual detector temperature.

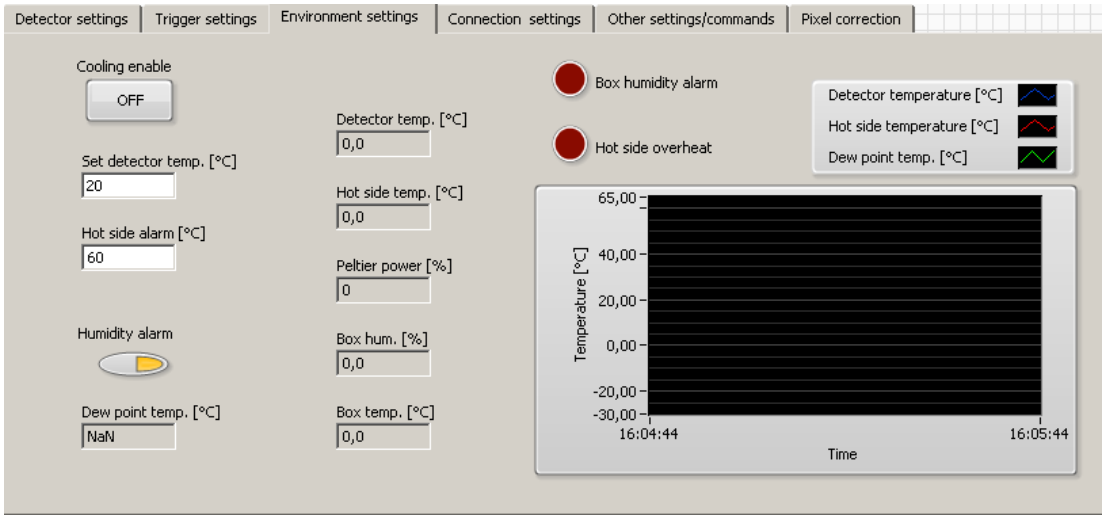

Figure 2.4: Presented is the '*Environment settings*' window, where one can enable the cooling via the '*Cooling enable*' button and set the peltier temperature via the '*Set detector temp. [°C]*' field. The actual detector temperatures can be read out.

Next to these windows there is another block in figure 2.5, where one can manage the saving settings of a measurement. When the '*REC*' button is activated, the measurement will be saved in the path that is typed in the '*File path*' field. Furthermore, one can choose via the '*DATA*' button, whether one wants to save the data as a picture file or a flatfield file. A flatfield file can be used to calibrate the measurement in the analysis software. This software can also be started in this window by the '*Run analysis software*' button.

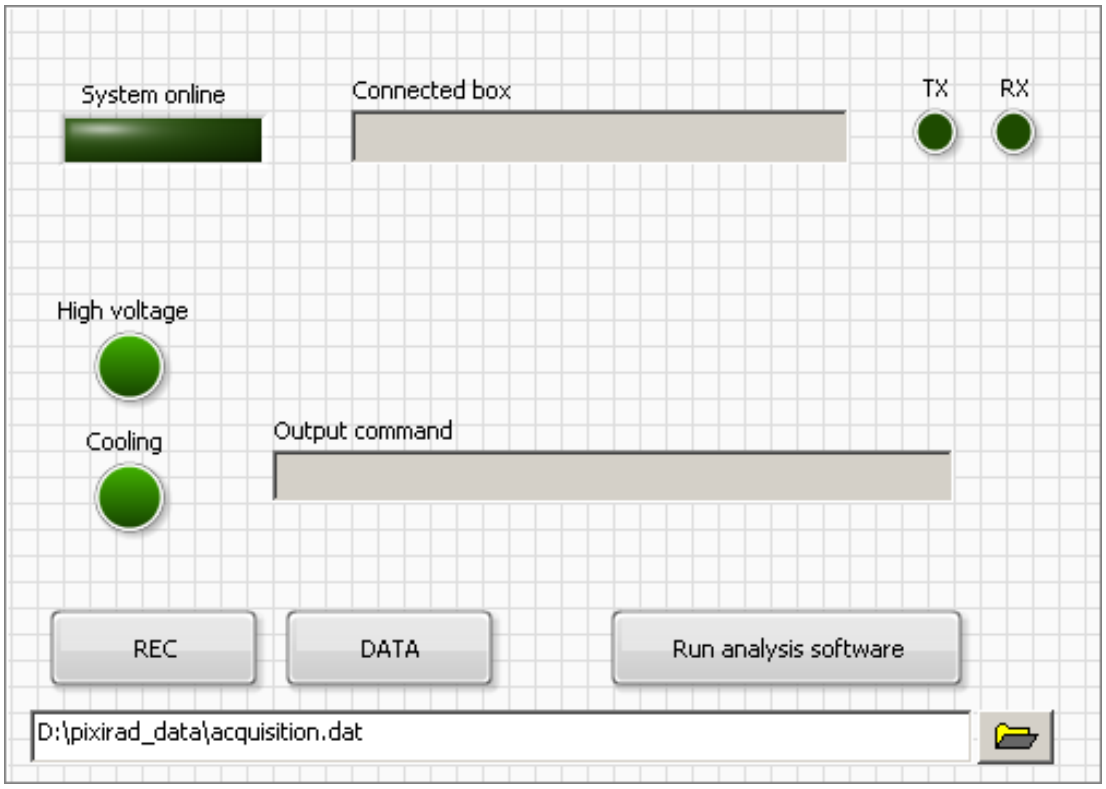

Figure 2.5: The saving options and status block on the frontpanel present the status of the system: the system is online, the high voltage is applied or the cooling is enabled. These information are indicated via the correspondent green lamps. One can adjust via the '*REC*' button if the measurement should be saved. The memory address is entered in the text field below. The analysis software can be started via the '*Run analysis software*' button.

2.2.2 LabView Program

The aim of modifying the LabView program is to enable an automatic measurement dumping the data of a whole spectrum of the measured radioactive source. The energy scan mode does this partly, but one does not obtain any information about the counted elements or any other data of each individual energy step. For this, the energy scan option has been modified, so the sum of the counted elements for each threshold step is written down into a file with the proper threshold. But these integrated counts do not contain any information about the spectrum of the source. Hence, the difference between the sum of elements from two following energies is calculated obtaining the differential spectrum $\mathrm{d}N/\mathrm{d}E$. This differential spectrum is also written down into another file.
At the end of a measurement one receives two different files: one with the

sum of elements to each energy step, the '*count file*', and another one with the calculated spectrum, the '*spectrum file*', including the measurement error $\sqrt{n}$ in case of the count file and the Gaussian error propagation

$$\Delta\left(\frac{\mathrm{d}N}{\mathrm{d}E}\right) = \sqrt{n_1^2 + n_2^2} \tag{2.1}$$

in case of the spectrum file. n_1 and n_2 are the integrated counts of two following thresholds. As a consequence the differential spectrum can be written as $n_2 - n_1$.
In addition, these two data sets are plotted on the frontpanel of the program at the end of every measurement. Besides, the .dat file of every threshold step is saved. The info file is extended by the sum of elements and the detector temperature of every threshold step.
The most important parts of the original energy scan program block and the modifications are explained in the following chapter.

Original Program

Figure 2.6 shows the original LabView program block of the energy scan function activated after pushing the scan button on the frontpanel. There are diverse encircled parts whose functions are useful to know for reprogramming. At first the status of the '*REC*' button is requested in circle (1). If the '*REC*' button is true, a file with the typed file path is created. After the successful creation of this file, the status '*TRUE*' is handed over to the next '*if statement*' where the main parts, calculating the threshold and generating the info file, are conducted.

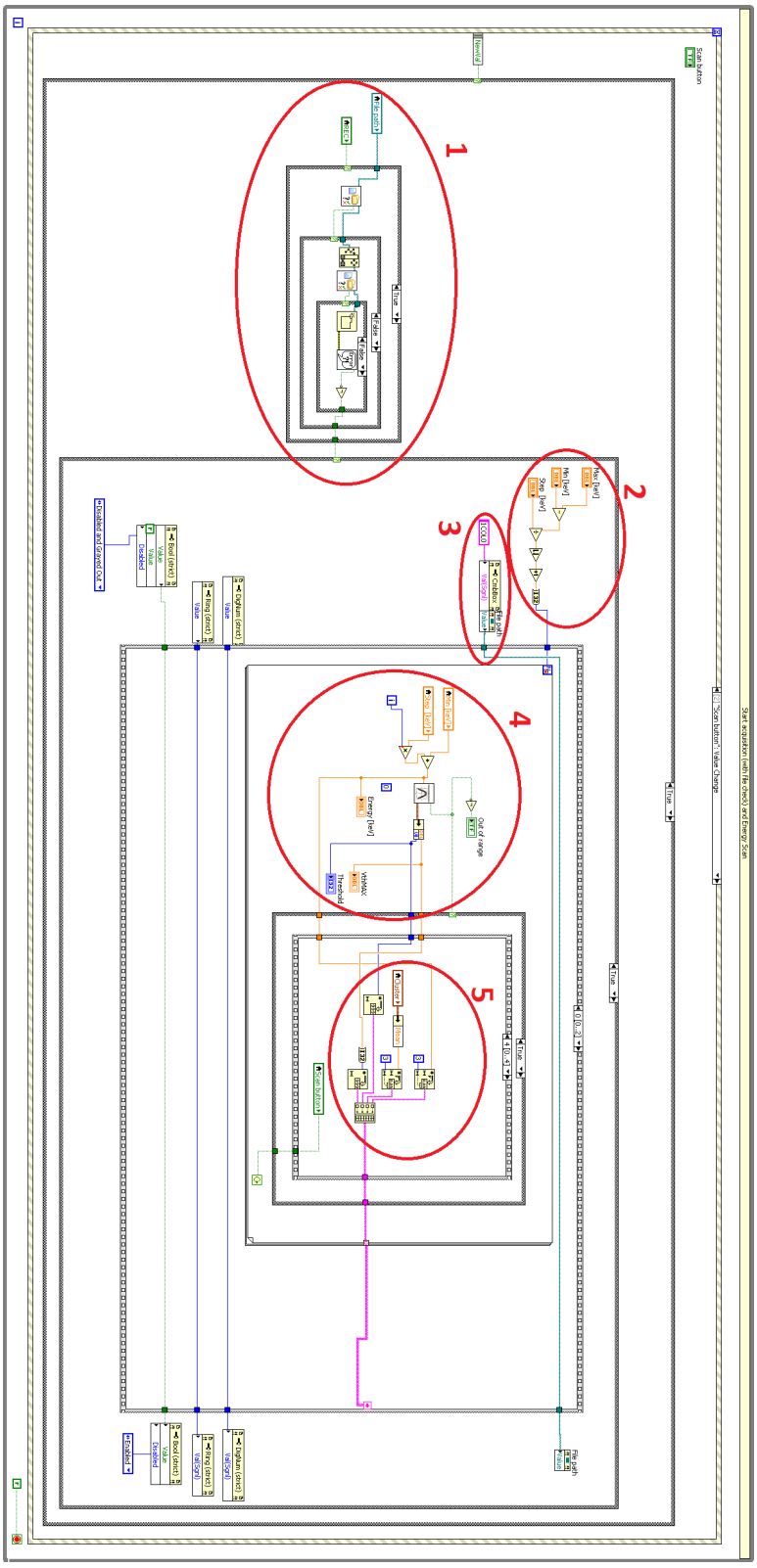

Figure 2.6: Presented is a brief overview of the original program with the most important parts: (1) The '*REC*' button request and the creation of the saved file. (2) The loop condition for the main computing loop. (3) The setting of the modality. (4) The calculation of the current threshold dependent on the current energy step. (5) The building of the information array, which will be written into the saved file.

The calculation of the threshold and the generation of the info file happen within a main case structure including 3 cases. The first two are important for the programming. In figure 2.8 one sees the first case, where the current threshold is calculated and the array with the data of the info file is built. For this, a loop is used passed as often as the numbers of energy steps from the minimum threshold to the maximum threshold. This value is calculated in circle (2) of figure 2.6. In (3) the modality is set to '*one color, low register*' while the file path is referred to the case structure.

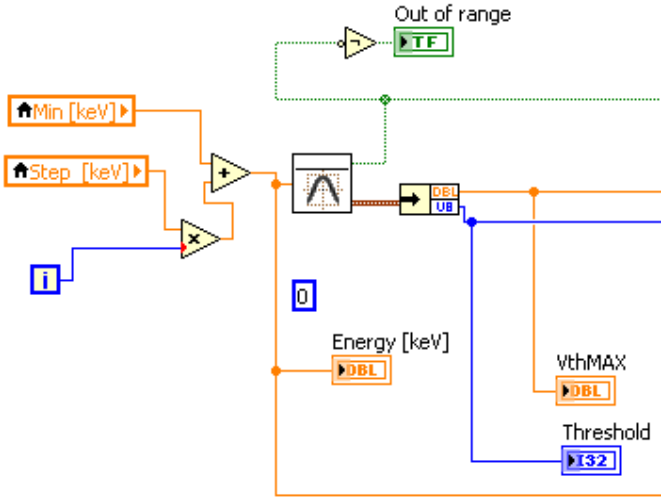

Figure 2.7: The part 4 of figure 2.6 presents the current threshold calculation with the calculation VI block in the middle.

The current threshold for each loop is computed with the '*Calculator VI*', the central block in figure 2.7. This is a preprogrammed LabView VI returning the detector settings depending on a delivered threshold value (Th) which was calculated before by the equation $Th_{curr} = Th_{min} + i \cdot stepwidth$, with the loop iteration i. The result is also displayed on the frontpanel in the '*Energy [keV]*' field. The calculator VI outputs an error message wether the threshold is out of the detector's range (1 - 89 keV) and a cluster with the computed threshold and the '*VthMAX*' value indicating the global threshold. These three data, the energy, the threshold and VthMAX are handed over to the case structure, where their string values are built into an array in addition to the '*mean of counts*'. This is done for every loop iteration, so that in the end one has an array with these information for every energy step. Afterwards, this array is given to the second case displayed in figure 2.9. The array is written into the info file which was created before. This file has the name ''*filepath*'_ *info.txt*' and has the following information beneath the array: the date, the minimum

and maximum threshold, the energy increment, the measurement time and the initial detector temperature. The file receives its information by the '*Build Text*' DAQ.
The scan button value is changed to false in the third case, while the energy scan block and therefore, the measurement is completed. One receives the info file with the explained information and one .dat file.

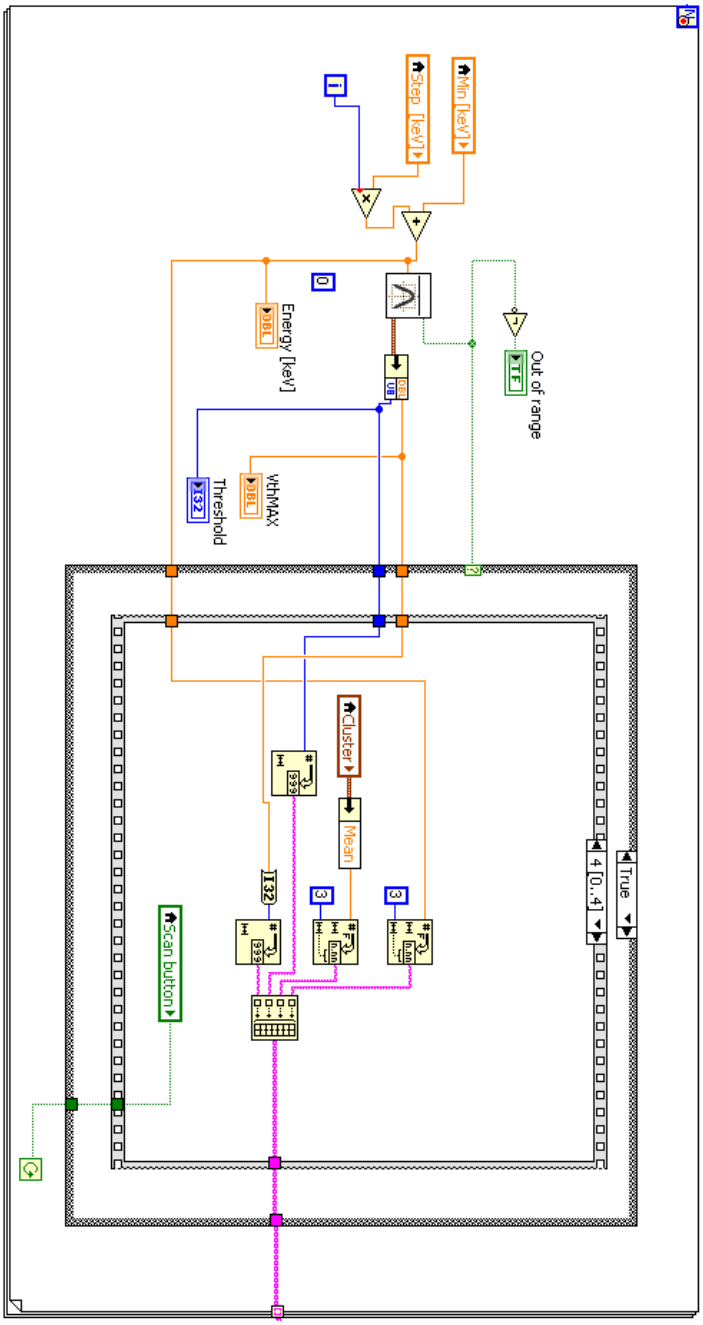

Figure 2.8: Presented is the first case (case 0) of the original program with the main computing loop. The current threshold is calculated on the left while the information array is built on the right.

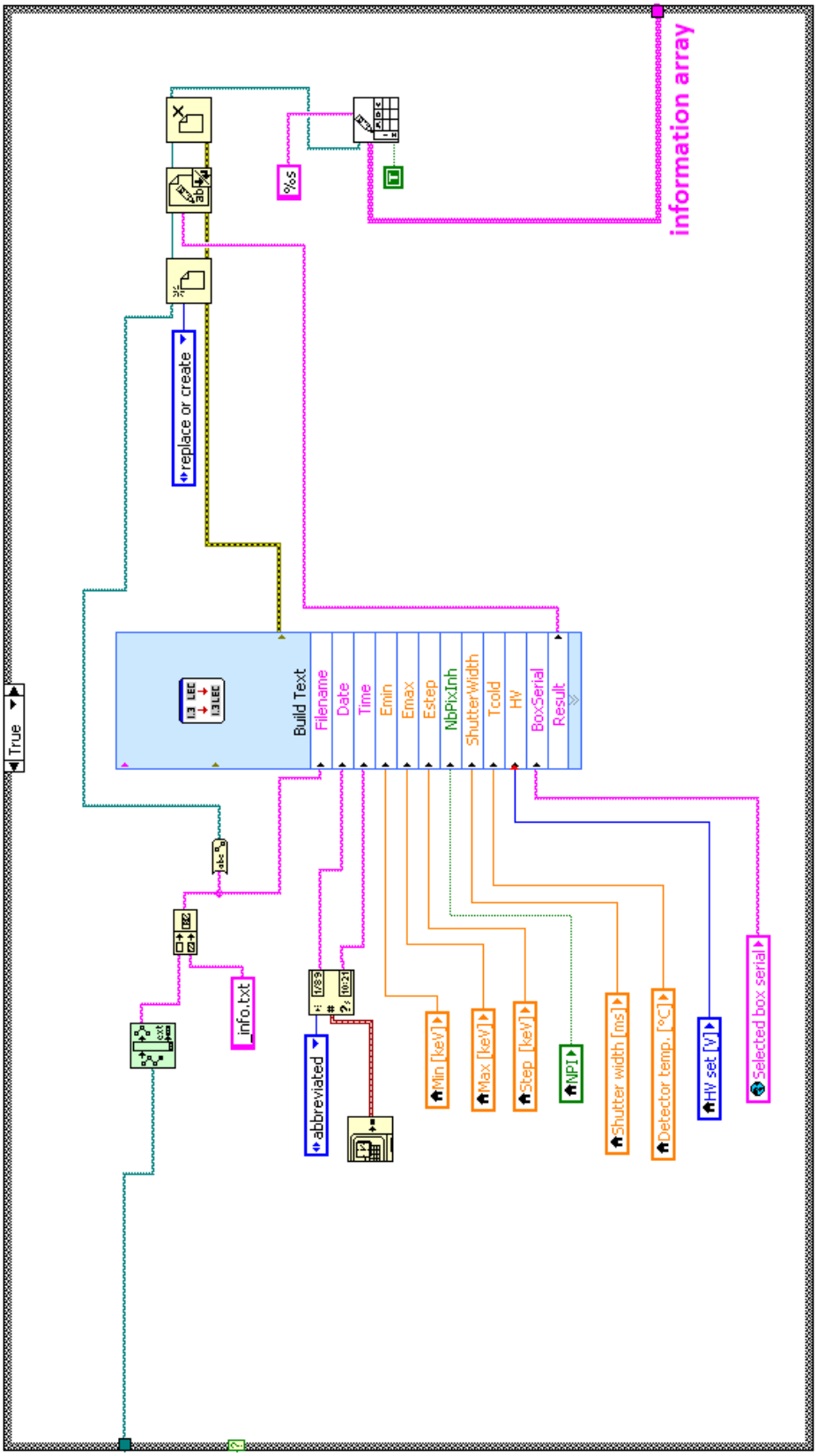

Figure 2.9: The main part of the second case (case 1) of the original program is illustrated. The text for the info file is built with all necessary parameters and the information array. Unbounded terms are edited.

Modified Program

The modified energy scan block is pictured in figure 2.11. The red encircled parts are exactly the same as in the original program, only the green encircled parts are new or reprogrammed.
Again, one can see the '*REC*' button and '*File path*' request in (1), the loop condition in (2), the '*File path*' and modality handover to the case structure in (3) and the threshold calculation in (4). Figure 2.10 shows the part (5) where changes in the array building has been made. Yet, the same array is built complemented by two new parameters, the sum of elements and the detector temperature. Besides, a cluster and an array with the numerical values of the energy and the '*sum of elements*' are created. The cluster is used for the representation of the counts as a function of the energy on the frontpanel. The array is needed for computing the spectrum. Moreover, a new fifth case was generated, wich can be seen in figure 2.12. In this case, an additional string array with information about the threshold, the '*sum of elements*' and its square root is built. This array is used for creating the counts file afterwards.

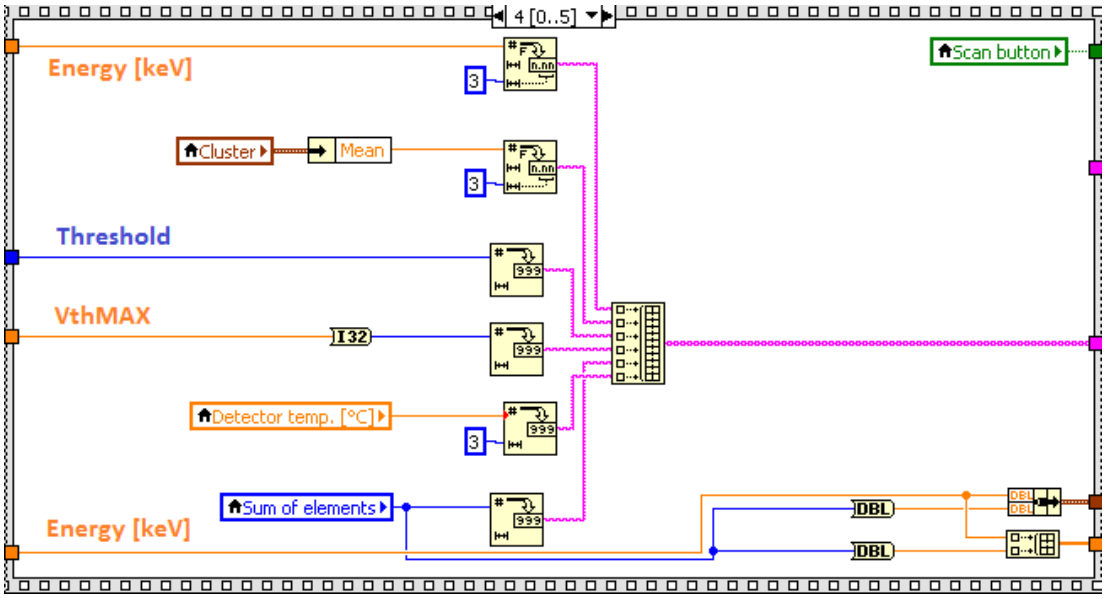

Figure 2.10: The fifth part of the modified program (figure 2.11) shows the building of the information array. The additional paramaters '*sum of elements*' and '*detector temperature*' are written into the array. Furthermore, another array and a cluster with the numerical value of the integrated counts are created. Unbounded terms are edited.

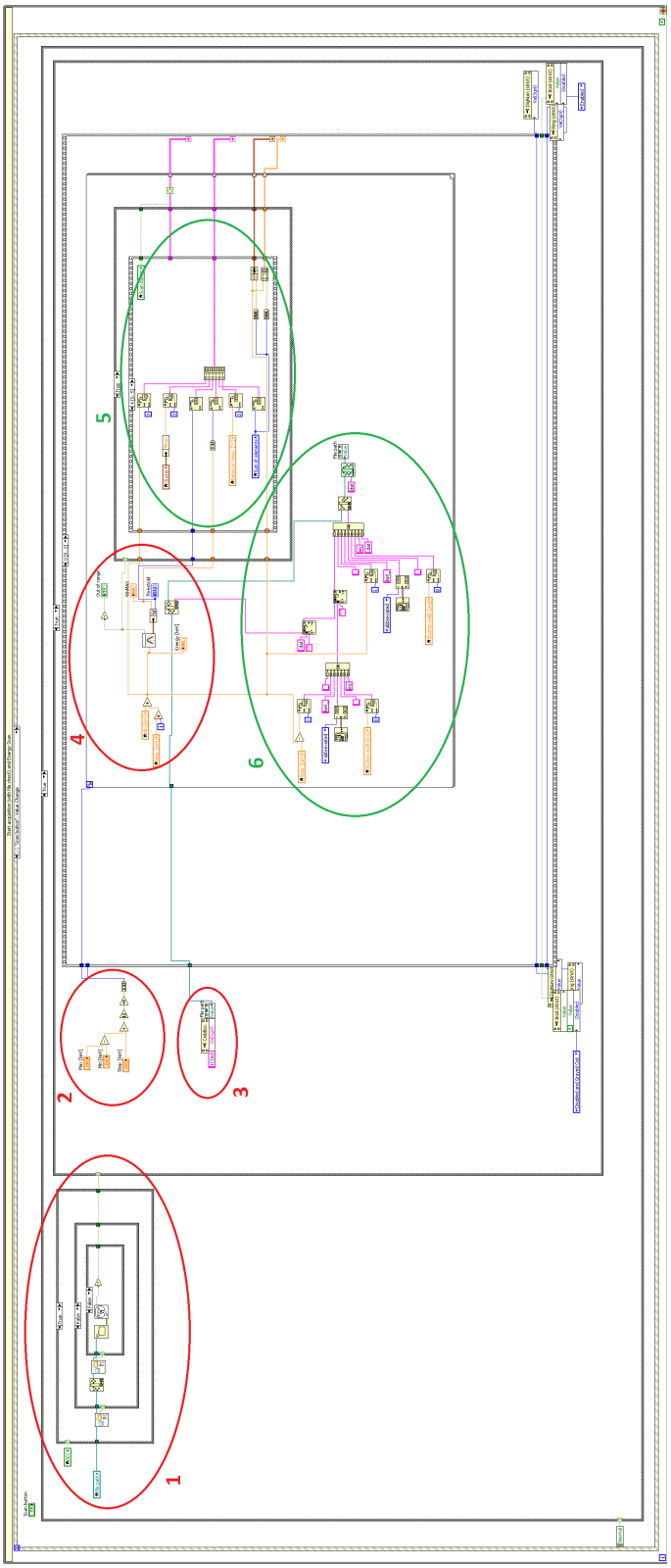

Figure 2.11: Presented is a brief overview of the modified program with the most important parts: (1) The '*REC*' button request and the creation of the saved file. (2) The loop condition for the main computing loop. (3) The setting of the modality. (4) The calculation of the current threshold dependent on the current energy step. (5) The building of the information array which will be written into the saved file.

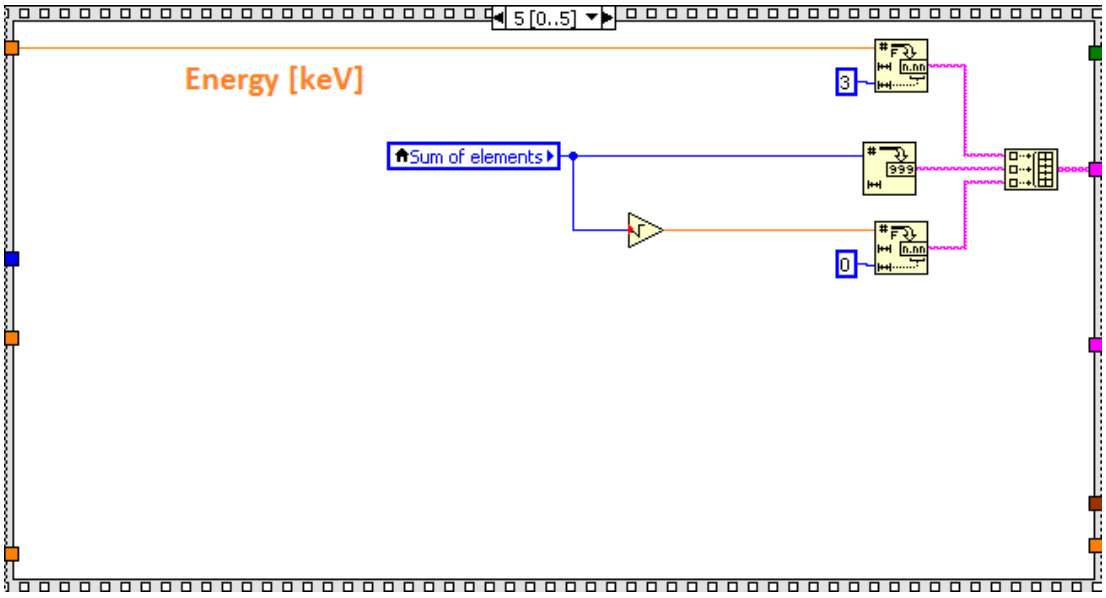

Figure 2.12: Pictured is an additional case in the main loop of the modified program. An array with information about the current energy step, the integrated counts and the measurement error $\sqrt{n}$ is built. Unbounded terms are edited.

The completely new programmed part (6) in figure 2.13 changes the value of the '*File path*' for every energy step. On the right side of the black line, several parameters such as the current energy, the date and the '*Shutter width [ms]*', are transformed into strings. These strings are concatenated with the string of the original file name, but without the path. The resulting string and the stripped path of the '*File path*' are used to build the new '*File path*' with a .dat ending. The final file is located at *'stripped path"file name'_ 'energy'keV_ 'date'_ 'Shutter width'ms.dat*.
As these information are added to the '*File path*' at every energy step, the file name would be far too long and confusing after a few loop iterations. Hence, the part of the file name with the strings of the settings has to be deleted before adding the new settings. This takes place on the left side of the black line. Thus, a string composed of the same components as the created file name, but with the previous energy, is created. This string and the .dat ending are replaced in the current '*File path*' by a blank line afterwards, so the resulting string is the original file name. This final string is also used for adding the new information to the new '*File path*'.
After these programmings are finished, the first main case (case 0) of the energy scan block is completed and four files are passed on to the second case (case 1): the string '*counts array*', the string '*info array*', the '*counts cluster*' and the numerical '*counts array*'.

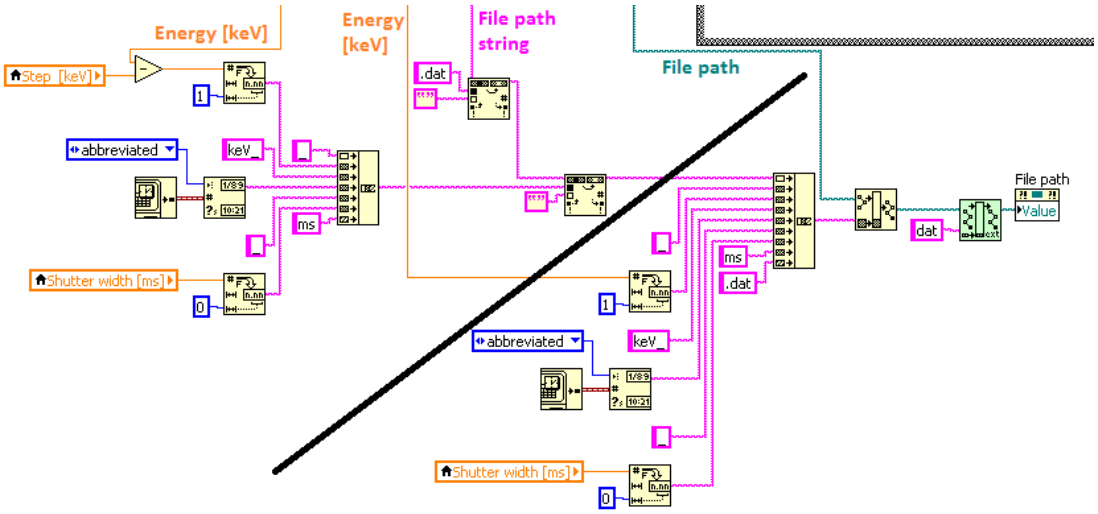

Figure 2.13: The sixth part of the modified program (figure 2.11) is shown. The '*File path*' is changed for every loop iteration: on the left of the black line the old file name is deleted. The new file name is created on the right side resulting in the filename *'stripped path"file name'_ 'energy'keV_ 'date'_ 'Shutter width'ms.dat*. Unbounded terms and the black line are edited.

The '*counts cluster*' is not further used and directly handed to the graph '*Counts after energy scan*'. The rest of case 1 (figure 2.14) is separated in two blocks, one on the left and the other on the right side. In the right block the counts, the spectrum and the info files are generated. The counts file, named *'file name'_ counts.txt'*, receives its information from the string '*counts array*'. It contains three columns, one for the energy, one for the '*sum of elements*' and a third one one for its measurement error $\sqrt{n}$. The info file has the same name as in the original program version (*'file name'_ info.txt*) and is built on the same way based on the string '*info array*'. It includes two additional columns, the '*sum of elements*' and the detector temperature at every energy step.

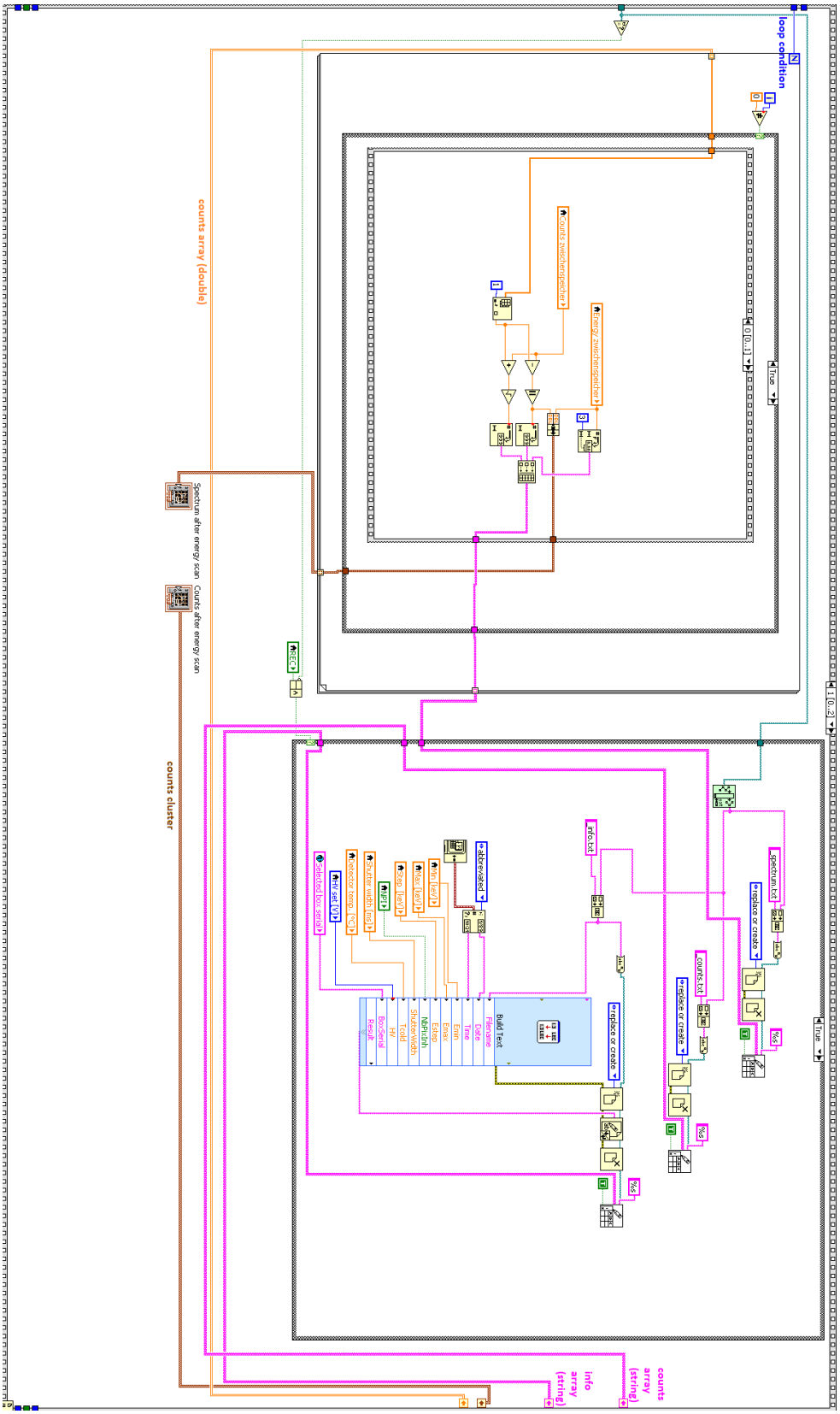

Figure 2.14: The second case (case 1) of the modified program is pictured. In the left block, the spectrum is calculated out of the numerical count array. In the right block, the text for the info file is created and the info, counts and spectrum files are generated. Unbounded terms are edited.

The last file, the spectrum file named *'file name'_ spectrum.txt*, obtains information from the left block of case 1 (figure 2.15), where the differential counts of the spectrum and their measuring errors are calculated. For this, a loop is used running the same amount of iterations, the number of energy steps, as the loop in case 0. At each iteration the '*sum of elements*' from the previous energy step is subtracted by the current value. The result is converted into a string and saved together with the previous energy value and the Gaussian error in an array. Furthermore, the energy and the differential counts are combined to a cluster directly connected with the graph '*Spectrum after energy scan*'. The current counts and the energy are written into a buffer afterwards, so they can be used as the previous value in the next iteration. This does not apply to the very first iteration $i = 0$, as no previous energy step exists. Hence the counts and the energy are only saved in the buffer and a blank space is added to the array. The resulting array is written into the spectrum file (*'file name'_ spectrum.txt*) in the left block of case 1. This file has three columns: the energy, the delta counts and their measurement error.

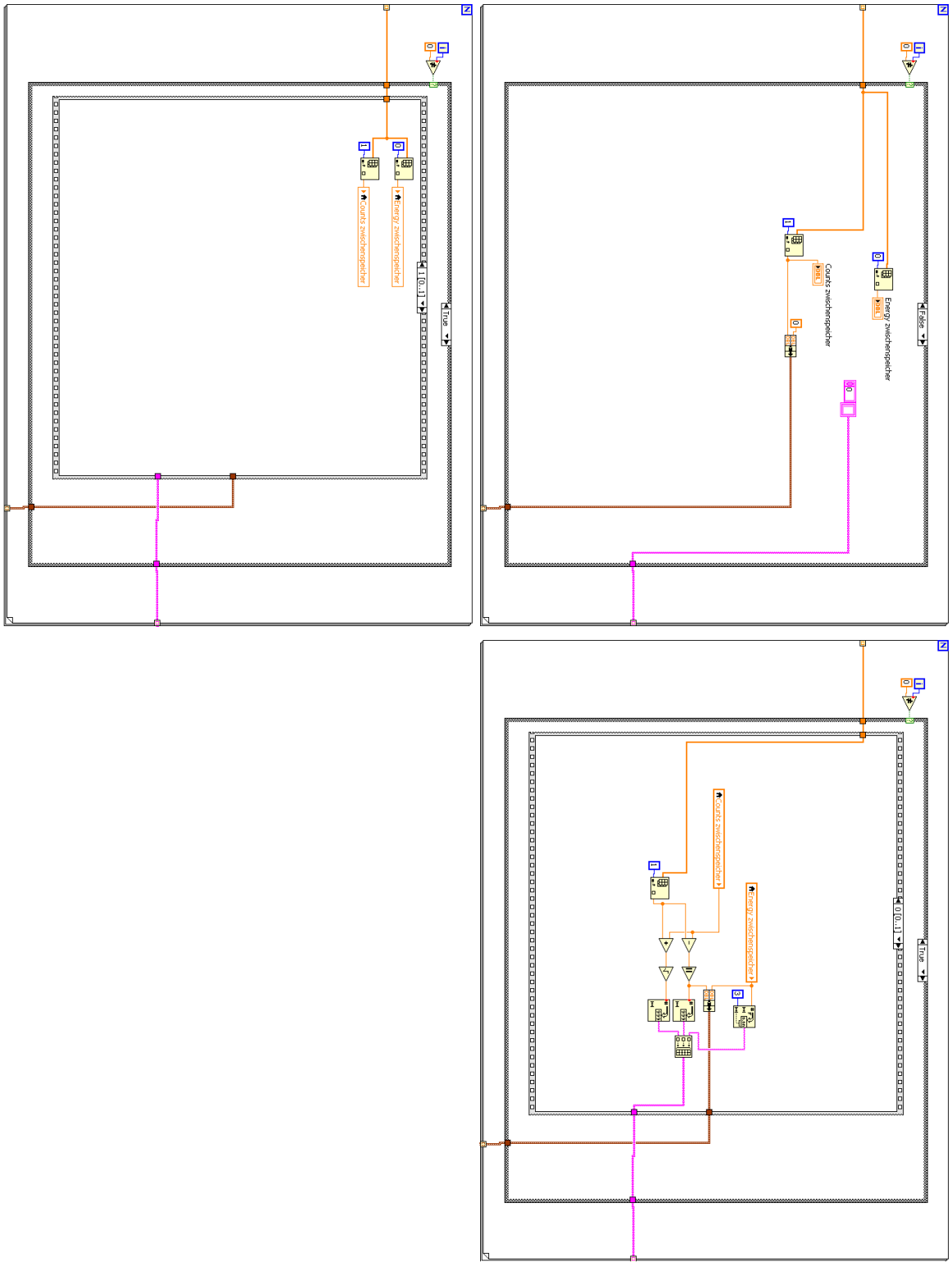

Figure 2.15: The creation of the spectrum array is pictured. In the upper left case the first loop iteration is shown, where the energy and the total counts are saved to a buffer. The first case for later iterations is presented in the upper right corner, creating an array including the energy from the buffer, the differential counts and their measurement error. The second case of later iterations is shown in the bottom, saving the current energy and the total counts to the buffer.

After applying all these modifications the program is completed and the following changes are made:

1. The information of the info file is extended to the '*sum of elements*' and the detector temperature.

2. The '*File path*' for every energy step is rewritten with the actual energy, date and shutter width, so one receives a separate .dat picture file for each energy step.

3. In addition to the info file, a counts and a spectrum file are produced. These files contain information about the counts or rather the differential counts as a function of the energy with the respective measuring error. These functions are also displayed in a graph on the frontpanel.

2.3 Nuclear Sources

The following two nuclear sources are applied to characterise the Pixirad I:

1. ^{55}Fe.

2. ^{241}Am.

These sources are used due to their characteristic peaks, which can be identified very well. The decay schemata and spectra are explained in the following chapter.

2.3.1 Decay and Spectrum of ^{55}Fe

^{55}Fe decays via electron capture into ^{55}Mn by emitting an Auger electron or X-ray γ quanta. The most important possibilities of emissions are a 5.19 keV Auger electron with a probability of 60 %, $K_{\alpha 1}$ X-rays of 5.90 keV with 16.22 %, $K_{\alpha 2}$ X-rays of 5.89 keV with 8.2 % and K_{β} X-rays of 6.49 keV with a probability of 2.85 %. The K_{α} lines are very close to each other, hence they are often detected as one 5.9 keV line with a probability of about 24.4 %. [7]
Figure 2.16 shows a recorded spectrum with the Pixirad detector from the official Pixirad website. As one can see, a peak at about 6 keV is expected, as the two dominant lines of the auger electrons and the K_{α} X-rays fall together due to of the energy resolution, which is larger than 0.7 keV.

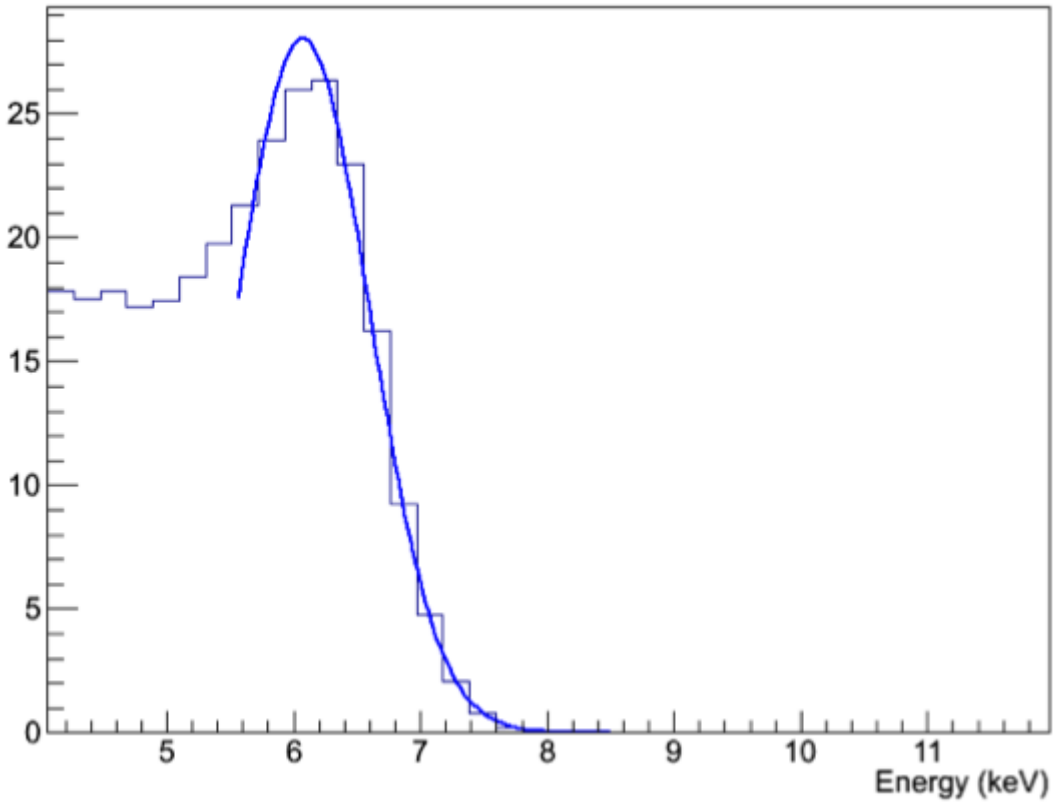

Figure 2.16: Presented is a spectrum of ^{55}Fe recorded by the PixiRad detector, as published on the official Pixirad website. [8]

2.3.2 Decay and Spectrum of ^{241}Am

^{241}Am decays with nearly 100 % via α decay into ^{237}Np. With a probability of 84.6 % an excited state of 59.54 keV is occupied directly emitting a 59.54 keV photon in most of the cases. This state also can transit into a 33.16 keV level by emitting a 26.34 keV gamma. With a probability of about 13 % the americium decay populates a ^{237}Np level of 102.98 keV mainly transitting into the 59.54 keV level by the emission of a 43.43 keV gamma. There can also be electron emissions due to the ^{237}Np transitions. The most probable ones are electrons with an energy of 37.11 kev to 41.93 keV, 10.77 keV to 15.59 keV and 20.99 keV to 25.81 keV. [9]
Due to the probability of the different decays and emissions, the mainly expected peaks in the spectrum are a a very high peak at 59.54 keV, followed in size by the 26.34 keV and the 33.16 keV line. Figure 2.17 shows the corresponding ^{241}Am spectrum recorded with the Pixirad detector based on the official Pixirad website.

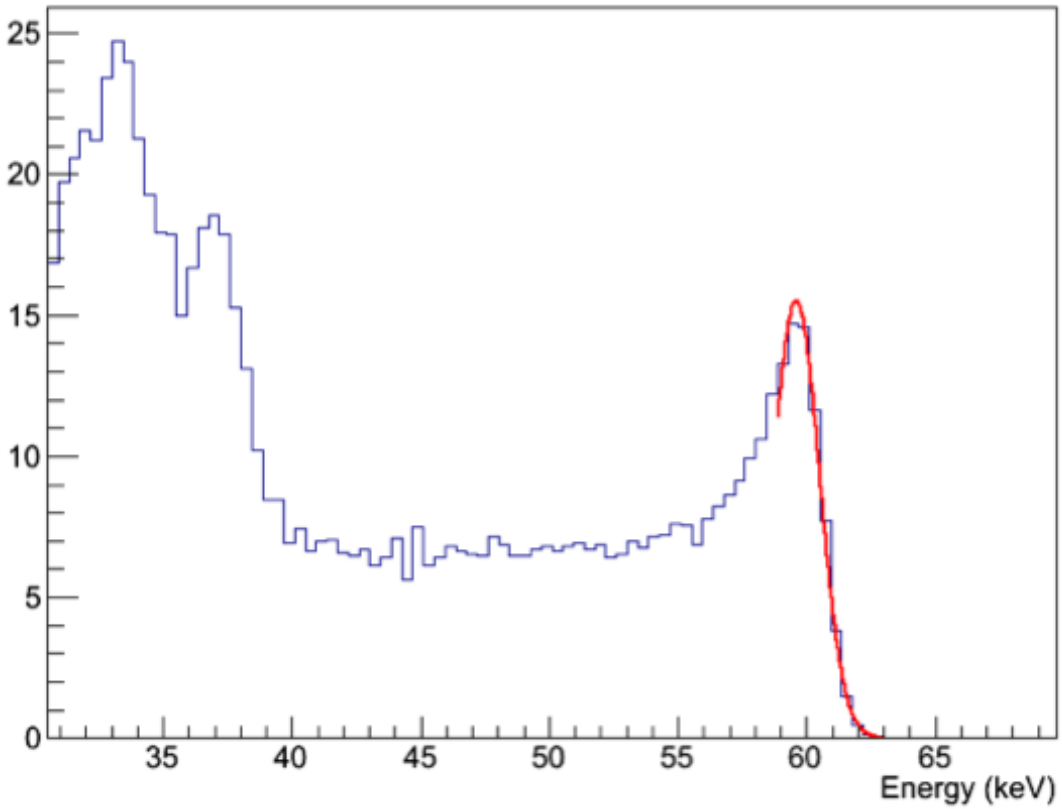

Figure 2.17: Presented is a spectrum of ^{241}Am recorded by the PixiRad detector, as published on the official Pixirad Website. [8]

3 Analysis of the Recorded Data

Several spectra of the nuclear sources illustrated in chapter 2.3 are recorded with the Pixirad I. These spectra are fit and analysed in order to characterise the energy resolution of the detector in dependence of different settings.

3.1 ^{55}Fe

The first measured nuclear source is ^{55}Fe. The detected spectra are described below including different settings of the ratio, the measurement time and the temperature.

3.1.1 Spectrum of ^{55}Fe

With the modified LabView program the spectrum of a ^{55}Fe source with an activity of 37 MBq is recorded. For this, an energy scan from 1 keV to 10 keV with an energy step width of 0.1 keV is conducted including different measurement settings of the time shutter width, the collimator and the temperature.
A detected spectrum of ^{55}Fe (figure 3.1) reveals different sections. At first, an exponential drop is visible due to the background radiation mainly appearing in the area around 1 keV. A nearly constant course dominates afterwards, followed by the expected peak at around 6 keV. After that, the counts drop down to a linear slope. All the counts in this last area must have their source in the background, as the highest energetic particles from the source are 6.5 keV photons.

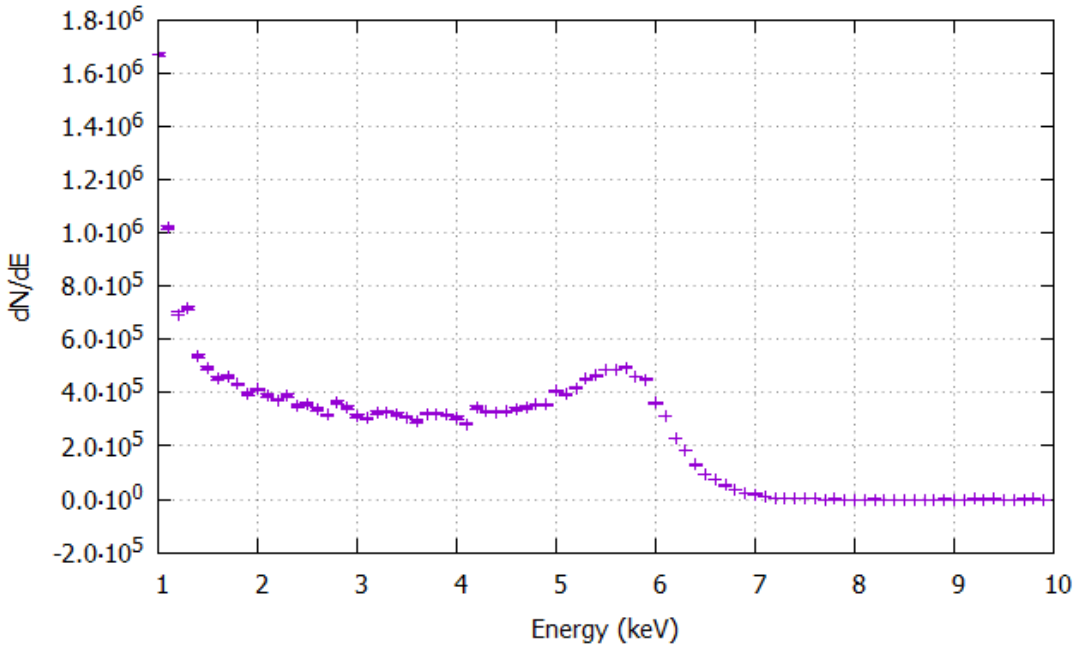

Figure 3.1: A differential spectrum of ^{55}Fe is pictured, recorded with no collimator, $T_{cooler} = -15\,°\mathrm{C}$, detector cooling off and 1 min time shutter width. The errorbars are plotted as well.

3.1.2 Fitting

As explained in chapter 2.3.1, ^{55}Fe has two dominant lines at 5.2 keV and 5.9 keV. Because of the detector's energy resolution these lines fall together and can not be detected separately. Hence, a function, including the addition of two Gaussian distribution, is used to fit the peak. This fit function has the form

$$f(x) = A_1 \exp\left(\frac{(x-\mu_1)^2}{2\sigma_1^2}\right) + A_2 \exp\left(\frac{(x-\mu_2)^2}{2\sigma_2^2}\right), \tag{3.1}$$

where μ is the mean and σ the standard deviation of the respective Gaussian distribution.
Because one knows the theoretical relative position of μ_1 and μ_2 and the relative values of the amplitudes A_1 and A_2 to each other, one can write μ_2 dependent on μ_1 and A_1 dependent on A_2. With $\mu_1 = 5.19\,\mathrm{keV}$ and $\mu_2 = 5.89\,\mathrm{keV}$ one receives

$$\mu_1 = \mu_2 - 0.7\,\mathrm{keV}. \tag{3.2}$$

With a probability of 60 % for the 5.19 keV line and 24.42 % for the 5.89 keV line, the depedence of the amplitudes between each other is given by

$$0.407 \cdot A_1 = A_2. \tag{3.3}$$

These relations lead to another fit function:

$$f(x) = A_1 \exp\left(\frac{(x-(\mu_2-0.7))^2}{2\sigma_1^2}\right) + 0.407 \cdot A_1 \exp\left(\frac{(x-\mu_2)^2}{2\sigma_2^2}\right). \tag{3.4}$$

As an alternative, two independent Gaussian distributions $f(x)$ and $g(x)$ are applied to fit the two lines at 5.2 keV and 5.9 keV.
In addition, an offset of the value of the constant area before the peak can be added to a fit function. Another option is subtracting this offset from the whole spectrum, which should have the same impact on the fit results as adding an offset.
To proof which function fits best to the spectra, a chisquare test is conducted. This test proofs the quality of a fit by calculating the sum of the difference between the measured data O and the expected value from the fit function E, divided by the expected value:

$$\chi^2 = \sum \frac{(O-E)^2}{E}. \tag{3.5}$$

The lower the outcome of the chisquare test is, the better the function fits to the measurement. The χ^2 test is dependent on the number of the degrees of freedom (NDF). Because the NDF can vary with different fits, the reduced χ^2 test may calculate a more objective result:

$$\chi^2_{red} = \chi^2/NDF. \tag{3.6}$$

Hence, all presented χ^2 results are results of the reduced χ^2_{red} test.
Finally, 9 functions can be fit to the spectrum. All resulting graphs are shown in the appendix, figures A.1 to A.6. All these fits are applied to the same spectrum. The results of the means and χ^2_{red} tests of these fits are listed in table 3.1.

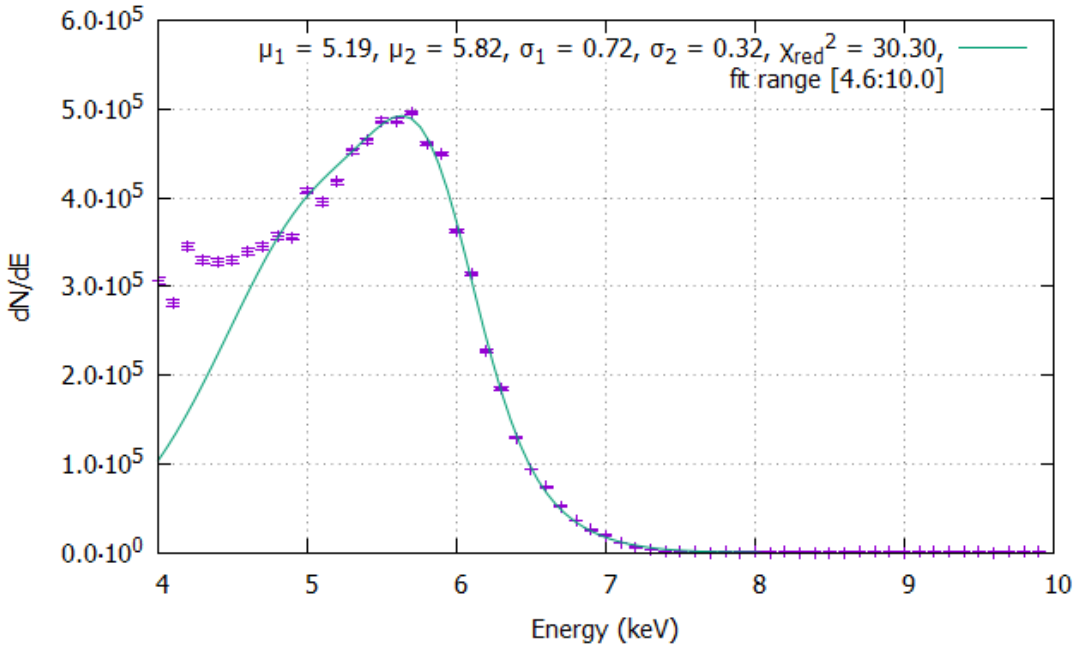

Figure 3.2: Presented is the differential spectrum of ^{55}Fe recorded with no collimator, $T_{cooler} = -15\,°C$, detector cooling off and 1 min time shutter width. The spectrum is fit by one function composed of the addition of two Gaussian distributions with independent parameters. The errorbars are plotted as well.

Table 3.1: The means and chisquare test results of the different fit functions.

fit	μ_1 (keV)	μ_2 (keV)	$\chi^2_{red,1}$	$\chi^2_{red,2}$
all independent (fig. A.1)	5.19 ± 0.05	5.82 ± 0.02	30.30	
all independent, offset (fig. A.2)	5.24 ± 0.72	5.69 ± 0.03	38.23	
all independent, gauged (fig. A.3)	5.24 ± 0.72	5.69 ± 0.03	38.23	
mean and amplitude dependent (fig. A.4)		5.85 ± 0.02	55.99	
mean and amplitude dependent, offset (fig. A.5)		6.26 ± 0.05	195.91	
mean and amplitude dependent, gauged (fig. A.6)		6.26 ± 0.05	195.90	
two Gaussian (fig. A.7)	5.18 ± 0.22	5.67 ± 0.05	45.96	61.06
two Gaussian, offset (fig. A.8)	5.18 ± 0.23	5.70 ± 0.04	51.86	126.05
two Gaussian, gauged (fig. A.9)	5.18 ± 0.23	5.70 ± 0.04	51.86	126.05

The best results, especially regarding the χ^2_{red} test, are achieved with the fit (3.1) pictured in figure 3.2. Furthermore, this function provides the most appropriate values for the means of the Gaussian distributions with $\mu_1 = (5.19 \pm 0.05)\,\text{keV}$ and $\mu_2 = (5.82 \pm 0.02)\,\text{keV}$. Although, μ_2 does not fit to the theoretical expected ^{55}Fe line at 5.89 keV, the deviation is small with 1.2 %. Hence, this fit can be used to analyse the spectrum. Another characteristic is the similarity of the results of the gauged and offset fits. This is not unexpected, as adding a constant number to the fit function or subtracting the same value from the spectrum should not make any difference. These gauged functions lead to a worse result of the χ^2 test as well, assuming, that the constant area before the peak does not result from any behaviour of the radioactive source but is caused by the detector. Therefore, it is not reasonable to put this constant into the fit function, as the fit should describe the natural characteristics of the source.
Another question arises, why the function (3.4) does not fit best to the spectrum, although it reflects the correlations of the theoretical decay. Due to the detector's energy resolution of about 1 keV, as described by the manufacturer, the two lines of 5.19 keV and 5.89 keV can not be detected perfectly on the right position and can even overlap, resulting in no accurate detection. Another explanation are the K_β X-rays at 6.4 keV. These X-rays just have a probability of about 3.4 % but can still have an impact on the spectrum by shifting the peak to higher energies.
The fit 3.1, where two Gaussian distributions with independent parameters are added in one function, are applied to all following analyses.

3.1.3 Background

The ^{55}Fe spectrum reveals a lot of noise. Especially in the beginning, one can identify an exponential drop of the differential counts. The counts stay constant until the peak what is also an unexpected course. These effects could have their origin in a background noise due to background radiation. To identify this background, a measurement without any source is conducted. The resulting spectrum is shown in figure 3.3. This measurement is done with a cooler temperature of 20 °C, a detector temperature of 20 °C and a time shutter width of 10 min.
The course has an exponential drop at the beginning and a linear slope in the area after 2 keV. Thus, a fit function of the form

$$f(E) = a \cdot \exp(-bE) + mE + n \tag{3.7}$$

with its error

$$\begin{aligned}\Delta f(E) =& \sqrt{\left(\exp(-bE)\cdot\Delta a\right)^2 + \left(-aE\exp(-bE)\cdot\Delta b\right)^2} \\ &+ \left(E\cdot\Delta m\right)^2 + \left(\Delta n\right)^2\end{aligned} \tag{3.8}$$

is used to characterise the background.

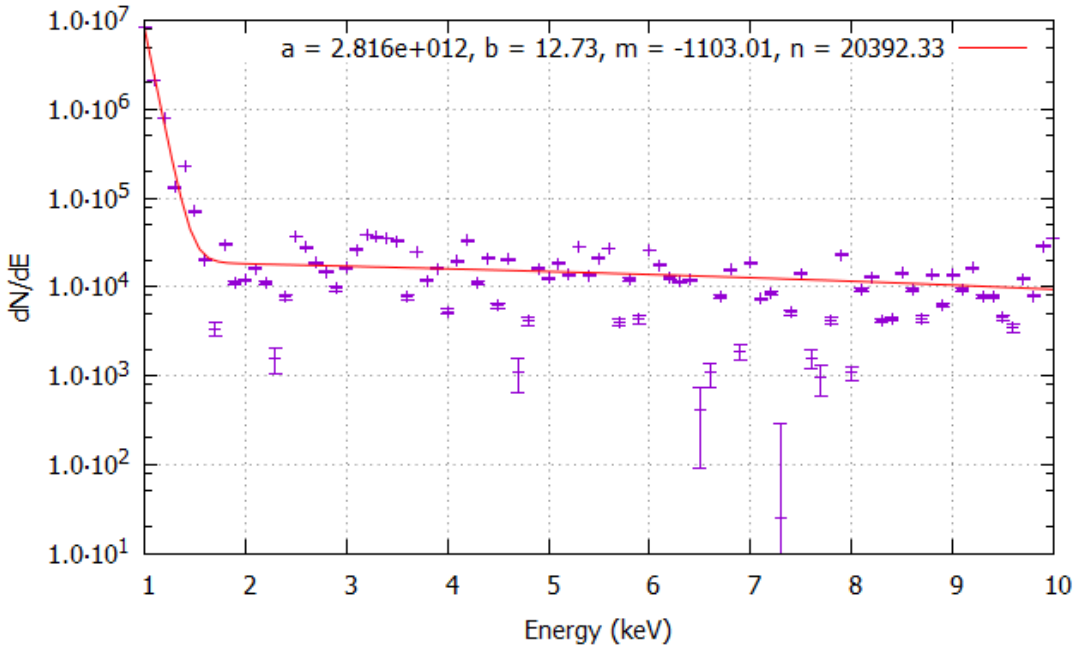

Figure 3.3: The background measurement is illustrated, recorded without any source, $T_{cooler} = 20\,°\mathrm{C}$, $T_{detector} = 20\,°\mathrm{C}$ and a time shutter width of 10 min. The spectrum is fit by the function $f(E) = a \cdot \exp(-bE) + mE + n$. The errorbars are plotted as well.

But this function shows a falling trend at the end of the spectrum. The fit makes a curve downwards, which may not represent the backgrounds behaviour for higher energies, hence there may be another, more appropriate function to fit the background. Looking at the logarithmic presentation of this spectrum, as pictured in figure 3.4, two linear parts, one at the beginning and one afterwards, can be identified. These characteristics should be fit well by two split power law functions of the form

$$f(E) = a \cdot E^{-k} \tag{3.9}$$

with the error propagation

$$\Delta f(E) = \sqrt{\left(E^{-k} \cdot \Delta a\right)^2 + \left(-aE^{-k} \ln(E) \cdot \Delta k\right)^2}. \tag{3.10}$$

In this case the first blue coloured fit can be used in the region from 1.0 keV to 1.6 keV and the red coloured fit can be applied for the higher energies.

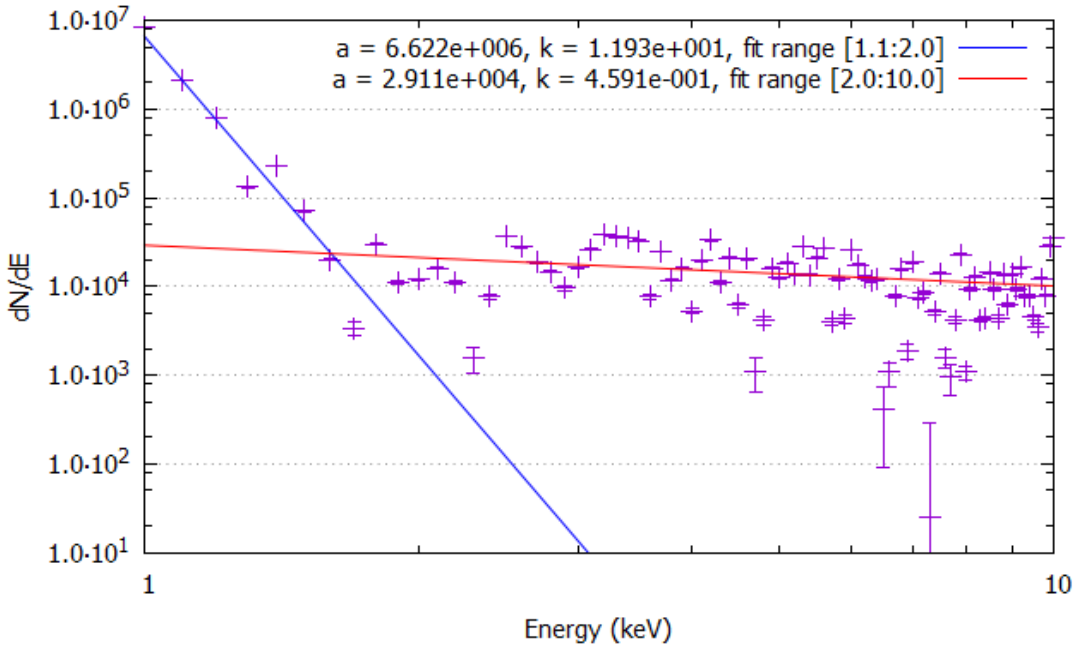

Figure 3.4: The background measurement is shown, recorded without any source, $T_{cooler} = 20\,°\mathrm{C}$, $T_{detector} = 20\,°\mathrm{C}$ and a time shutter width of 10 min. The spectrum is fit by two power law functions $f(E) = a \cdot E^{-k}$. The errorbars are plotted as well.

To look at the influence of the background on a ^{55}Fe spectrum, the spectrum is corrected with those two fit options. The parameters of the functions are

$$\begin{aligned} a &= (2.82 \pm 1.00) \cdot 10^{12} \\ b &= (12.73 \pm 0.35) \\ m &= (1103.01 \pm 547.60) \\ n &= (20392.30 \pm 3969.00) \end{aligned} \tag{3.11}$$

for the exponential/linear fit and

$$\begin{aligned} a_1 &= (6.62 \pm 1.05) \cdot 10^6 \\ k_1 &= (11.93 \pm 1.08) \\ a_2 &= (29114.20 \pm 9021.00) \\ k_2 &= (0.46 \pm 0.18) \end{aligned} \tag{3.12}$$

for the two power law fits.
The corrected spectrum is detected with a cooler temperature of 6 °C, a detector temperature of 20 °C and a time shutter width of 10 min while no collimator is installed. The background correction is conducted by subtracting the fits from the original spectrum:

$$\left(\frac{\mathrm{d}N}{\mathrm{d}E}\right)_{corrected} = \frac{\mathrm{d}N}{\mathrm{d}E} - f(E) \tag{3.13}$$

and its propagated error

$$\Delta\left(\frac{\mathrm{d}N}{\mathrm{d}E}\right)_{corrected} = \sqrt{\left(\Delta\frac{\mathrm{d}N}{\mathrm{d}E}\right)^2 + (\Delta f)^2}. \tag{3.14}$$

Applying these calculations, the spectra in figure 3.5 result. The uncorrected spectrum is depicted at the top, the exponential and linear corrected spectrum in the middle and the power law corrected spectrum on the bottom. All these spectra look very similar. Differences can be seen for low energies, where the exponential course slightly disappears in the corrected spectra. The counts in this area do not have their origin in the nuclear source but in the background radiation mainly appearing at low energies of about 1 keV. Thus, this region of the spectrum can be corrected by the background, although the other parts stay the same. This is not unexpected if one looks at the value of the background and the ^{55}Fe differential counts, which are about two orders of magnitudes higher. Regarding this ratio, the background spectrum should not have any visible influence on the ^{55}Fe spectrum. Hence, the constant noise before the peak must have its origin in something other than the background radiation.
An explanation for this noise could be a multiple particle detection due to Compton scattering. When a particle reaches the detector it can interact with material in terms of Compton scattering. Due to this, an incoming photon knocks out an electron of an atom in the material and both particles are detected. This effect can also run in the inverse way, where an incoming electron scatters with a photon and loses some of its energy to it. In both cases, more particles than the initial one are detected with lower energy due to the energy loss during the scattering. The Compton scattering can also appear in the nuclear source itself or in the medium between the source and the detector, which is air. This would also explain why the constant zone completely fades away after the peak. As the highest energetic particles emitted by the ^{55}Fe source have an energy of about 6.49 keV, nothing could produce any higher energetic particles above this energy. Accordingly, everything that is measured above this energy belongs to the background, whose intensity is so low that it is not visible in the spectrum.

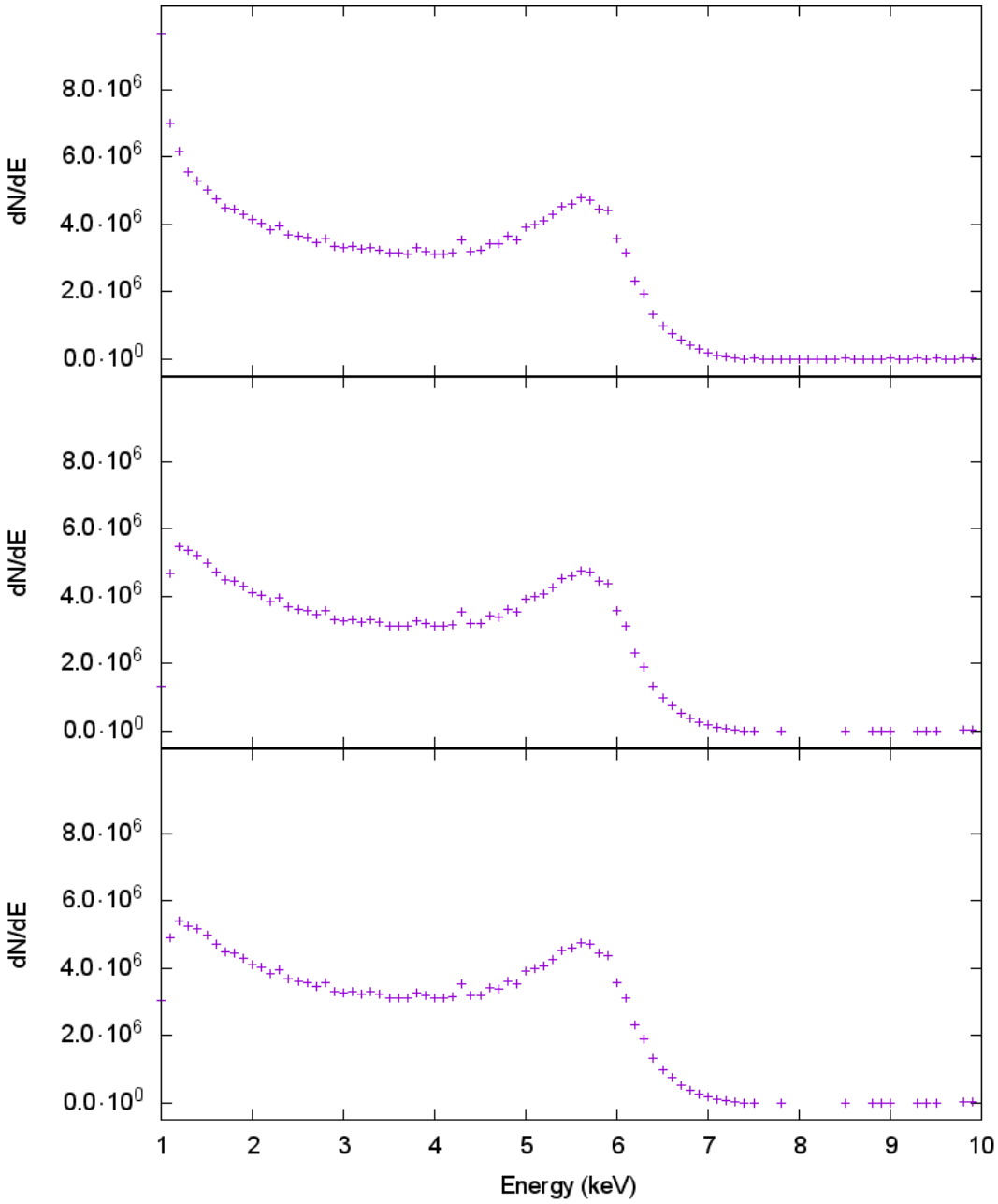

Figure 3.5: Different corrected differential spectra of ^{55}Fe are pictured, detected with $T_{cooler} = 6\,°C$, $T_{detector} = 20\,°C$ and a time shutter width of 10 min: on the top the uncorrected spectrum, in the middle the spectrum corrected with the exponential and linear fit and on the bottom the spectrum corrected with the two power law fits. The errorbars are plotted as well.

If the noise has its origin in the Compton Scattering caused by the 5.9 keV photons of the ^{55}Fe source, the compton edge can be calculated by equation (1.4). With an electron mass of $m_e c^2 \approx 511\,\text{keV}$, the maximum electron energy is $E_{e,max} = 133\,\text{eV}$. The corresponding photon energy after the scattering is $E'_\gamma = 5767\,\text{eV}$. Accordingly, no scattered electrons with an energy higher than 133 eV and no photons with an energy lower than 5767 eV should be detected. As this is not the case, the Compton scattering of the K_α photons does not lead to the noise, but other effects such as the inverse Compton scattering of the 5.2 keV Auger electrons could be an explanation. Nevertheless, the scattered photons can have an impact on the spectrum by shifting the peak to lower energies. Due to the low effective cross section of the Compton scattering, this effect is neglected in the analyses.
Comparing the background measurement and the region of the ^{55}Fe spectrum before the peak, both reveal similar courses: an exponential drop followed by a line. Thus, the counts in both measurements could have their reason in the same effect, for example some detector characteristics dependent on the amount of counts. These detector characteristics will be specified in chapter 3.1.6 by changing the measurement temperature.
Another notice of the background correction is, that some differential counts are overcorrected, so some measurement points do not fit in the spectrum and are lower than they are expected to be. This is caused by the statistics of the decay.
The background, used to adjust the spectrum, is recorded with a detector temperature of 20 °C. Based on the assumption that the background noise will lower with lower temperature, one can say that the background does not have any noticeable influence on the measurement, independent from the temperature. Thus, no background correction has to be done for the analysis of the data.

3.1.4 Different Collimators

The ^{55}Fe source is a cylindrical slice embedded in a carrier. Calculating the expected intensity that reaches the detector, a punctual source, which radiates in every direction, can be assumed. If this source is positioned centrally above the detector, the angular element captured by the rectangular detector with the side lengths b_1 and b_2, has to be identified. This angular element is calculated via the surface element of a globe in spherical coordinates:

$$\mathrm{d}\Omega = \mathrm{d}\varphi \cdot \sin\vartheta \, \mathrm{d}\vartheta. \tag{3.15}$$

Figure 3.6 shows a sidelong view of the setup with the punctual source above the detector with the distance s. One can identify the angle ϑ via

the tangens: $\tan\vartheta = x/s$. The length x, which specifies the distance from the center of the detector to its edges, has to be characterised. Looking at the right side of figure 3.6, where a top view on the detector is pictured, x can be determined by

$$x = \frac{b_2}{2\sin\varphi}. \tag{3.16}$$

So ϑ can be calculated by

$$\vartheta = \arctan\left(\frac{b_2}{2\cdot s\cdot\sin\varphi}\right). \tag{3.17}$$

In a final step the detector is subdivided in four equal parts similar to figure 3.6, so the angular element can be specified by

$$\begin{aligned} \mathrm{d}\Omega &= 4\cdot\int_0^{\pi/2}\mathrm{d}\varphi\cdot\int_0^{\arctan\left(\frac{b_2}{2\cdot s\cdot\sin\varphi}\right)}\sin\vartheta\,\mathrm{d}\vartheta \\ &= 2\pi - 4\cdot\int_0^{\pi/2}\cos\left(\arctan\left(\frac{b_2}{2\cdot s\cdot\sin\varphi}\right)\right)\mathrm{d}\varphi. \end{aligned} \tag{3.18}$$

The distance s from the source to the detector is composed of two lengths. The source is not directly placed on the end of the carrier. There is a placeholder for the installation of a collimator with a height of $(10 \pm 0.05)\,\mathrm{mm}$. Additionally, the active detector area is lowered into the case with a range of $(45 \pm 20)\,\mathrm{mm}$. Thus, the distance results in $(55.00 \pm 20.05)\,\mathrm{mm}$. The effective detector size is $31 \times 25\,\mathrm{mm}$, so b_2 is $31\,\mathrm{mm}$.

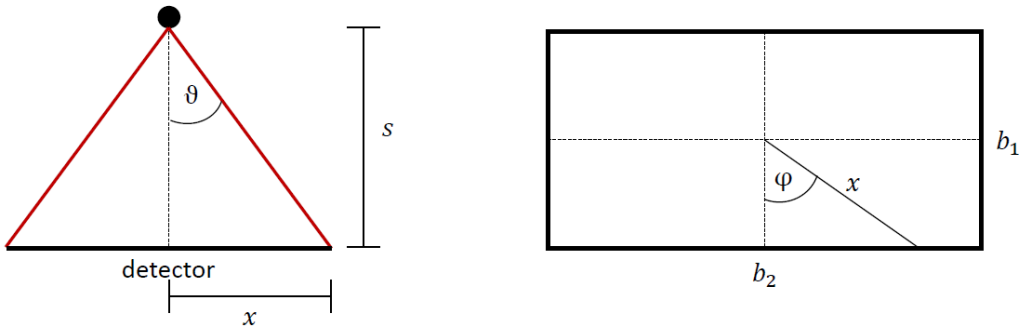

Figure 3.6: Presented are two drawings from different perspectives of the theoretical setup of the nuclear source on the detector. The source is presented without any collimator. The left drawing shows a side view, where s is the distance from the source to the active detector area and x the distance from the middle of the detector to its edges. The right drawing is a top view on the detector with side lengths $b_{1/2}$. ϑ and φ are spherical coordinates.

The installation of a collimator in front of the radioactive source changes the measured intensity. A collimator is a steel disc with a round hole of the radius r_{coll}. It may be assumed that every photon, which does not traverse this hole, is absorbed.
Because one can expect the collimator overlying on the source without any noteworthy space, the collimator simply reduces the angular element in which the radiation can reach the detector. Due to the small size of the collimator hole compared to the detector's dimensions, it is supposed that all particles leaving the collimator are detected. Thus, the angular element of the collimator has to be identified. Figure 3.7 shows the theoretical drawing of the setup. Because the hole is circular, the angle ϑ is not calculated further. According to this, the angular element can be set to

$$\begin{aligned} \mathrm{d}\Omega &= \int_0^{2\pi} \mathrm{d}\varphi \cdot \int_0^{\arctan\left(\frac{r_{coll}}{h_{coll}}\right)} \sin\vartheta \, \mathrm{d}\vartheta \\ &= 2\pi \left(1 - \cos\left(\arctan\left(\frac{r_{coll}}{h_{coll}}\right)\right)\right) \end{aligned} \tag{3.19}$$

with the collimator height $h_{coll} = (10 \pm 0.05)\,\mathrm{mm}$.
With these angular elements, the expected intensity is

$$I = I_0 \cdot \frac{\mathrm{d}\Omega}{4\pi} \tag{3.20}$$

as I_0 refers to the initial intensity of the source, if the entire radiation is detected in a globe around it with the angle 4π.

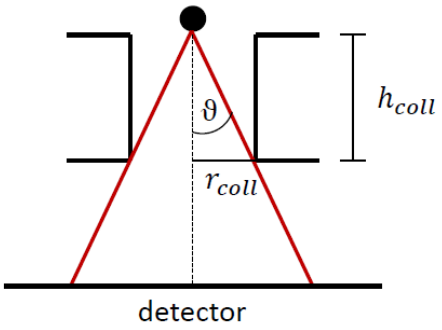

Figure 3.7: Presented is a drawing of a side view on the theoretical setup of the nuclear source on the detector. The source is presented with a collimator of the radius r_{coll} and the height h_{coll}. ϑ is a spherical coordinate.

Collimators with different diameters of 1 mm and 3 mm and the height $h_{coll} = (10 \pm 0.05)\,\mathrm{mm}$ are used to analyze their influences on the measurement. In the following four measurements the external cooling temperature

and the detector temperature are set to 20 °C. The spectra are recorded with a time shutter width of 10 min for each energy step.
Figure 3.8 shows the detected spectrum of the ^{55}Fe source with a 1 mm collimator. There is no actual structure visible. The reason for this is the disappearing of the differential counts in the statistics of the decay.
The spectrum with a 3 mm collimator is displayed in figure 3.9. The weak characteristics of the expected spectrum can be seen with a light rise of a peak at about 5 keV to 6 keV, although lots of spikes in the constant area from 2 keV to 5 keV are visible.
Figure 3.10 presents the detected spectrum without any collimator installed. The expected run of the spectrum with a well shaped peak at about 6 keV is clearly visible.
The parts of the different spectra caused by the background radiation, including the exponential drop at the beginning and a constant course after 7.5 keV with ca. 10,000 counts, are equal for each collimator.

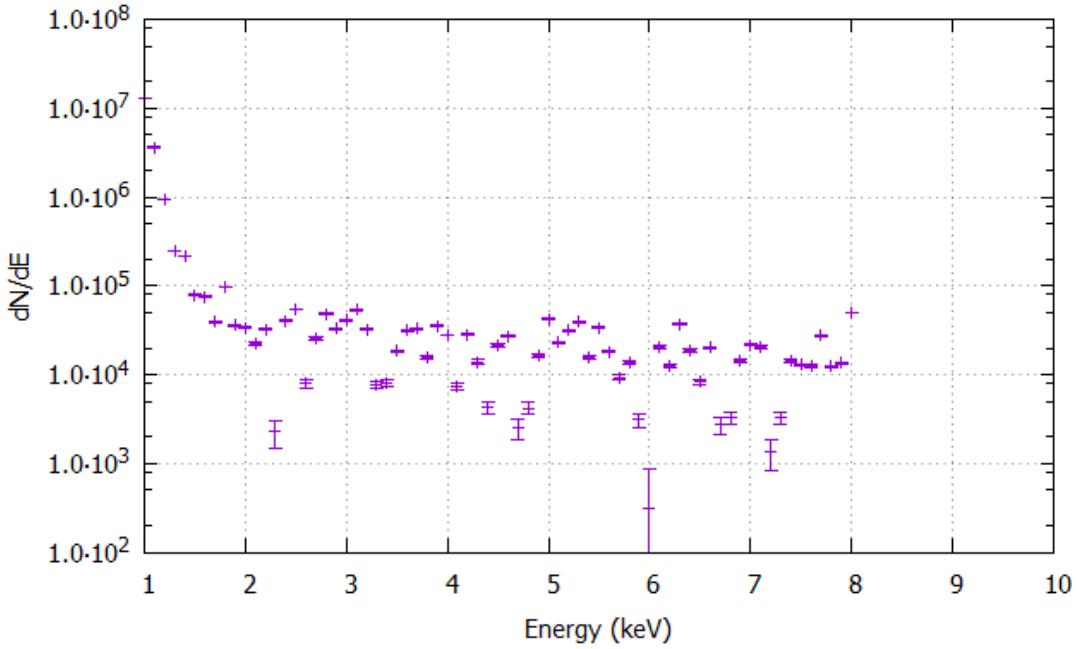

Figure 3.8: Presented is the logarithmic differential spectrum of ^{55}Fe, recorded with a 1 mm collimator, T_{cooler} = 20 °C, $T_{detector}$ = 20 °C and 10 min time shutter width. The spectrum is recorded from 1 keV to 8 keV. The errorbars are plotted as well.

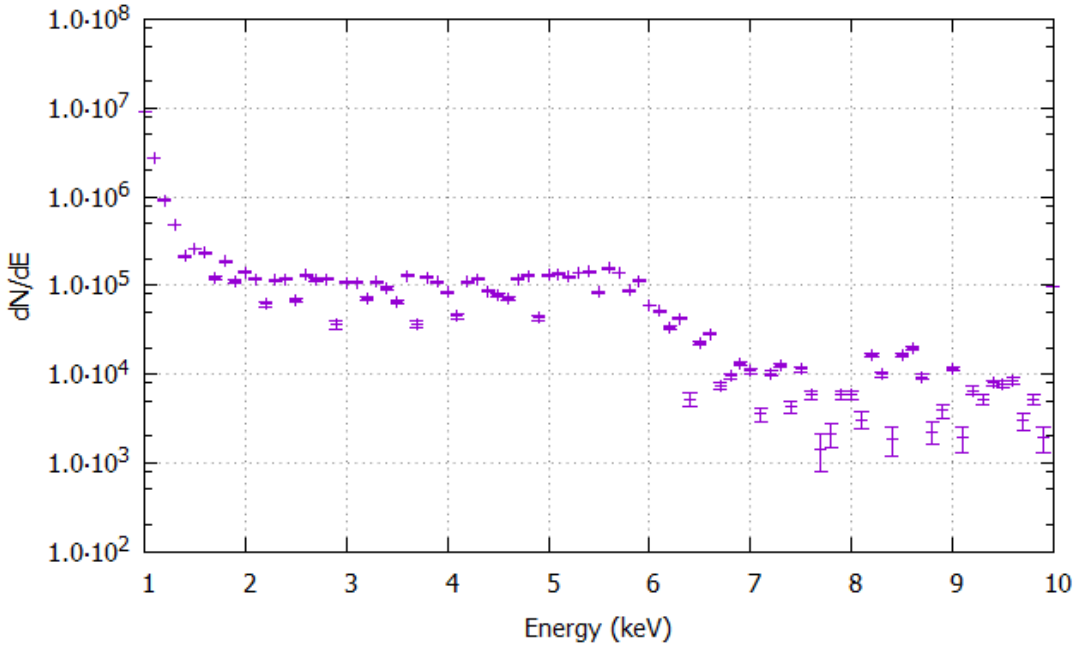

Figure 3.9: Presented is the logarithmic differential spectrum of ^{55}Fe, recorded with a 3 mm collimator, $T_{cooler} = 20\,°C$, $T_{detector} = 20\,°C$ and 10 min time shutter width. The errorbars are plotted as well.

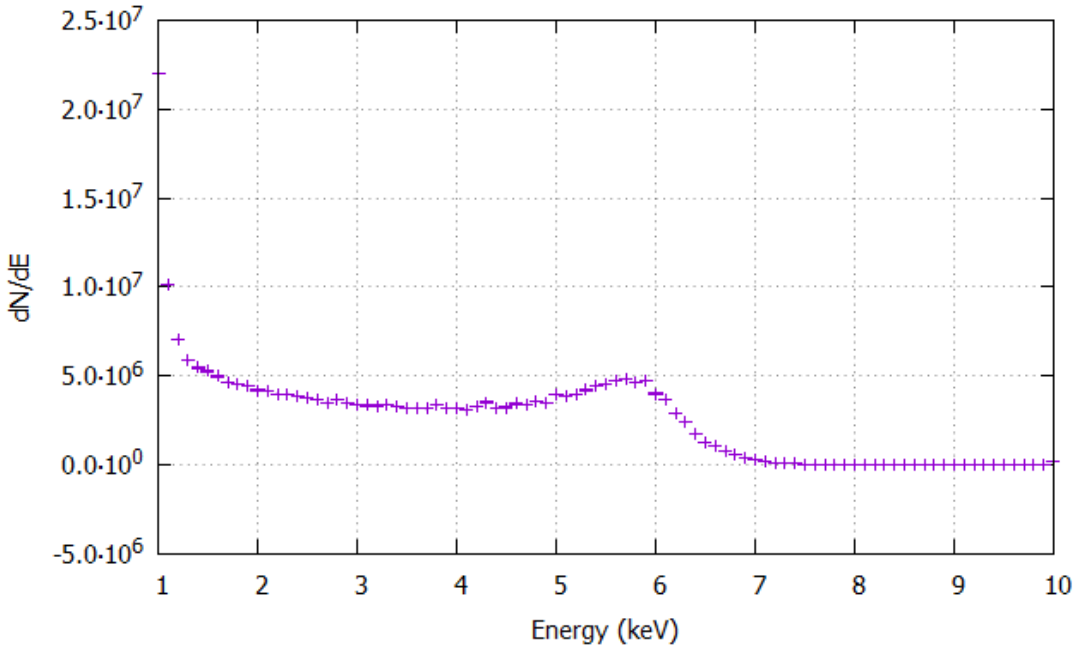

Figure 3.10: Presented is the linear differential spectrum of ^{55}Fe, recorded with no collimator, $T_{cooler} = 20\,°C$, $T_{detector} = 20\,°C$ and 10 min time shutter width. The errorbars are plotted as well.

One can compare the percentage of the theoretical calculated intensities with the measured ones. Hence, the areas before the peak are fit with a constant. The results of the constant fits and their ratios to the highest counts (the constant counts of the measurement without collimator) are listed in table 3.2. Regarding to the theoretical intensities, the integral in (3.18) is calculated numerically. As one can see, the theoretical and measured ratios fit to each other within the 2σ confidence interval.
In case of the 1 mm and 3 mm collimator, no higher statistics could be measured due to the maximum measurement time of 10 min per energy step. According to this, the statistics of these measurements are much lower than the statistics in the measurement without collimator. Thus, fitting the spectra in order to gain information about the energy resolution is not appropriate here.
Looking at the qualitative course of the spectra, the best results regarding a shaped and well fitted spectrum are archived with no collimator in front of the radioactive source. Hence, following measurements are conducted without any collimator.

Table 3.2: Presented are the percentages of the intensities for a 1 mm and 3 mm collimator in dependence of the intensity without any collimator. A comparison of the theoretical and measured values is shown as well.

d_{coll} (mm)	I_{theory} (MBq)	% of highest I	const. counts	% of highest counts
none	3.23640 ± 1.82433		3.47E+06 ± 7.01E+04	
1	0.02308 ± 0.00046	0.71 ± 0.40	29070 ± 3155	0.84 ± 0.19
3	0.20468 ± 0.00403	6.32 ± 3.57	96681 ± 6550	2.78 ± 0.06

3.1.5 Different Measurement Times

The second setting, which is adjusted, is the measurement time of the single energy steps. Such as the choice of the collimator, the measurement time has a direct effect on the number of counts. This influence should be linear. The purpose of studying the dependence on the spectra of the measurement time is to gain information about the statistics needed by the detector for an energetically dissolved measurement. This is important, as the detector should be used as a reference measurement of a particle beam. For this, the Pixirad has to be moved over the detection area to locate the beam. Thus, different measurements have to be conducted as short as possible.
The time shutter width of each threshold step is changed under a constant temperature and without any collimator. The cooler operates at 6 °C and the peltier of the detector is set to 20 °C, so the actual detector temperature

is about 14 °C. With these settings, spectra from 1 keV to 10 keV with a shutter width of 10 s, 30 s, 10 min, 2.5 min, 5 min and 10 min are recorded. The fitted spectra, pictured in the appendix in the figures A.10 to A.15, can be used to have a look at the characteristics of the peak counts as a function of the time shutter width. The fit results are listed in the appendices table A.1 and are displayed graphically in figure 3.11. As one can see, these counts rise linear to the shutter width with a gradient of $m = (7912 \pm 20)$ counts/s.

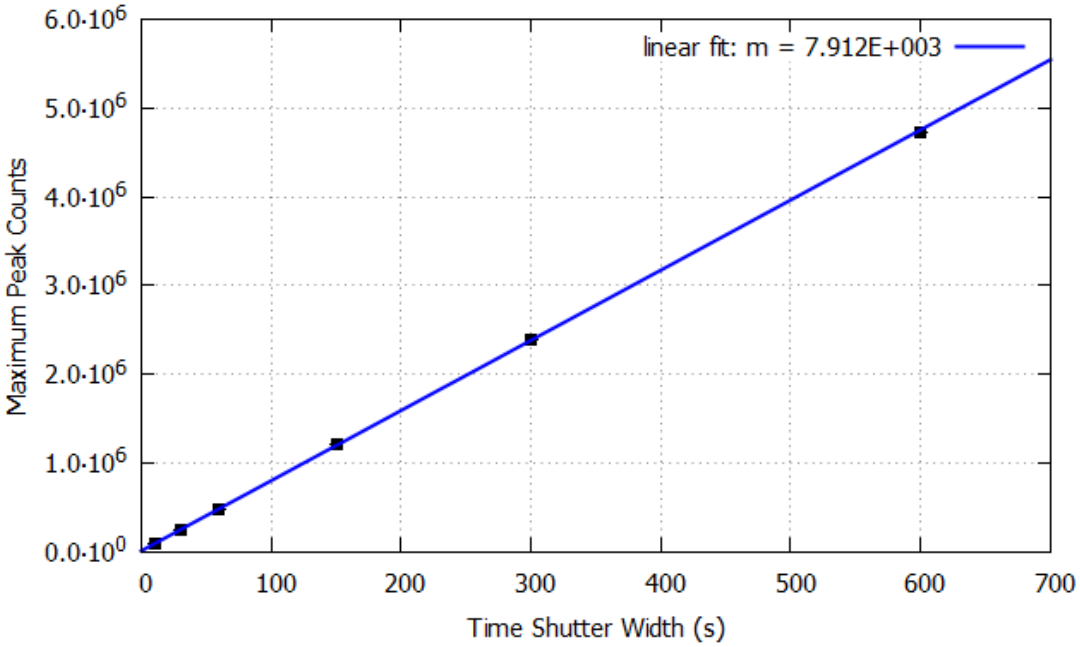

Figure 3.11: Presented are the measured peak counts as a function of the time shutter width, fit with a linear slope with the gradient m. The errorbars are plotted as well.

The means μ and standard deviations σ of the double Gaussian fit can be compared in order to see an influence of the measurement time on the quality of the measurement characterised by the energy resolution. The results of the fits are listed in the appendices in table A.2. The energy resolution Er of the two added Gaussian distributions within the fit function (3.1) can be calculated by

$$Er = \frac{FWHM}{\mu} = \frac{2\sqrt{\ln(2)}\sigma}{\mu}. \tag{3.21}$$

The energy resolutions Er_1 and Er_2 are illustrated as a function of the time shutter width in figure 3.12. Two different fits are conducted for

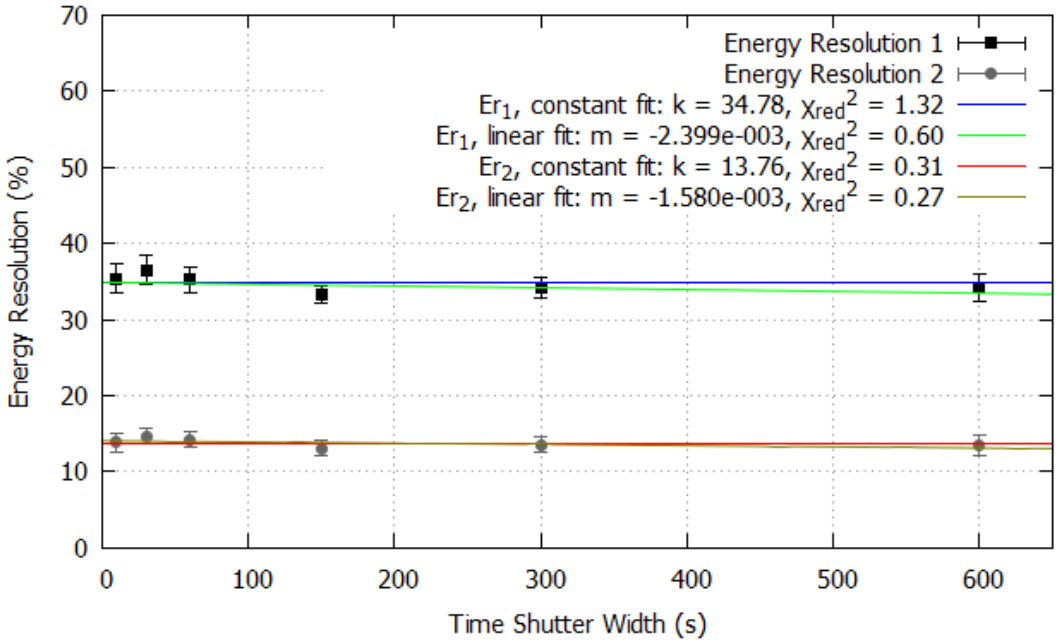

Figure 3.12: Presented are the two energy resolutions $Er_{1/2}$ of the fit function in dependence of the time shutter width. Both resolutions are fit by a constant of the value k and a linear slope of the gradient m.

every data series, a linear fit and a constant fit. Because the measurement values apparently stay constant, the two fits can be compared to find out, if the linear fit is necessary and reasonable or not. Especially in the case of Er_2, both χ^2_{red} results are lower than 1 and the constant fit hits every measurement entry, so the linear fit is not reasonable and just overcorrecting. Hence, the function is described sufficiently by the constant fit. Looking at Er_2, the χ^2_{red} of the constant fit is higher than 1, but due to the very low gradient m of the linear function, the constant can still be accepted as good approach.
Regarding these results, no significant influence of the shutter width on the fit results can be noticed for measurement times higher than 10 s. The energy resolutions stay constant with

$$Er_1 = (34.78 \pm 0.47)\,\% \tag{3.22}$$
$$Er_2 = (13.76 \pm 0.23)\,\%. \tag{3.23}$$

A measurement with a time shutter width of 1 s is recorded, resulting in no visible course of the spectrum. Hence, at shorter time shutter widths than 10 s the measured statistics are not high enough for a well shaped spectrum and the energy resolution deteriorates. Following measurements will be undertaken with a time shutter width of 1 min.

3.1.6 Different Temperatures

So far, a constant area before the peak exists in every single measurement, disappearing after the peak. This constant disrupts the fitting of the spectrum as explained in chapter 3.1.2. Some potential reasons for this noise have already been explained in chapter 3.1.3 but the different possibilities can still be limited. The reason of varying the detector temperature is to eliminate the possibility that leakage currents in the detector cause the noise.
Every semiconductor detector has a small leakage current leading to a temperature-sensitive noise. Mobil charge carriers can tunnel through the junction region causing a current pulse that is recognized by the detection electronics. The tunnel probability rises with the kinetic and thermal energy of the charge carriers. Hence, a higher temperature results in a higher probability, more tunneling carriers and finally in a higher leakage current and a greater noise.
Due to this effect, the temperature of the cooler and the peltier element are changed for several measurements in order to obtain a better shaped peak. As a quantity of the peak shape, the ratio between the peak counts and the constant counts can be calculated. Furthermore, the means and standard derivations are observed to receive the energy resolution as a function of the temperature.
Different series of measurements are recorded. The cooler temperature is varied at a constant peltier temperature (detector temperature) of 20 °C. The same measurement is conducted with the peltier switched off. The last recording is undertaken for a varied peltier temperature at a constant cooler temperature of -19 °C. As the actual detector temperature is measured by the detector, displayed in the LabView program and saved in the info file, the results can also be presented as a function of the actual detector temperature. Regarding this, temperature measurements in a range from -30 °C to 14 °C have been done and fit by the usual function 3.1. The analysed spectra are illustrated in the appendices in figures A.16 to A.25. The results of the energy resolutions are listed in the appendices in table A.3. The percentage of the peak to the constant counts are shown in the appendices in table A.4. Both measurement series are presented as a plot in the figures 3.13 and 3.14 as well.
The energy resolutions show the same behaviour as for different measurement times. The χ^2_{red} results of the Er_2 fits are both lower than 1, hence the constant fit can be used describing the characteristics. Considering Er_2, the χ^2_{red} of the constant is higher than 1, but due to the low gradient m of the linear fit, the constant can be used to characterise the data. Nevertheless, both energy resolutions show a weak rising trend, hence they improve with lower temperature, as expected.

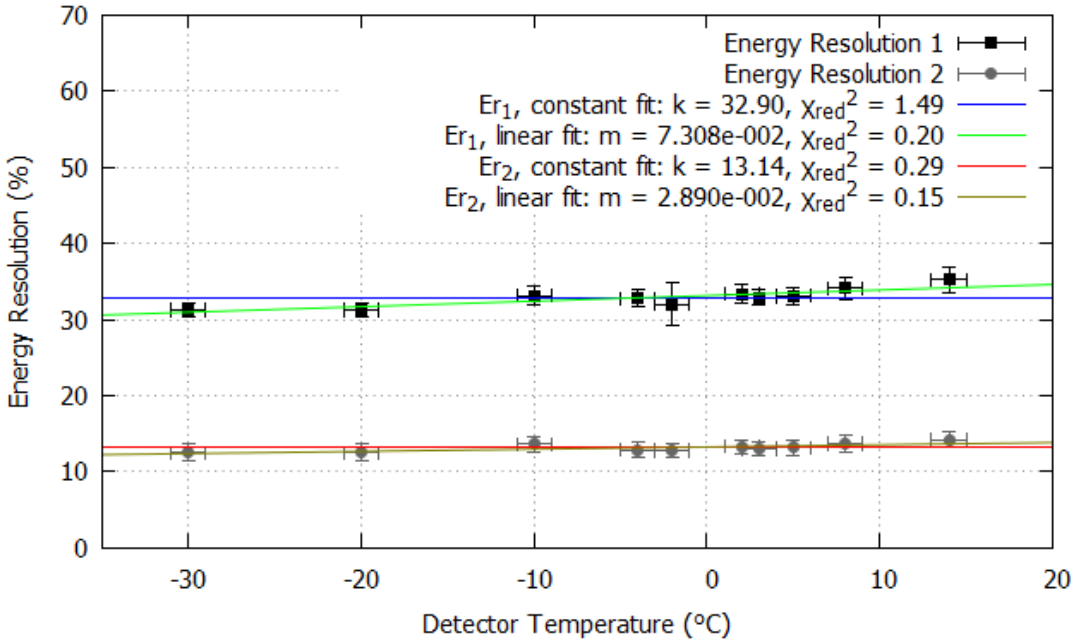

Figure 3.13: Presented are the two energy resolutions $Er_{1/2}$ of the fit function in dependence of the detector temperature displayed by the program. Both resolutions are fit by a constant of the value k and a linear slope of the gradient m.

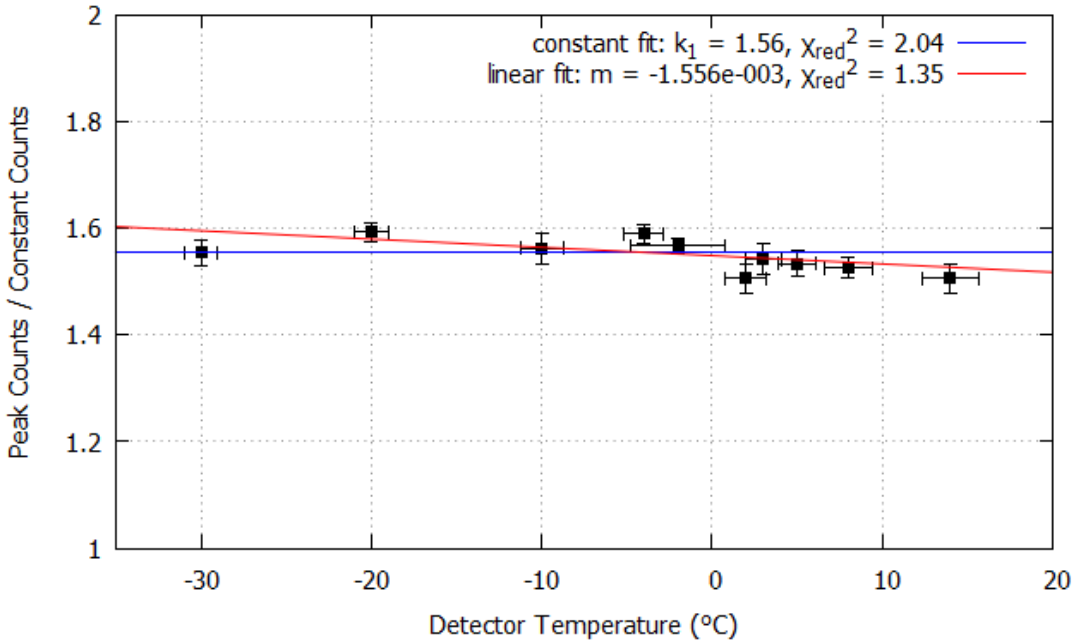

Figure 3.14: Presented are the peak counts divided by the constant counts before the peak in dependence of the detector temperature displayed by the program. The spectrum is fit by a constant of the value k and a linear slope of the gradient m.

In the case of the ratio of the peak counts and the constant counts, the constant fit does not hit every point. Nevertheless, the χ^2_{red} results are both close to 1, so the constant fit is still a close approach to the measurement. Neither the energy resolution nor the peak/constant ratio change with different detector temperatures. Due to the detector's operating temperature range from -40 °C to +40 °C, the energy resolution or measurement quality of the detector is independent from the detector temperature. It neither makes a difference if the cooler temperature is varied at a constant peltier temperature or if the peltier temperature is changed at a constant cooler temperature. Thus, the detector's measurements are independent from any environmental influences in this temperature range.
Another conclusion following from this measurement is that the constant area before the peak is not caused by any leakage current from the detector. Yet, other detector characteristics dependent on the readout of the counts, can be a reason for the noise. The most probable reason is the array arrangement of the individual detector pixels. If a particle does not completely hit a pixel and just hits its edge, some of the particle's energy can not be detected. If the pixels are not arranged directly next to each other, this energy is lost in the blank space between the pixels. Assuming no existing space and contacting pixel edges, the particle's energy is split among the pixels. In both cases, lower energies than the initial energy of the particle are detected. Another explanation could be cross talk of the detectors. Before the digital readout of a current pulse in a pixel, parts of the signal can be spread over the neighbour detectors. Usually the cross talk signal is about 1 % of the original signal and all neighbour pixels would detect it. Accordingly, the noise of the spectrum should be mostly distinct in the area of lower energies.
However, the multiple particle detection, generated by the Compton scattering of the Auger electrons, remains as another possible reason for the background noise.
Looking at the fit results again, the relation of the peak to the constant area is constant with

$$\frac{peak\ counts}{constant\ counts} = 1.56 \pm 0.01. \tag{3.24}$$

The energy resolutions of the fit function, including the addition of two independent Gaussian distributions, have the constant values

$$Er_1 = (32.90 \pm 0.39)\,\% \tag{3.25}$$
$$Er_2 = (13.14 \pm 0.17)\,\%. \tag{3.26}$$

3.1.7 Picture of the ^{55}Fe source

Figure 3.15 shows an example of a picture taken by the Pixirad. It represents a picture of the ^{55}Fe source with a 3 mm collimator at a threshold of 4 keV. It clearly identifies the source and its circular structure.
As the detector counts every particle with a higher energy than the threshold, the source will definitely be visible when the threshold is lower than the energy of the source's characteristic lines, but if the threshold is in the range of the background radiation, the counts of the source will get lost in the background. In this case the nuclear source will not be visible in the picture. As a conclusion, the picture should be taken with a threshold between the background range (1 - 2 keV) and the characteristic energies of the measure source.

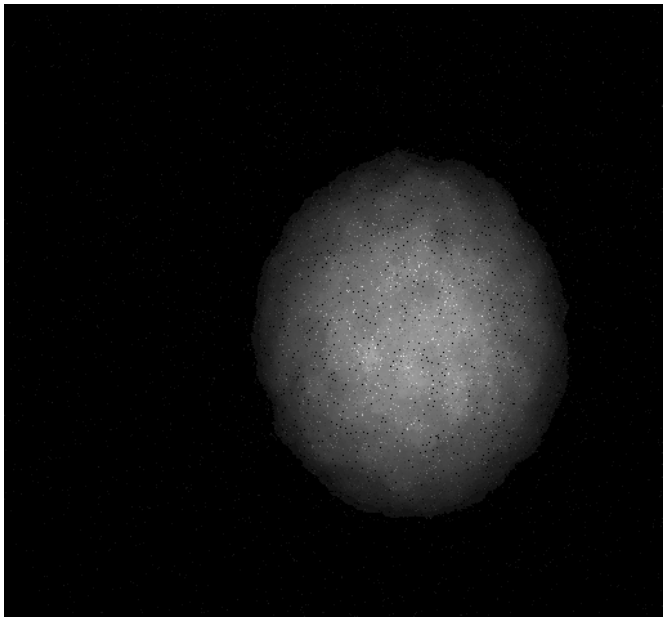

Figure 3.15: A picture of the ^{55}Fe source is illustrated, recorded with a 3 mm collimator $T_{cooler} = 20\,^{\circ}\mathrm{C}$, $T_{detector} = 20\,^{\circ}\mathrm{C}$ and 10 min time shutter width. The picture is taken at a threshold of 4 keV. The image contrast is edited.

3.2 ^{241}Am

^{241}Am is the second measured source. Four different spectra are recorded with different energy step widths, which are explained in the following chapter.

3.2.1 Spectrum of ^{241}Am

In the measured energy range from 20 keV to 70 keV, five different peaks are expected; three main peaks at 59.54 keV, 26.34 keV and 33.16 keV and two lower peaks in the area of 20.99 keV to 22.681 keV and in the area of 37.11 keV to 41.93 keV. With constant cooler and detector temperatures of -10 °C and -30 °C and a time shutter width of 1 min, four different measurements are undertaken from 20 keV to 70 keV by varying the energy step widths. The recorded spectra with the step widths 0.1 keV, 0.2 keV, 0.5 keV and 1.0 keV are pictured in figures 3.16 to 3.19. Because all the peaks are far enough away from each other, they are fit by a single Gaussian distribution.

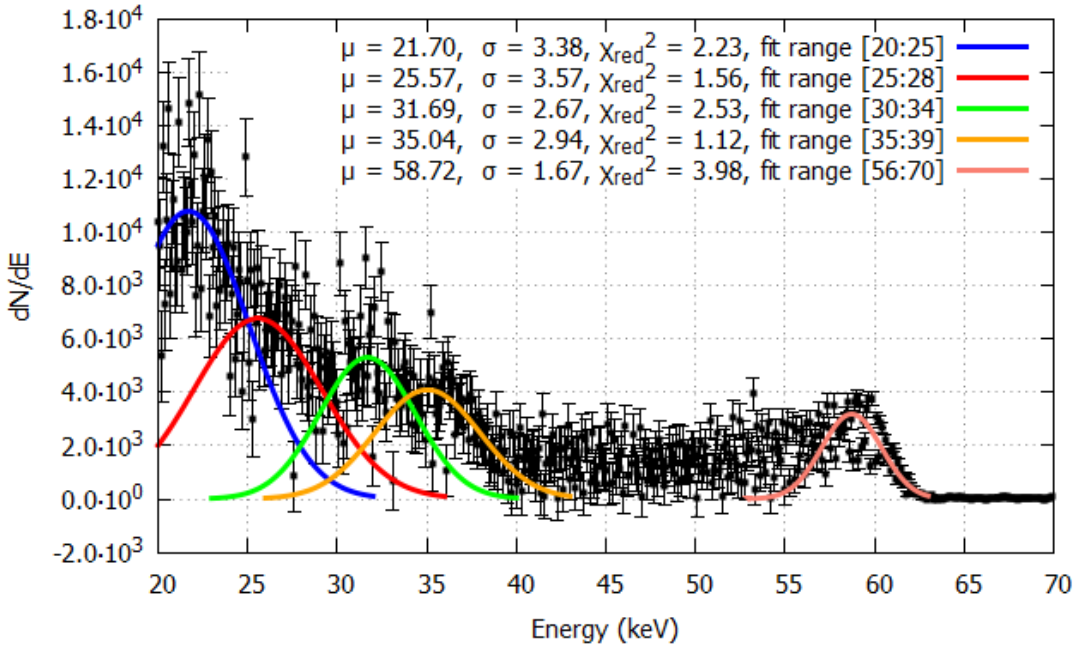

Figure 3.16: Presented is the differential spectrum of ^{241}Am, recorded with an energy step width of 0.1 keV, $T_{cooler} = -10\,°C$, $T_{detector} = -30\,°C$ and 1 min time shutter width. The errorbars are plotted as well.

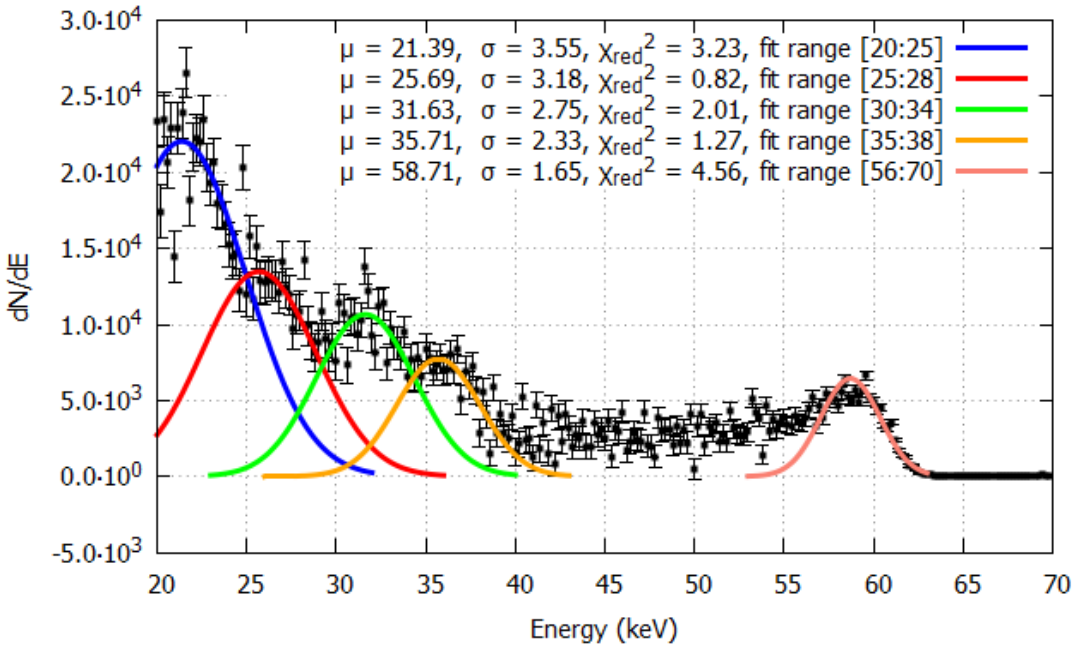

Figure 3.17: Presented is the differential spectrum of ^{241}Am, recorded with an energy step width of 0.2 keV, $T_{cooler} = -10\,°C$, $T_{detector} = -30\,°C$ and 1 min time shutter width. The errorbars are plotted as well.

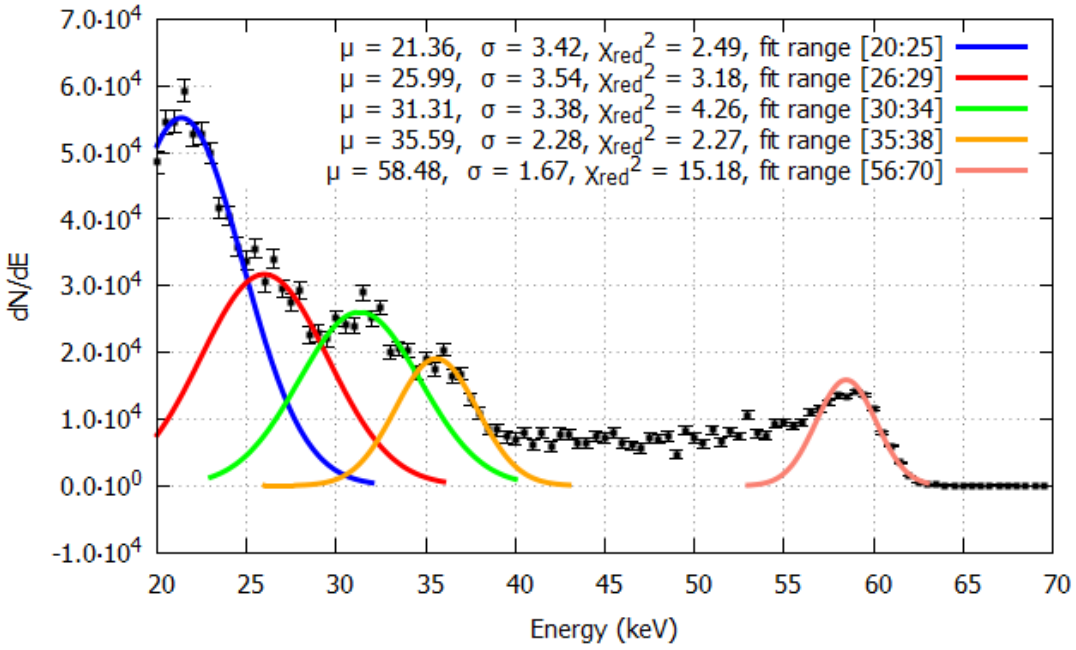

Figure 3.18: Presented is the differential spectrum of ^{241}Am, recorded with an energy step width of 0.5 keV, $T_{cooler} = -10\,°C$, $T_{detector} = -30\,°C$ and 1 min time shutter width. The errorbars are plotted as well.

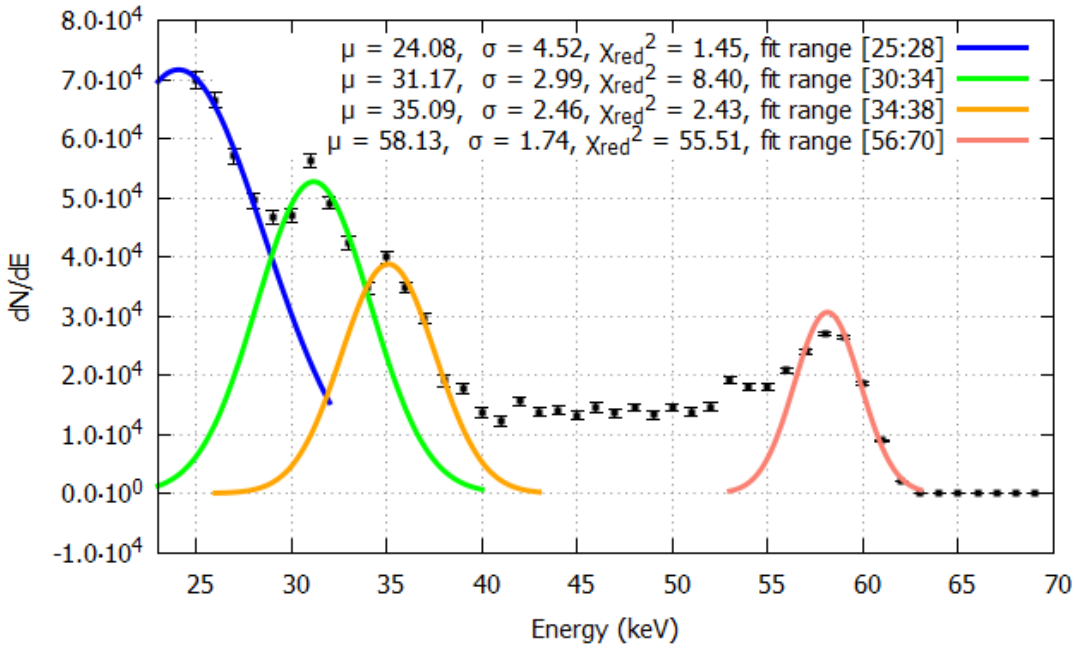

Figure 3.19: Presented is the differential spectrum of ^{241}Am, recorded with an energy step width of 1.0 keV, $T_{cooler} = -10\,°C$, $T_{detector} = -30\,°C$ and 1 min time shutter width. The spectrum is recorded from 25 keV to 70 keV The errorbars are plotted as well.

Looking at the different spectra, the five expected lines can be identified. Not every line is a well shaped peak. The peak at 26.34 keV for example, can be specified because the spectrum stops falling and stays constant for a short area. Furthermore, one does not receive any information about the intensity of the lines. The peaks sink with higher energy. This is the same effect as seen at the ^{55}Fe spectra. Due to some multiple counting by the detector, particles have an influence on lower energetic counts. One can see this characteristic very well in the area between the 36 keV and 59.54 keV line. After the 36 keV peak, the counts fall down to a constant area caused by the the 59.54 keV gammas, which have a constant impact on the counts of every lower energy level.
Due to the measured energy range in the 1.0 keV measurement from 25 keV to 70 keV, the first line at about 21 keV is not detected. The fit results are listed in the appendices in tables A.5 and A.6 in terms of the means and the standard deviations. Such as the course of the spectra, the fit results are very similar for every measurement and do not show any specific trend. Only the second line in the 1.0 keV measurement deviates from the other results as the fit range begins at 25 keV and some points are missing for a accurate fit. According to the similar means and standard derivations, the choice of the energy step width does not have an impact on

the analytic results. However, taking into account the individual graphs, differences are revealed. The smaller the step width is, the more blurred the course is. Additionally, the differential counts value decreases with a smaller step width. These two effects can be explained by the way the spectrum is computed. For each value, the total counts of two following energy steps are subtracted. The smaller the interval of these two energy steps is, the smaller the differential counts become, the more the statistics of the decay flow into the spectrum. But if the energy step width is chosen too wide, one may lose information about the spectrum. Figure 3.19 shows the recorded spectrum with energy steps of 1.0 keV. One can see, that the course of the spectrum is not as clearly visible as in the 0.5 keV step spectrum in figure 3.18, especially regarding the 33 keV line. Thus, the energy step width has to be set by instinct, considering the best percentage of accuracy and information.

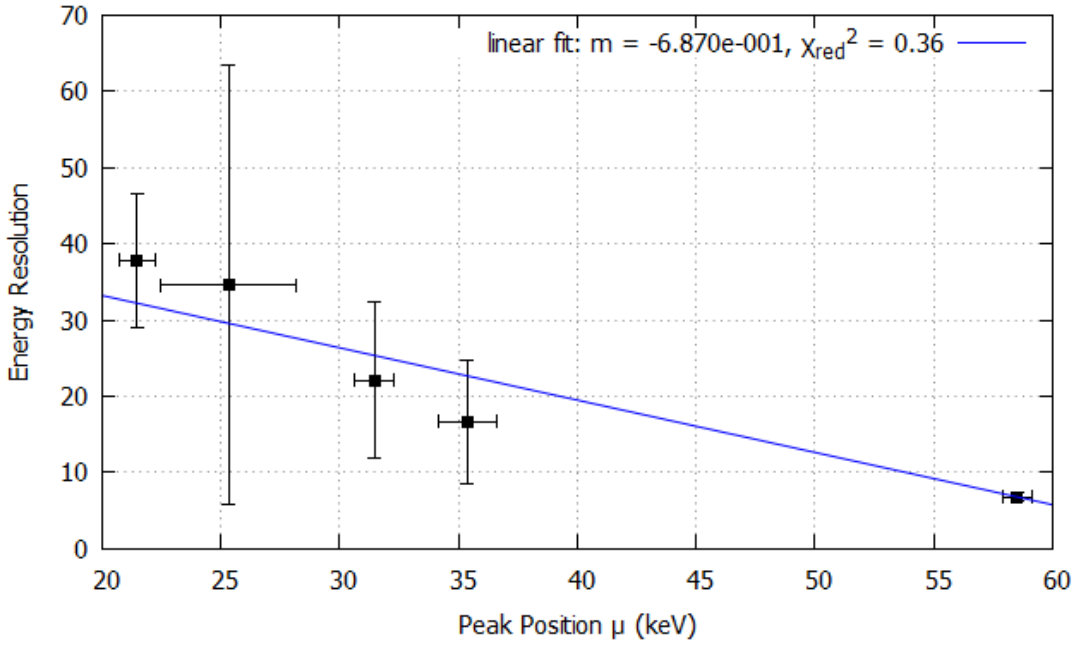

Figure 3.20: Presented is the energy resolution Er of the different ^{241}Am peaks in dependence of the peak position. A linear fit with the gradient m is applied.

To obtain information about the dependence of the energy on the detector's energy resolution, the averages of the means μ_n and the standard derivations σ_n of the different peaks can be applied to calculate the energy resolution of the peaks dependent on their position μ_n. The result is

pictured in figure 3.20. One would expect the energy resolution Er rising with higher energy. Yet, the opposite is true and Er decreases linear with the energy. This can be explained by the multiple counting of the detector as well. The more peaks exist at energies above some peak's energy, the more counts are generated by the higher energetic particles. Due to this effect, the peaks are more blurred at lower energies and therefore, the energy resolution decreases at the lower energy lines.
Another conclusion that can be drawn out of the dependence of the energy step width on the differential counts is that no statement about the absolute value of the detected counts and the measured intensity for the radioactive source can be made. Instead, one has to take a look at the total counts and not the differential counts considering that even the total counts are affected by the multiple counting.
But despite all these inaccuracies, the expected lines could be identified in every measurement in the right position including the standard derivation.

4 Conclusion and Outlook

In this elaboration the characteristics of the Pixirad I detector were tested. In order to do this, especially its performance at different parameters, such as the statistics, the measurement time and the temperature, was tested. The performance was evaluated based on the energy resolution and the qualitative trend of the differential spectra.

With the succesfully reprogrammed software the detector is now able to detect a whole differential spectrum within one measurement. The general courses of the measured spectra are satisfying, as the expected peaks can be identified. Nevertheless, an undesired effect is visible. There is no possibility to prevent the multiple counting by the detector. This multiple counting generates a constant noise below every peak in the spectrum. Many detected particles cause not only one but many counts on lower energies and therefore, have a constant influence on the differential counts of lower energies. Due to this effect, one can not make any conclusion about the total intensity of a peak and different peaks in one spectrum will lower in their intensity with higher energy. This effect does not change with lower or higher statistics of the counts and it does not change with lower temperatures. The multiple counting can have different possible reasons:

1. The initial particles/photons can transfer some of their energy to other particles by Compton scattering in the source, the air or the detector. In this case, many particles/photons are not detected as one, but they are detected several times with a fragment of the total energy.

2. Another option are detector characteristics, which cause multiple readout of one particle.

    a) Due to the array arrangement of the detector pixels, a particle could hit the edge of an individual pixel or two neighbour pixels at the same time. In both cases lower energies than the initial one are detected.

    b) Before the digital readout of a current pulse in a pixel, parts of the signal can be spread over the neighbour detectors, called cross talk. All neighbour pixels would detect a lower signal.

(1.) and (2.b) can be excluded due to the conducted measurements. Compton scattering of photons mainly appears in the area of $\hbar\omega > 0.5\,\mathrm{MeV}$. As these energies are not reached with the available sources ^{55}Fe and ^{241}Am, this effect does not have a large influence. Yet, the 5.19 keV Auger electrons emitted by ^{55}Fe, can cause inverse Compton scattering and therefore, the noise before the peak. As the same noise can be identified in the ^{241}Am spectrum, which is only generated by photons, the Auger electrons can be excluded as an explanation as well.
Assuming cross talk causing the constant noise, about 1 % of the original signal would be spread over the neighbour pixels. Thus, the noise should be mostly present in the area of lower energies. Especially in the ^{241}Am spectra a constant area before the highest energetic peak is visible. Accordingly, cross talk does not apply as a reasonable explanation.
Regarding all these considerations, the pixel arrangement of the Pixirad I remains as the most probable reason for the multiple counting. To prevent the multiple detection, the Pixirad has to offer another detection mode. In this mode, not all of the integrated counts from every individual pixel should be detected. For example, the charge of one pixel and its neighbours should be summed up, so the resulting value is the energy of the initial particle. Newer Pixirad models already provide a mode, including this adjustment and according to the Pixirad website the resulting spectra have a lower noise.
Due to the multiple counting, no final statement about the detector's energy resolution can be made. The energy resolutions improve with higher energy in all spectra of both nuclear sources. This is the opposite of what was expected before. However, this characteristic can be explained by the multiple counting as well. The more peaks exist at energies above some peak's energy, the more counts are generated by the higher energetic particles. Due to this effect, the peaks are more blurred at lower energies and therefore, the energy resolution is worse at the lower energy lines. According to this, the best conclusion about the hardware energy resolution of the detector can be made by the highest energetic ^{241}Am line at $(58.51 \pm 0.62)\,\mathrm{keV}$, as this peak is not influenced by any noise. The energy resolution of this peak has an average of $(6.8 \pm 0.6)\,\%$.
Inspite of this incident, the peaks of the recorded spectra could be identified at the rigth positions. The position and the energy resolution of these peaks did not change with the variation of the temperatures. Based on this finding it can be concluded that the environmental factors do not have any great influence on the characteristics of the Pixirad. Yet, it should always be ensured that the measured intensity of the nuclear source is at a certain height, so that the differential counts are not lost in the background noise or the statistics of the decay. The differential counts of the background are up to 17 counts/s. In addition one has to set a reasonably chosen energy step width. Especially the spectra of ^{241}Am show that a very low step

width can result in high fluctuation and a high step width can result in a loss of information.
Overall, the Pixirad I is a good choice for a reference measurement of TR-photons with energies up to 89 keV, as it can reliably detect the photons regardless of the surrounding conditions. Furthermore, the detector can easily locate the photon with its imaging sensors and therefore, one can identify the energy spectrum of a radioactive source on the right location.

A Appendices

A.1 Fitting of the ^{55}Fe spectrum

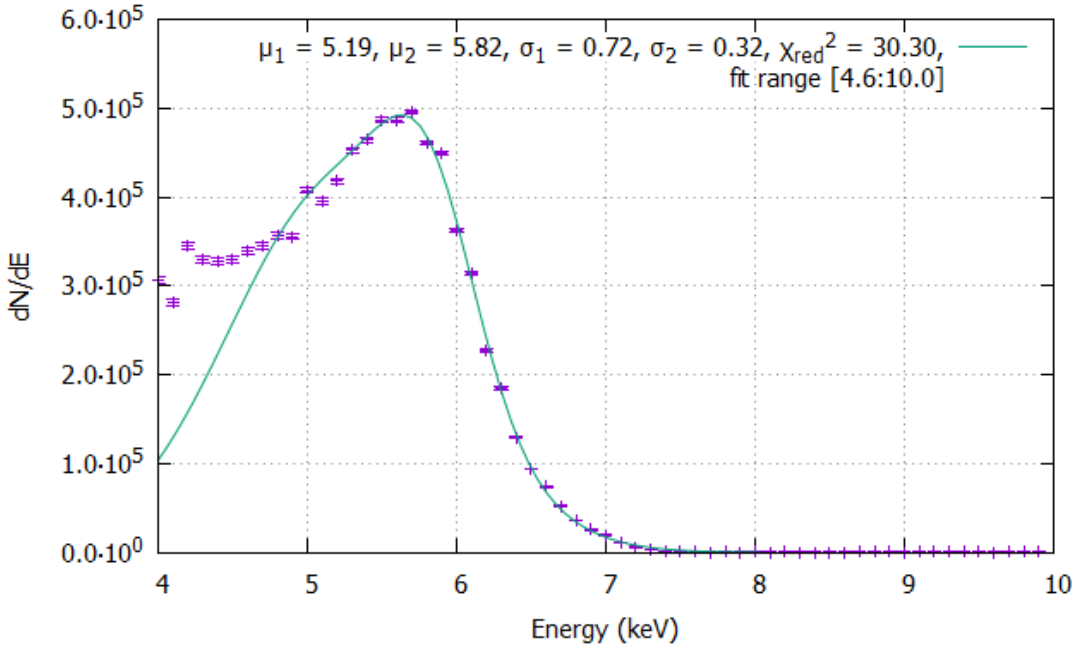

Figure A.1: The differential spectrum of ^{55}Fe, recorded with no collimator, $T_{cooler} = -15\,°\mathrm{C}$, detector cooling off and 1 min time shutter width. Fit by one function composed of the addition of two Gaussian distributions with independent parameters. The errorbars are plotted as well.

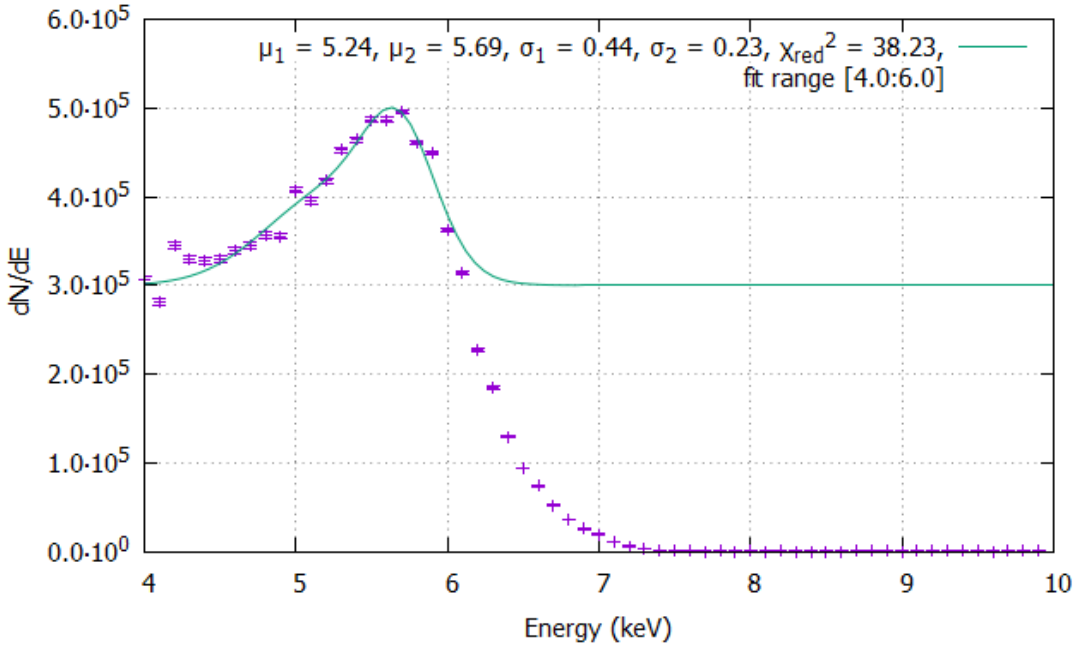

Figure A.2: The differential spectrum of ^{55}Fe, recorded with no collimator, $T_{cooler} = -15\,°C$, detector cooling off and 1 min time shutter width. Fit by one function composed of the addition of two Gaussian distributions with independent parameters. A constant offset of 300,000 is added to the function. The errorbars are plotted as well.

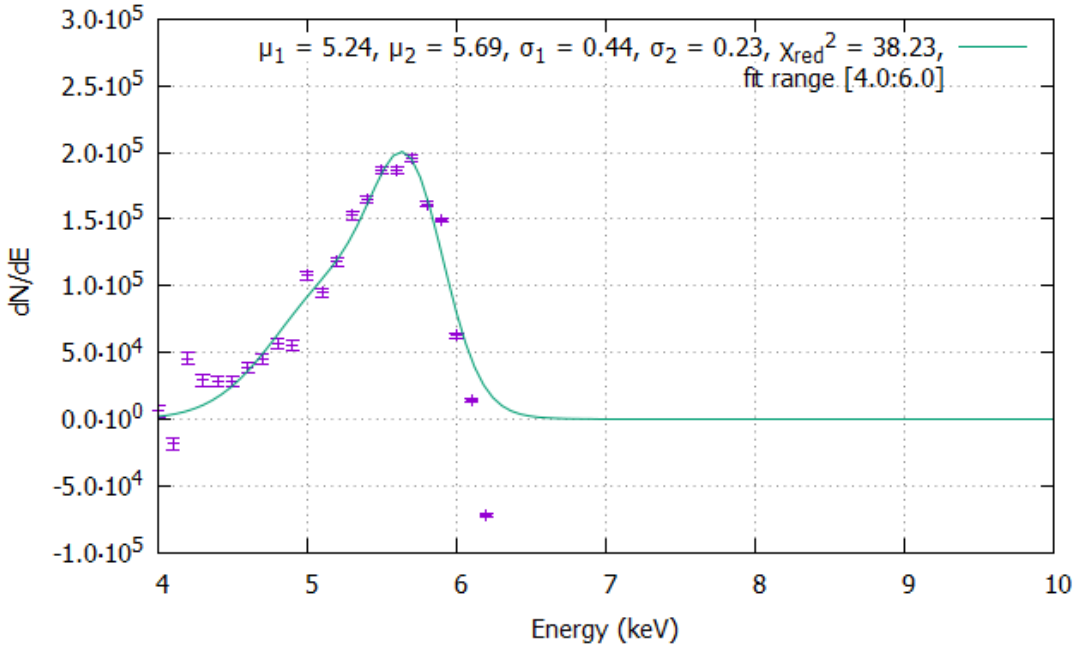

Figure A.3: The differential spectrum of ^{55}Fe, recorded with no collimator, $T_{cooler} = -15\,°C$, detector cooling off and 1 min time shutter width. Fit by one function composed of the addition of two Gaussian distributions with independent parameters. A constant value of 300,000 is subtracted from the whole spectrum. The errorbars are plotted as well.

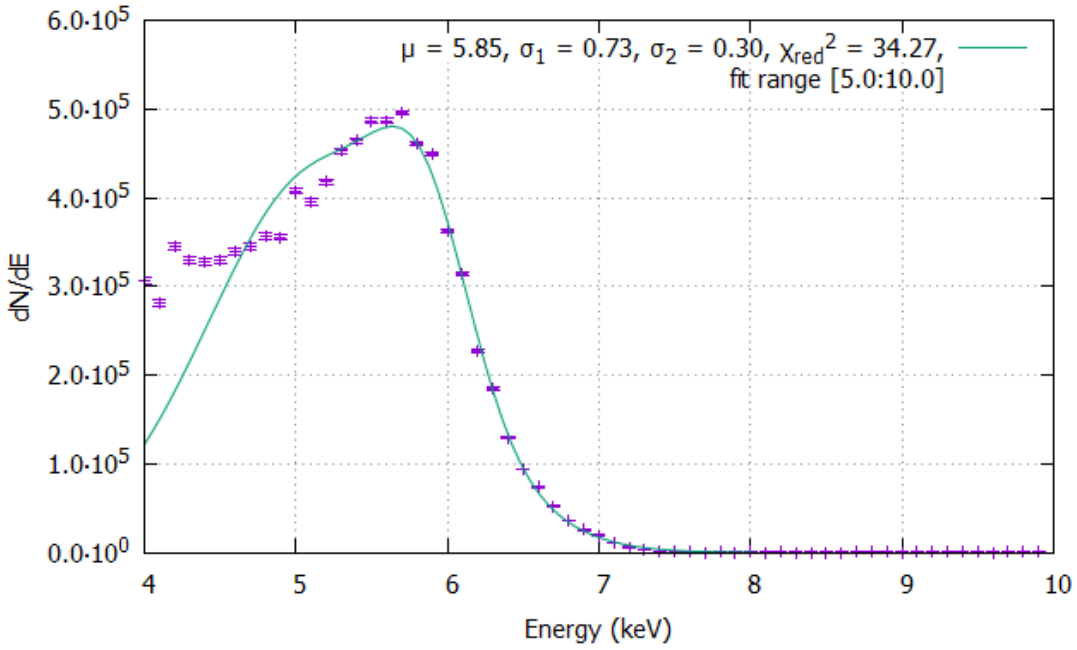

Figure A.4: The differential spectrum of ^{55}Fe, recorded with no collimator, $T_{cooler} = -15\,°C$, detector cooling off and 1 min time shutter width. Fit by two independent Gaussian distributions by one function composed of the addition of two Gaussian distributions with interdependent means and amplitudes. The errorbars are plotted as well.

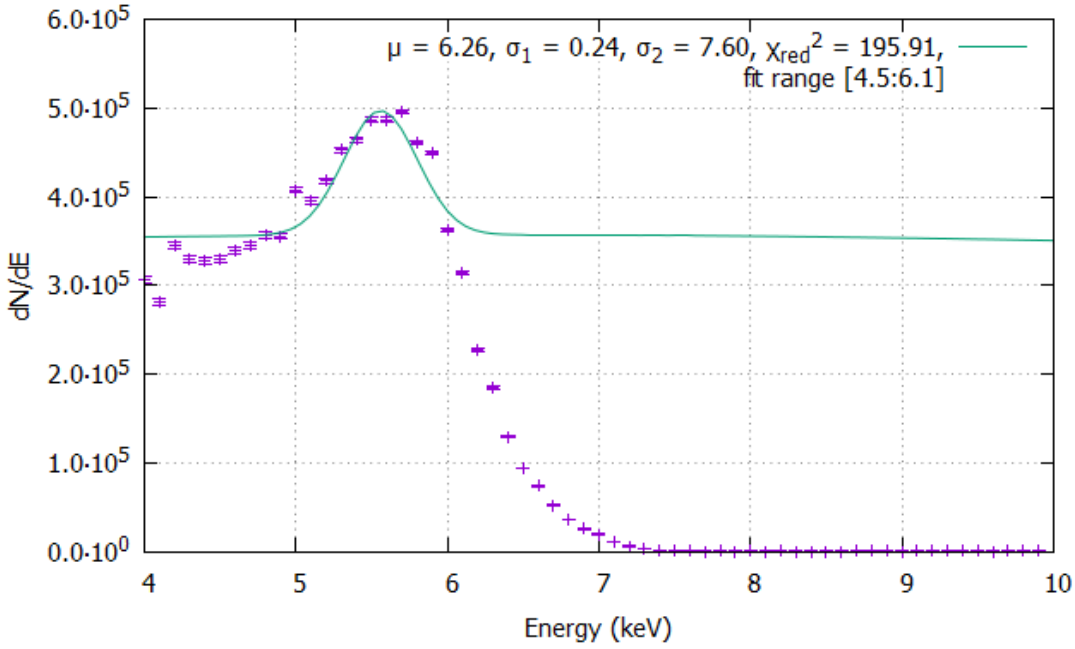

Figure A.5: The differential spectrum of ^{55}Fe, recorded with no collimator, $T_{cooler} = -15\,°C$, detector cooling off and 1 min time shutter width. Fit by two independent Gaussian distributions by one function composed of the addition of two Gaussian distributions with interdependent means and amplitudes. A constant offset of 300,000 is added to the function. The errorbars are plotted as well.

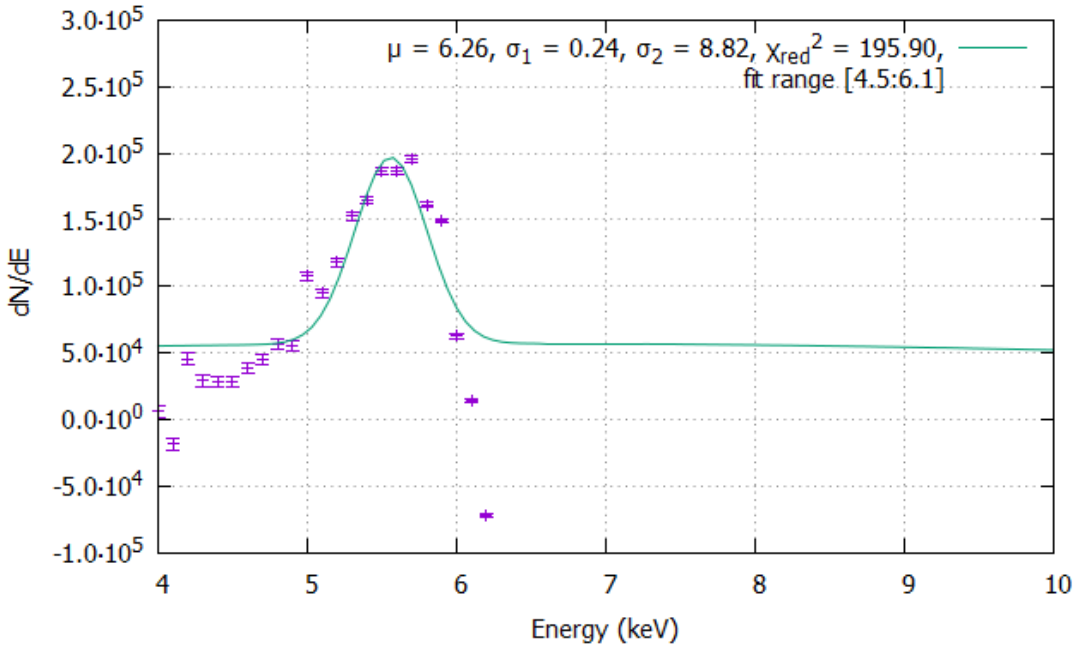

Figure A.6: The differential spectrum of ^{55}Fe, recorded with no collimator, $T_{cooler} = -15\,°C$, detector cooling off and 1 min time shutter width. Fit by two independent Gaussian distributions by one function composed of the addition of two Gaussian distributions with interdependent means and amplitudes. A constant value of 300,000 is subtracted from the whole spectrum. The errorbars are plotted as well.

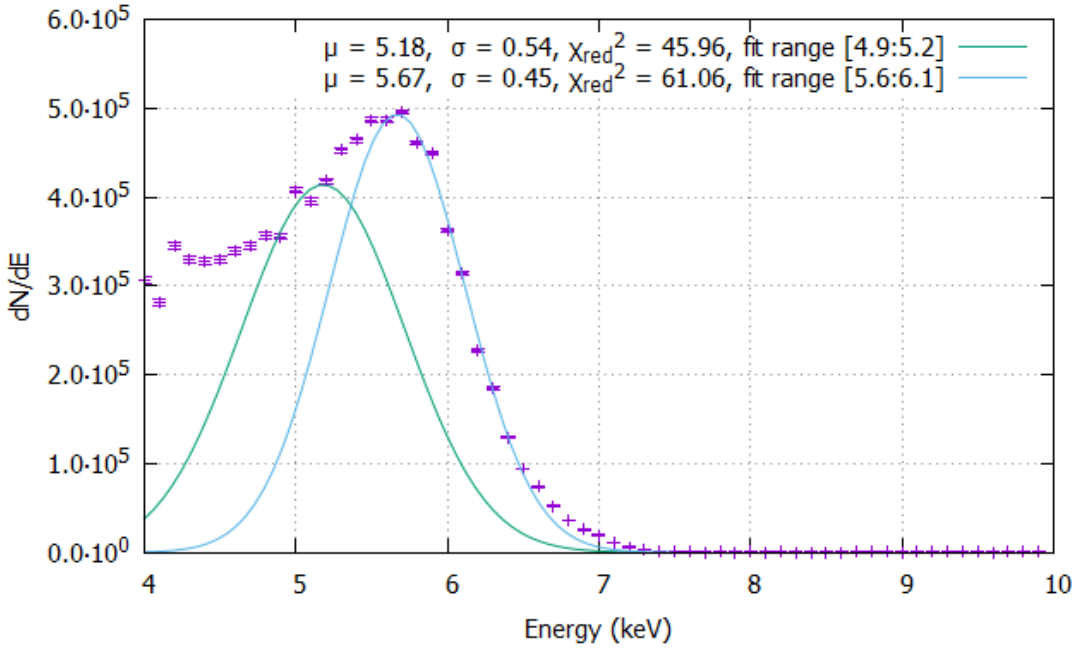

Figure A.7: The differential spectrum of ^{55}Fe, recorded with no collimator, $T_{cooler} = -15\,°C$, detector cooling off and 1 min time shutter width. Fit by two independent Gaussian distributions. The errorbars are plotted as well.

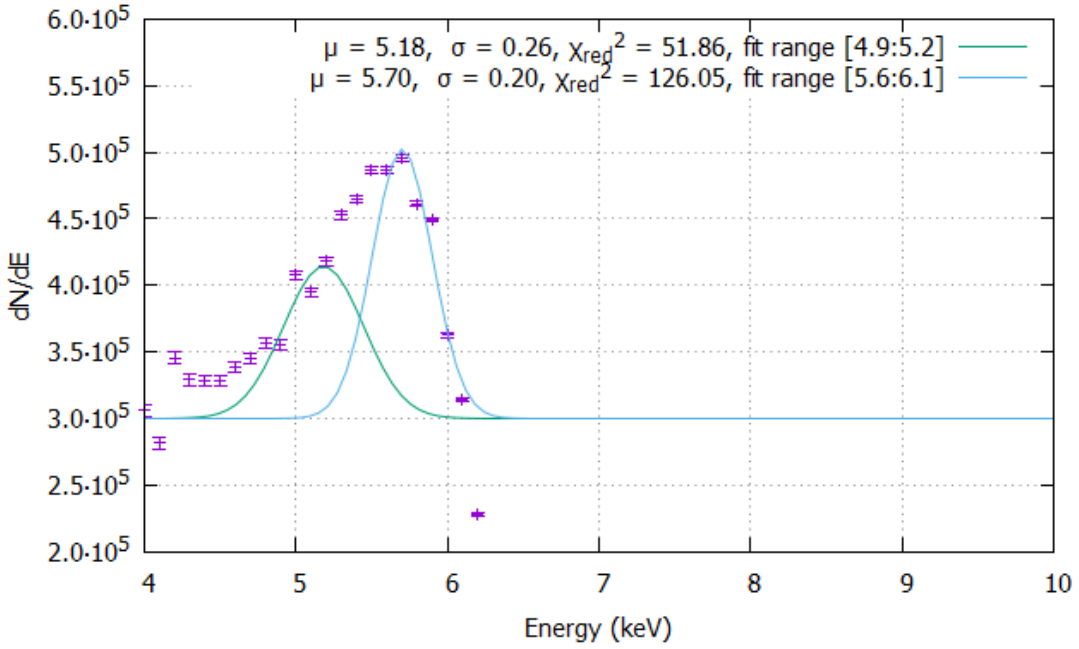

Figure A.8: The differential spectrum of ^{55}Fe, recorded with no collimator, $T_{cooler} = -15\,°C$, detector cooling off and 1 min time shutter width. Fit by two independent Gaussian distributions. A constant offset of 300,000 is added to the functions. The errorbars are plotted as well.

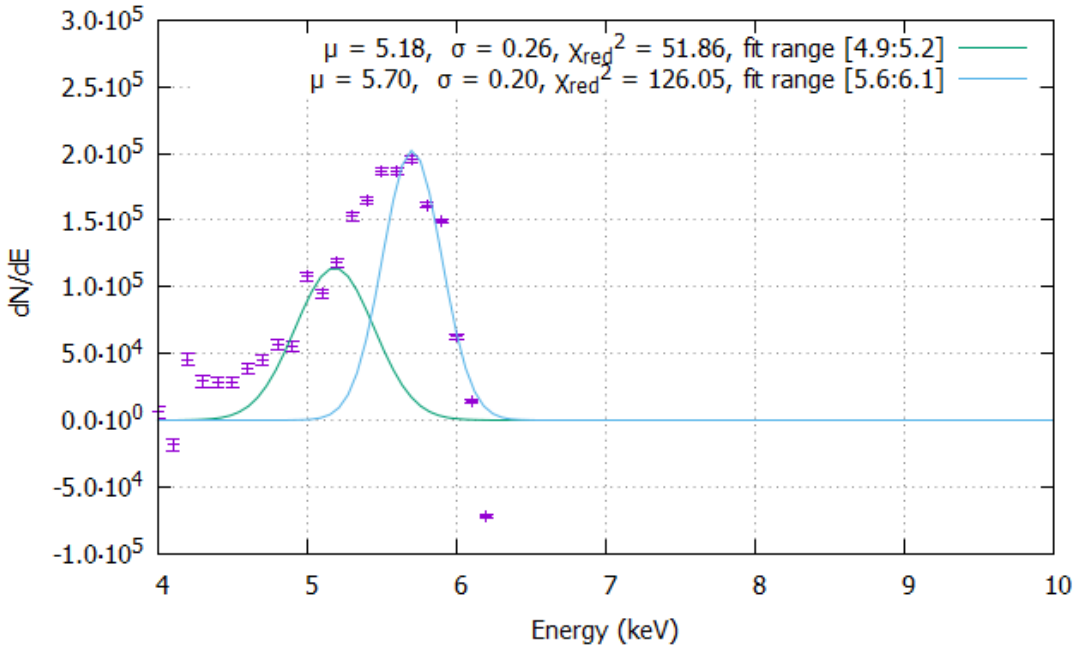

Figure A.9: The differential spectrum of ^{55}Fe, recorded with no collimator, $T_{cooler} = -15\,°C$, detector cooling off and 1 min time shutter width. Fit by two independent Gaussian distributions. A constant value of 300,000 is subtracted from the whole spectrum. The errorbars are plotted as well.

A.2 ^{55}Fe, Different Measurement Times

Table A.1: The maximum counts of the ^{55}Fe fit peak in dependence of the time shutter width are presented. Additionaly, the expected and measured percentages from the highest counts value (10 min) are shown.

shutter width (s)	counts peak	% from 10 min	% expected
10	8.22E+04 ± 2.40E+00	1.74 ± 5.06E-07	1.67
30	2.44E+05 ± 6.56E-03	5.16 ± 1.93E-09	5.00
60	4.83E+05 ± 1.29E-02	10.21 ± 3.80E-09	10.00
150	1.20E+06 ± 3.04E-02	25.30 ± 9.19E-09	25.00
300	2.38E+06 ± 6.19E-02	50.38 ± 1.85E-08	50.00
600	4.73E+06 ± 1.23E-01	100.00 ± 3.67E-08	100.00

Table A.2: Presented are the means and standard deviations of the ^{55}Fe fit peak in dependence of the time shutter width.

shutter width (s)	μ_1 (keV)	μ_2 (keV)	σ_1 (keV)	σ_2 (keV)
10	5.12 ± 0.09	5.84 ± 0.03	0.77 ± 0.04	0.34 ± 0.03
30	5.06 ± 0.09	5.82 ± 0.03	0.78 ± 0.04	0.36 ± 0.03
60	5.10 ± 0.08	5.82 ± 0.03	0.76 ± 0.03	0.35 ± 0.03
150	5.18 ± 0.05	5.84 ± 0.03	0.73 ± 0.02	0.32 ± 0.02
300	5.15 ± 0.06	5.83 ± 0.03	0.75 ± 0.03	0.34 ± 0.02
600	5.15 ± 0.08	5.83 ± 0.04	0.75 ± 0.04	0.33 ± 0.03

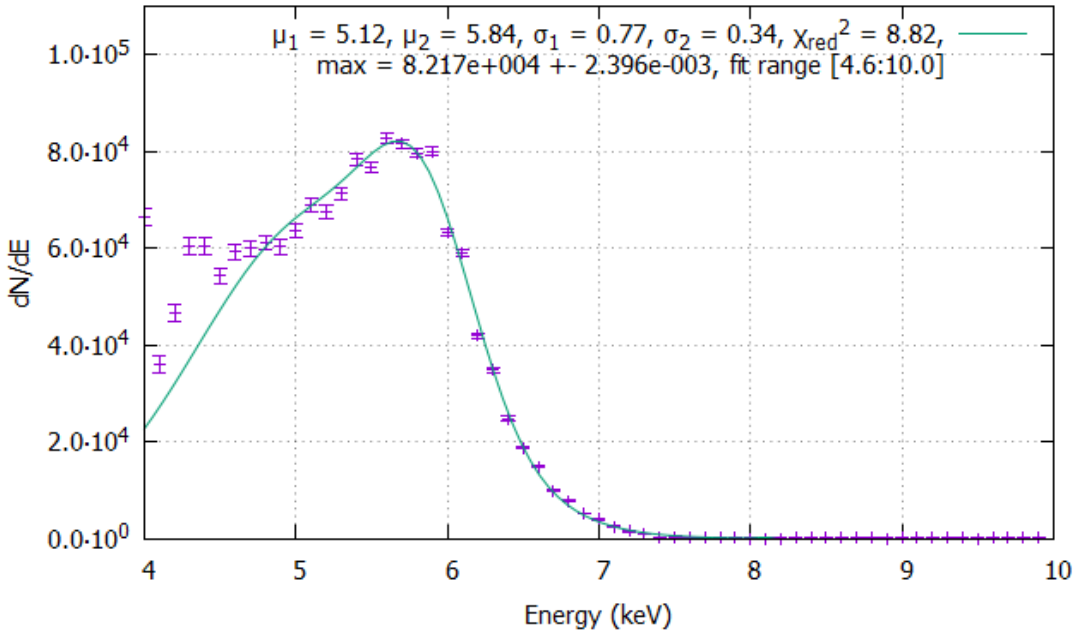

Figure A.10: The differential spectrum of ^{55}Fe, recorded with no collimator, T_{cooler} = 6 °C, $T_{detector}$ = 20 °C and 10 s time shutter width. Fit by one function composed of the addition of two Gaussian distributions with independent parameters. The errorbars are plotted as well.

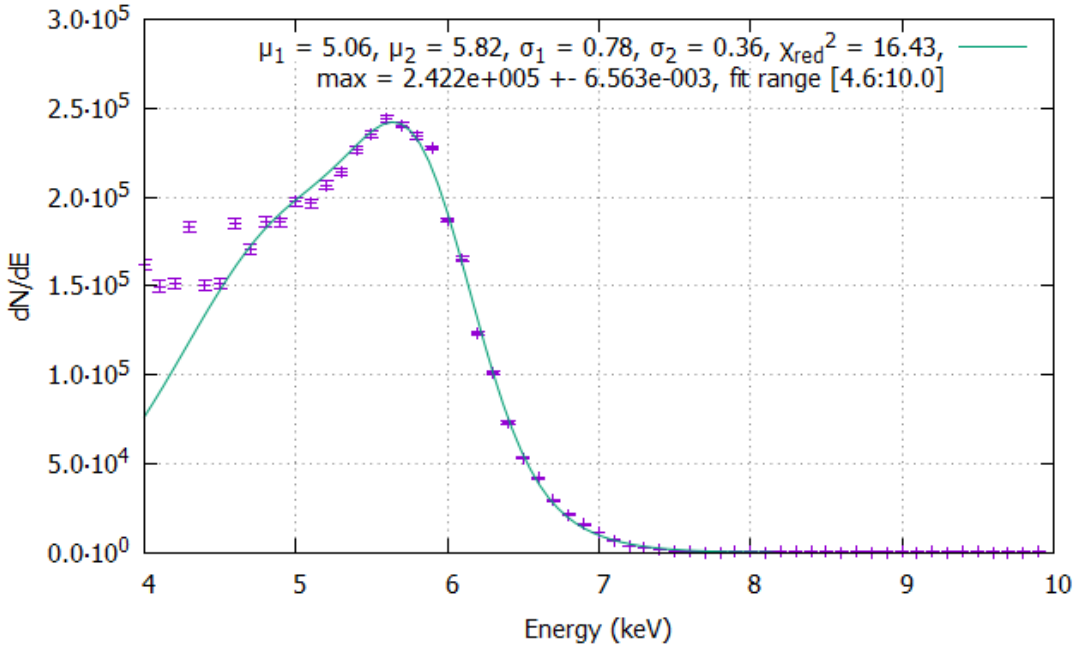

Figure A.11: The differential spectrum of ^{55}Fe, recorded with no collimator, T_{cooler} = 6 °C, $T_{detector}$ = 20 °C and 30 s time shutter width. Fit by one function composed of the addition of two Gaussian distributions with independent parameters. The errorbars are plotted as well.

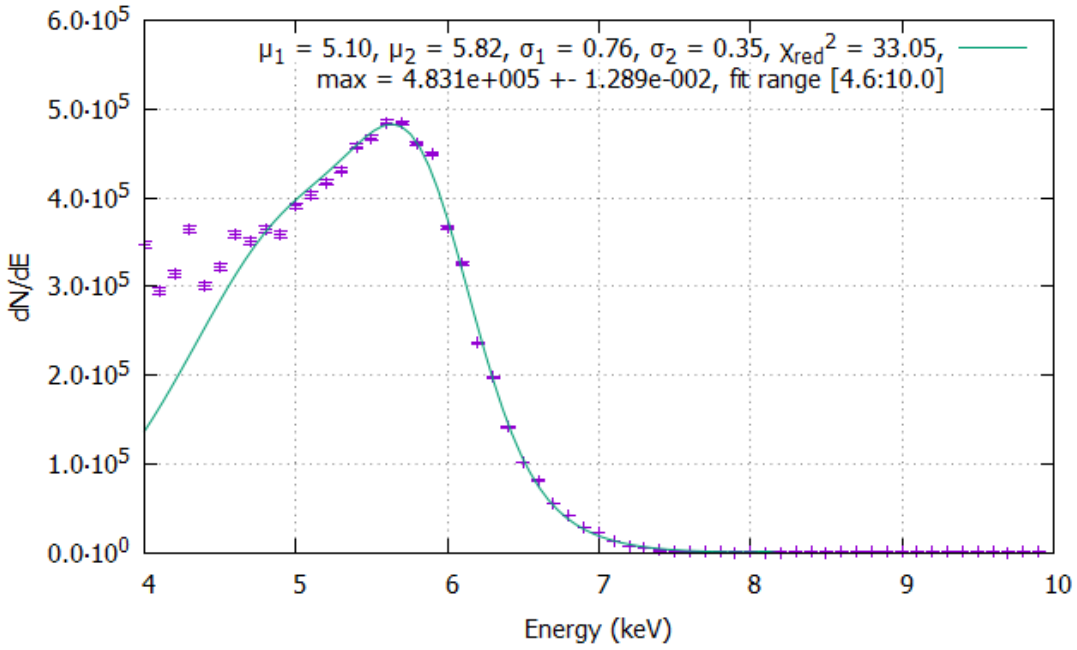

Figure A.12: The differential spectrum of ^{55}Fe, recorded with no collimator, T_{cooler} = 6 °C, $T_{detector}$ = 20 °C and 1 min time shutter width. Fit by one function composed of the addition of two Gaussian distributions with independent parameters. The errorbars are plotted as well.

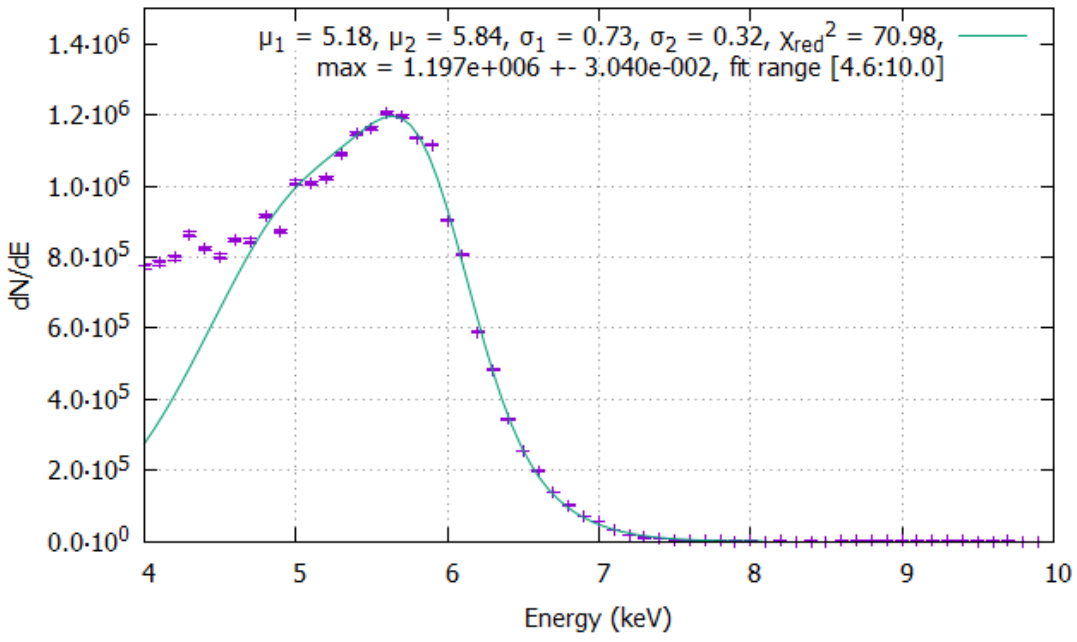

Figure A.13: The differential spectrum of ^{55}Fe, recorded with no collimator, T_{cooler} = 6 °C, $T_{detector}$ = 20 °C and 2.5 min time shutter width. Fit by one function composed of the addition of two Gaussian distributions with independent parameters. The errorbars are plotted as well.

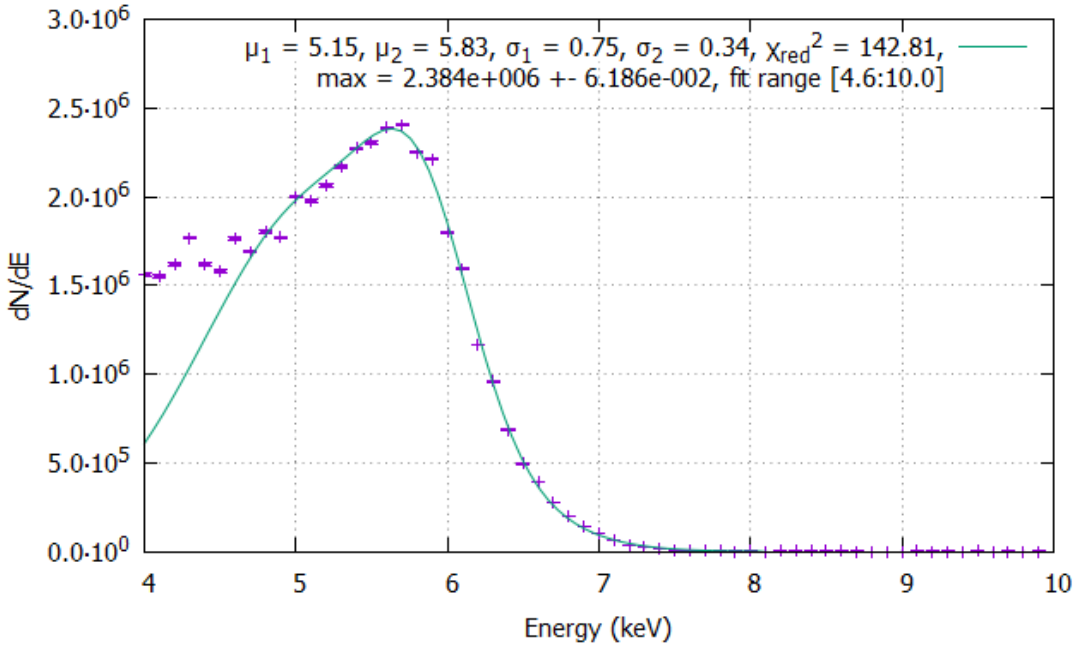

Figure A.14: The differential spectrum of ^{55}Fe, recorded with no collimator, $T_{cooler} = 6\,°C$, $T_{detector} = 20\,°C$ and 5 min time shutter width. Fit by one function composed of the addition of two Gaussian distributions with independent parameters. The errorbars are plotted as well.

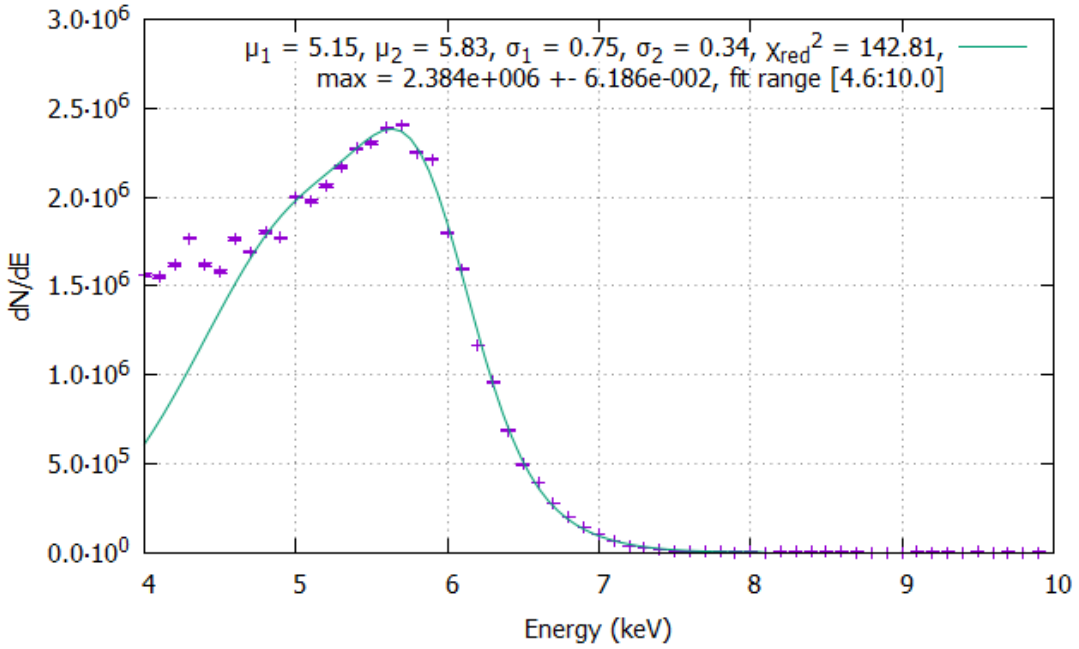

Figure A.15: The differential spectrum of ^{55}Fe, recorded with no collimator, $T_{cooler} = 6\,°C$, $T_{detector} = 20\,°C$ and 10 min time shutter width. Fit by one function composed of the addition of two Gaussian distributions with independent parameters. The errorbars are plotted as well.

A.3 ^{55}Fe, Different Temperatures

Table A.3: $Er_{1/2}$ in dependence of the detector temperature which is displayed by the LabView program.

detector temperature (°C)	Er_1	Er_2
-30	31.24 ± 0.99	12.50 ± 1.05
-20	31.24 ± 0.99	12.50 ± 1.05
-10	33.14 ± 1.27	13.63 ± 1.05
-4	32.77 ± 1.17	12.85 ± 0.98
-2	32.01 ± 2.81	12.77 ± 0.96
2	33.31 ± 1.21	13.26 ± 0.97
3	32.86 ± 1.05	12.99 ± 0.94
5	33.09 ± 1.15	13.13 ± 0.98
8	34.10 ± 1.41	13.65 ± 1.04
14	35.23 ± 1.63	14.15 ± 1.05

Table A.4: The peak counts divided by the constant counts in dependence of the detector temperature which is displayed by the LabView program.

detector temperature (°C)	peak counts	constant counts	peak/const
-30	4.65E+05 ± 1.20E-02	2.99E+05 ± 4.65E+03	1.56 ± 0.02
-20	4.94E+05 ± 1.33E-02	3.10E+05 ± 3.48E+03	1.59 ± 0.02
-10	4.89E+05 ± 1.27E-02	3.13E+05 ± 5.87E+03	1.56 ± 0.03
-4	4.96E+05 ± 1.47E-02	3.12E+05 ± 3.64E+03	1.59 ± 0.02
-2	4.93E+05 ± 1.40E-02	3.14E+05 ± 3.05E+03	1.57 ± 0.02
2	4.87E+05 ± 1.35E-02	3.13E+05 ± 3.90E+03	1.51 ± 0.03
3	4.85E+05 ± 1.25E-02	3.14E+05 ± 6.13E+03	1.54 ± 0.03
5	4.85E+05 ± 1.29E-02	3.17E+05 ± 4.94E+03	1.53 ± 0.02
8	4.84E+05 ± 1.30E-02	3.17E+05 ± 4.23E+03	1.53 ± 0.02
14	4.83E+05 ± 1.29E-02	3.21E+05 ± 5.76E+03	1.51 ± 0.03

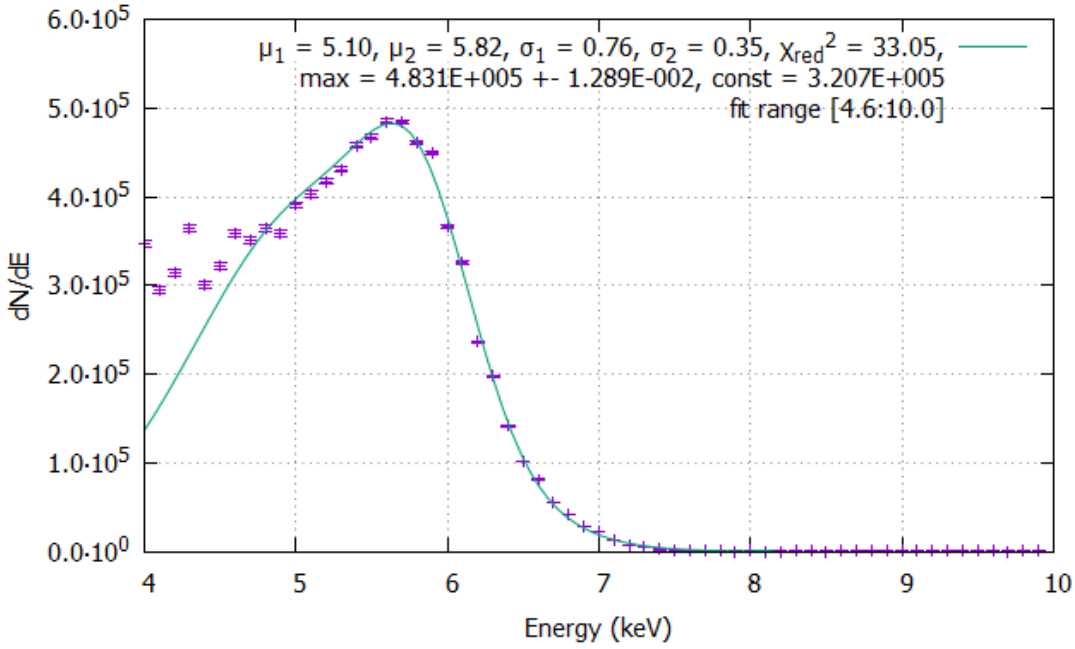

Figure A.16: The differential spectrum of ^{55}Fe, recorded with no collimator, $T_{cooler} = +6\,°C$, $T_{detector} = +20\,°C$ and 1 min time shutter width. The resulting detector temperature displayed by the software is +14 °C. Fit by one function composed of the addition of two Gaussian distributions with independent parameters. The constant value results from a constant fit in the area from 3 keV to 4 keV. The errorbars are plotted as well.

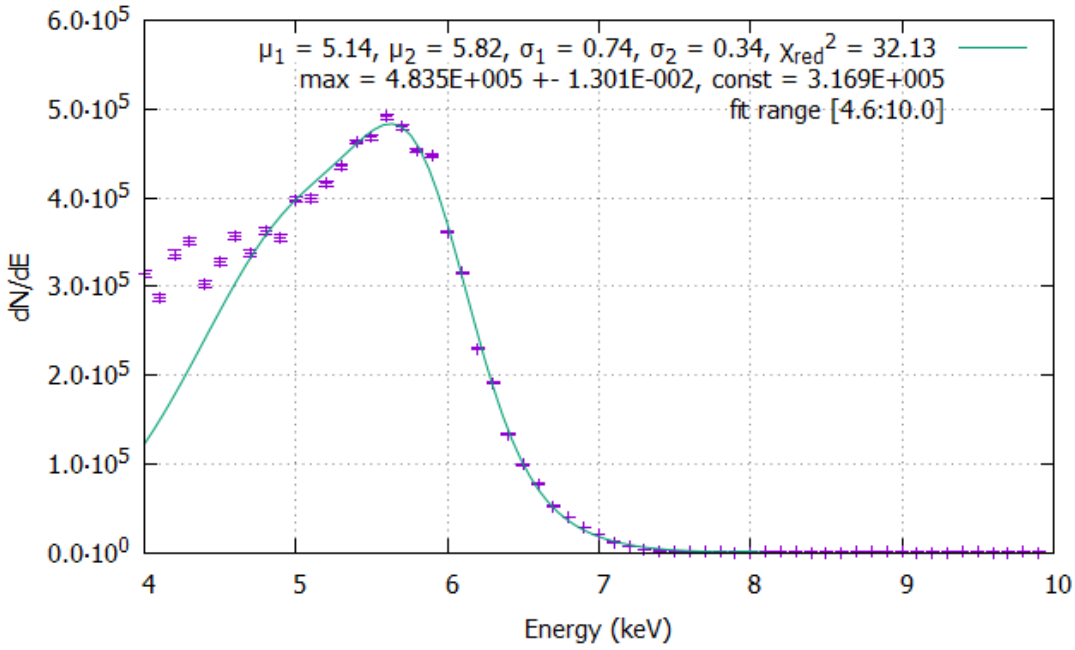

Figure A.17: The differential spectrum of ^{55}Fe, recorded with no collimator, $T_{cooler} = -4\,°C$, $T_{detector} = +20\,°C$ and 1 min time shutter width. The resulting detector temperature displayed by the software is $+8\,°C$. Fit by one function composed of the addition of two Gaussian distributions with independent parameters. The constant value results from a constant fit in the area from 3 keV to 4 keV. The errorbars are plotted as well.

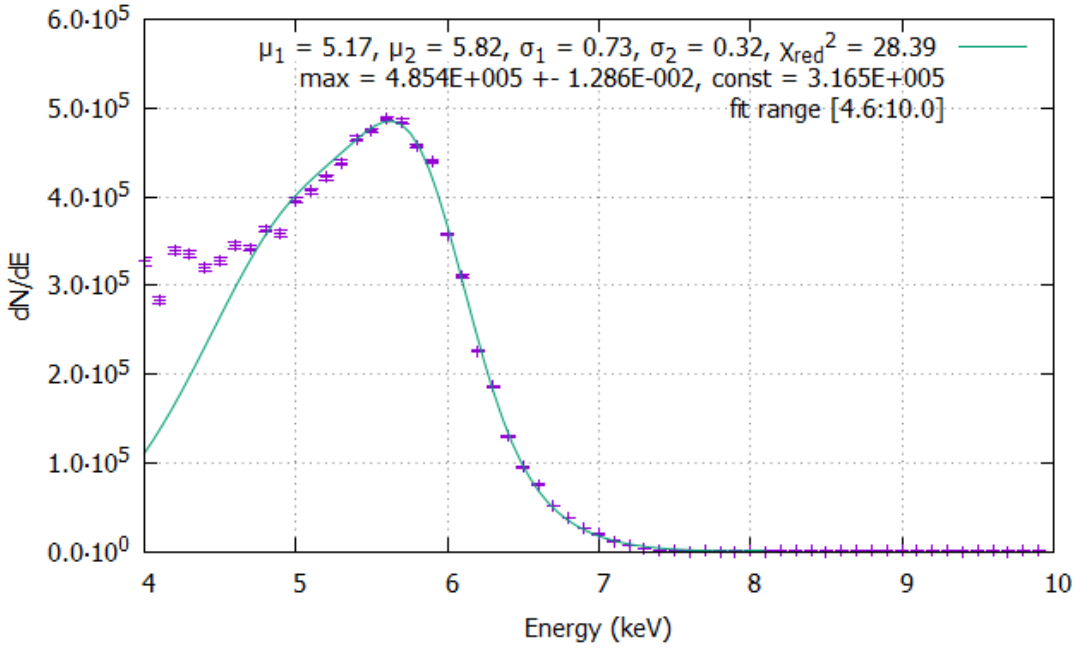

Figure A.18: The differential spectrum of ^{55}Fe, recorded with no collimator, $T_{cooler} = -8\,°C$, $T_{detector} = +20\,°C$ and 1 min time shutter width. The resulting detector temperature displayed by the software is +5 °C. Fit by one function composed of the addition of two Gaussian distributions with independent parameters. The constant value results from a constant fit in the area from 3 keV to 4 keV. The errorbars are plotted as well.

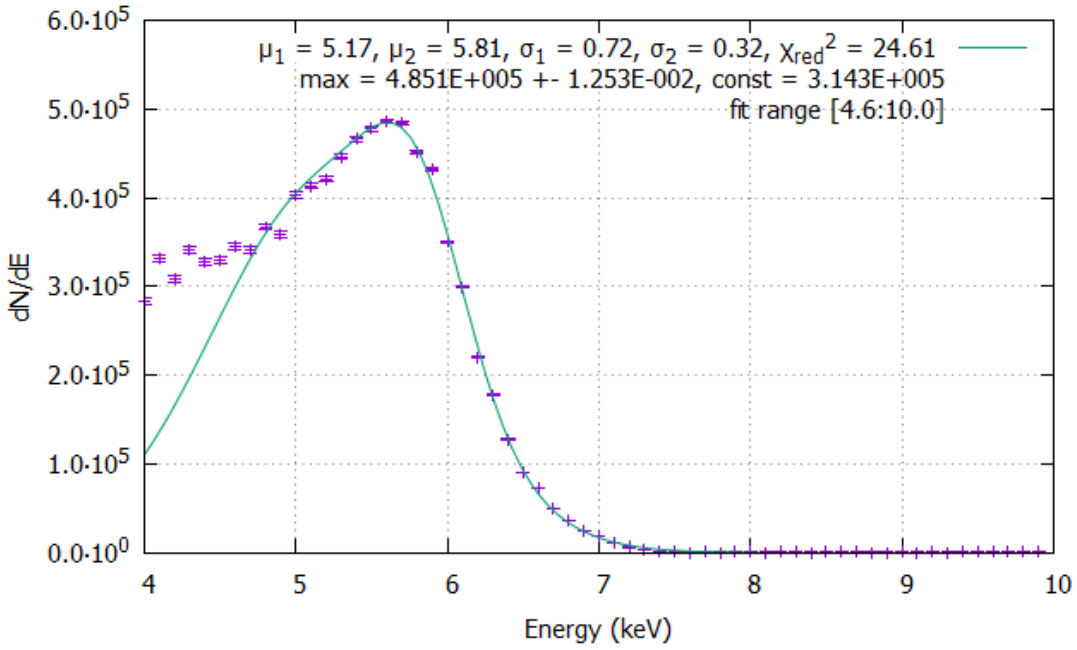

Figure A.19: The differential spectrum of ^{55}Fe, recorded with no collimator, $T_{cooler} = -12\,°C$, $T_{detector} = +20\,°C$ and 1 min time shutter width. The resulting detector temperature displayed by the software is +3 °C. Fit by one function composed of the addition of two Gaussian distributions with independent parameters. The constant value results from a constant fit in the area from 3 keV to 4 keV. The errorbars are plotted as well.

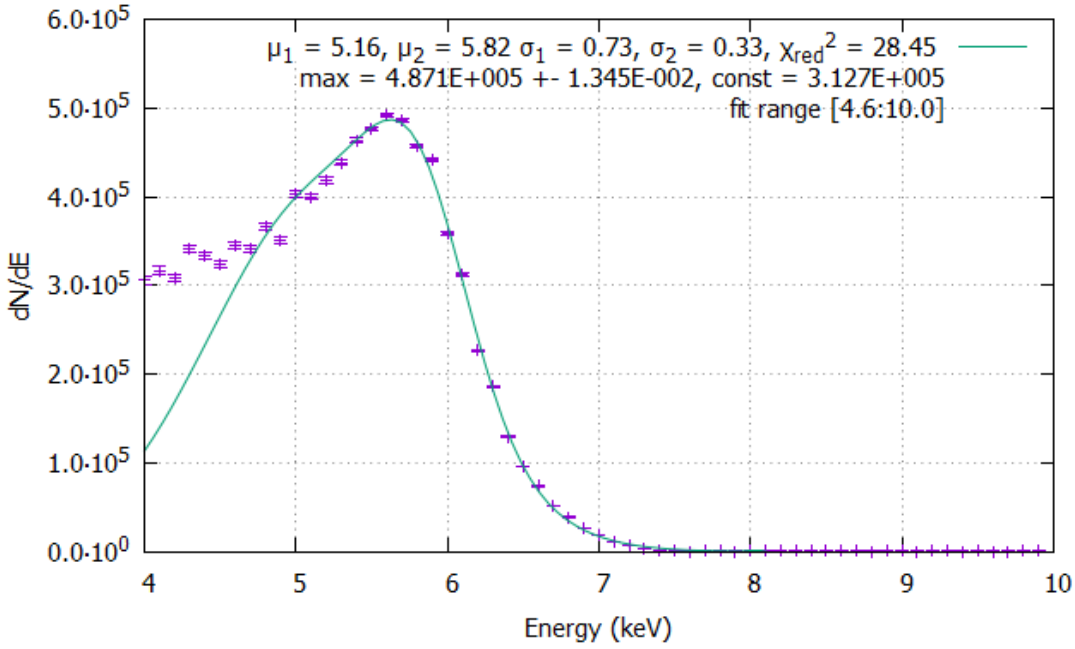

Figure A.20: The differential spectrum of ^{55}Fe, recorded with no collimator, $T_{cooler} = -10\,°C$, detector cooling off and 1 min time shutter width. The resulting detector temperature displayed by the software is $+2\,°C$. Fit by one function composed of the addition of two Gaussian distributions with independent parameters. The constant value results from a constant fit in the area from 3 keV to 4 keV. The errorbars are plotted as well.

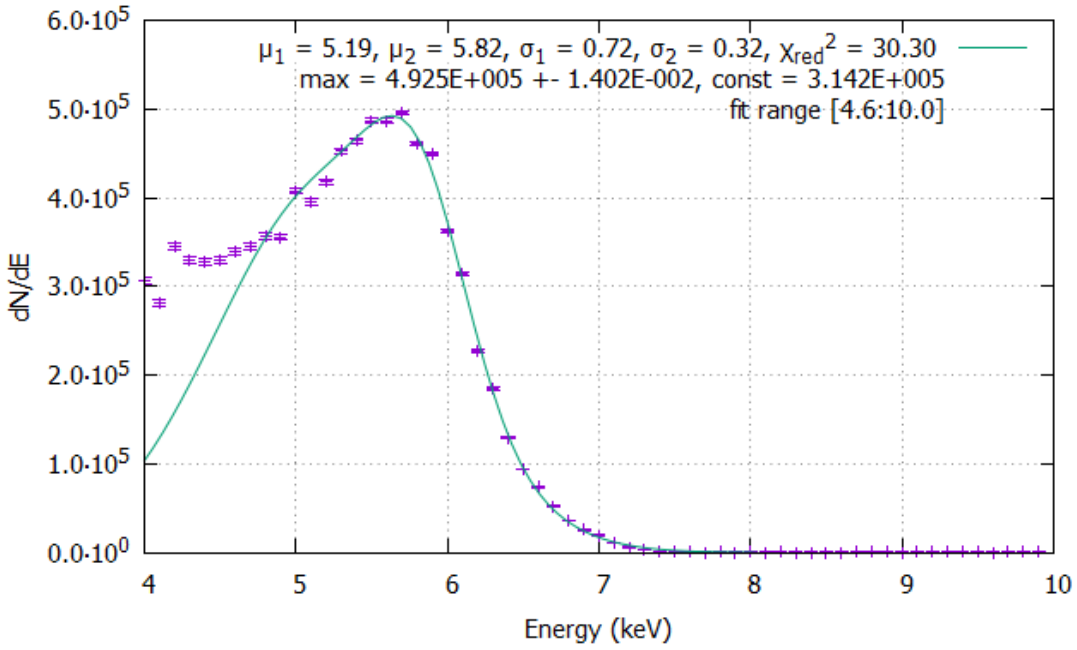

Figure A.21: The differential spectrum of ^{55}Fe, recorded with no collimator, $T_{cooler} = -15\,°C$, detector cooling off and 1 min time shutter width. The resulting detector temperature displayed by the software is -2 °C. Fit by one function composed of the addition of two Gaussian distributions with independent parameters. The constant value results from a constant fit in the area from 3 keV to 4 keV. The errorbars are plotted as well.

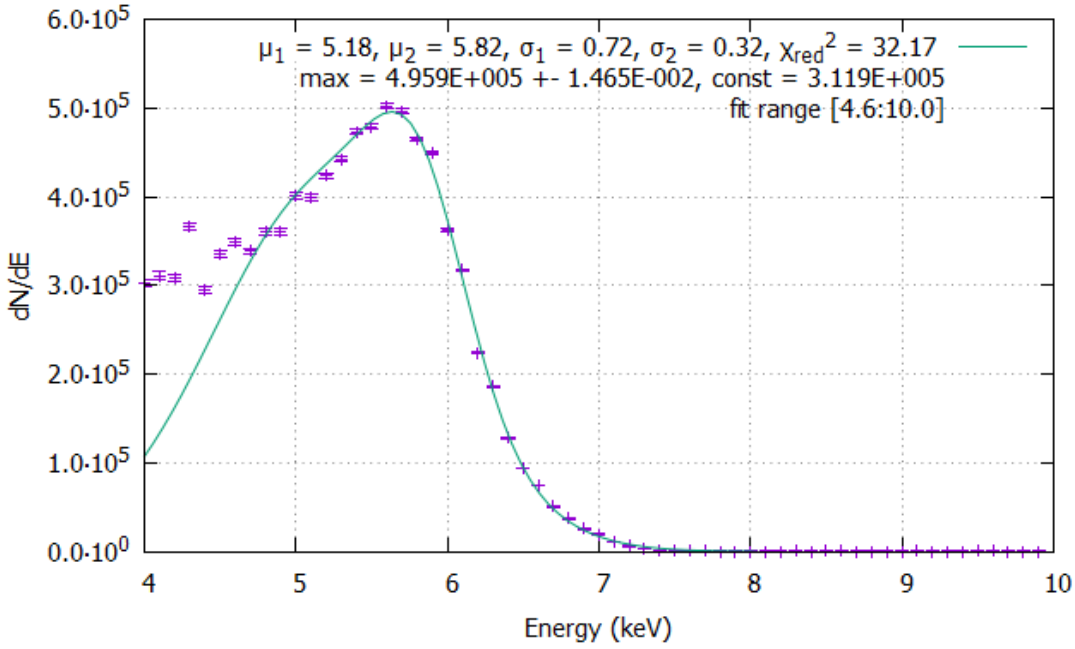

Figure A.22: The differential spectrum of ^{55}Fe, recorded with no collimator, $T_{cooler} = -19\,°C$, detector cooling off and 1 min time shutter width. The resulting detector temperature displayed by the software is -4 °C. Fit by one function composed of the addition of two Gaussian distributions with independent parameters. The constant value results from a constant fit in the area from 3 keV to 4 keV. The errorbars are plotted as well.

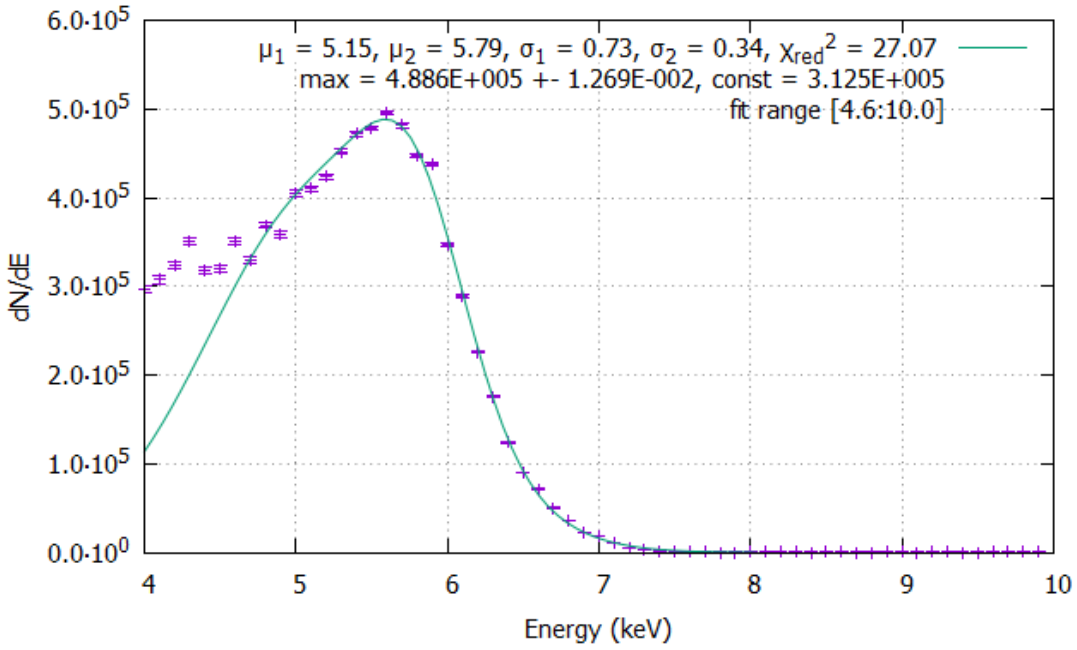

Figure A.23: The differential spectrum of ^{55}Fe, recorded with no collimator, $T_{cooler} = -19\,°C$, $T_{detector} = -10\,°C$ and 1 min time shutter width. The resulting detector temperature displayed by the software is -10 °C. Fit by one function composed of the addition of two Gaussian distributions with independent parameters. The constant value results from a constant fit in the area from 3 keV to 4 keV. The errorbars are plotted as well.

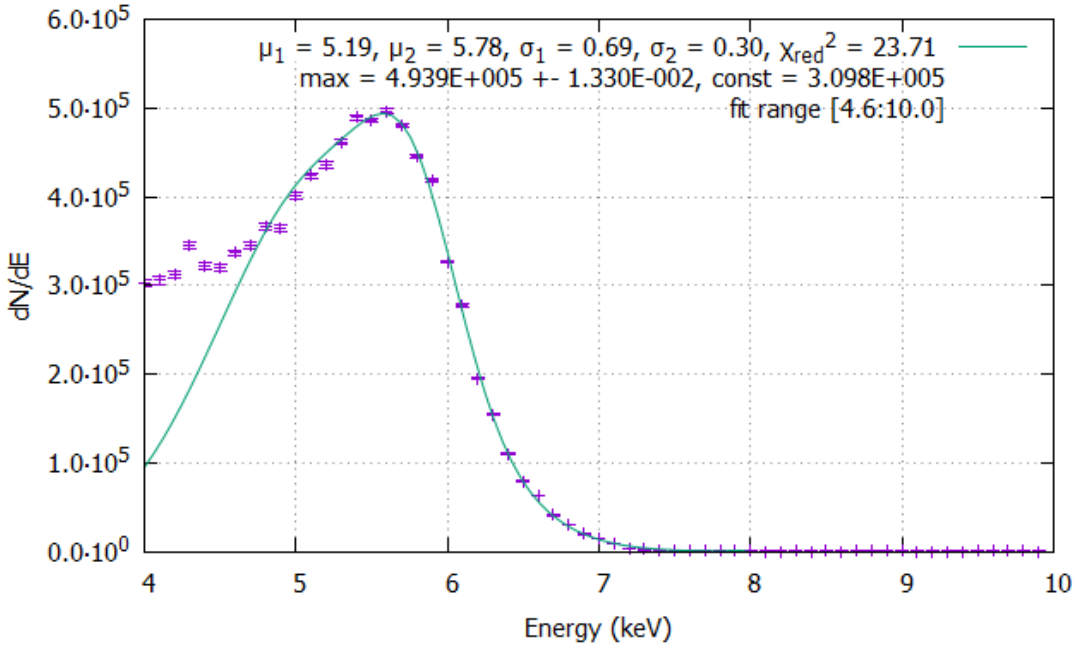

Figure A.24: The differential spectrum of ^{55}Fe, recorded with no collimator, $T_{cooler} = -19\,°C$, $T_{detector} = -20\,°C$ and 1 min time shutter width. The resulting detector temperature displayed by the software is -20 °C. Fit by one function composed of the addition of two Gaussian distributions with independent parameters. The constant value results from a constant fit in the area from 3 keV to 4 keV. The errorbars are plotted as well.

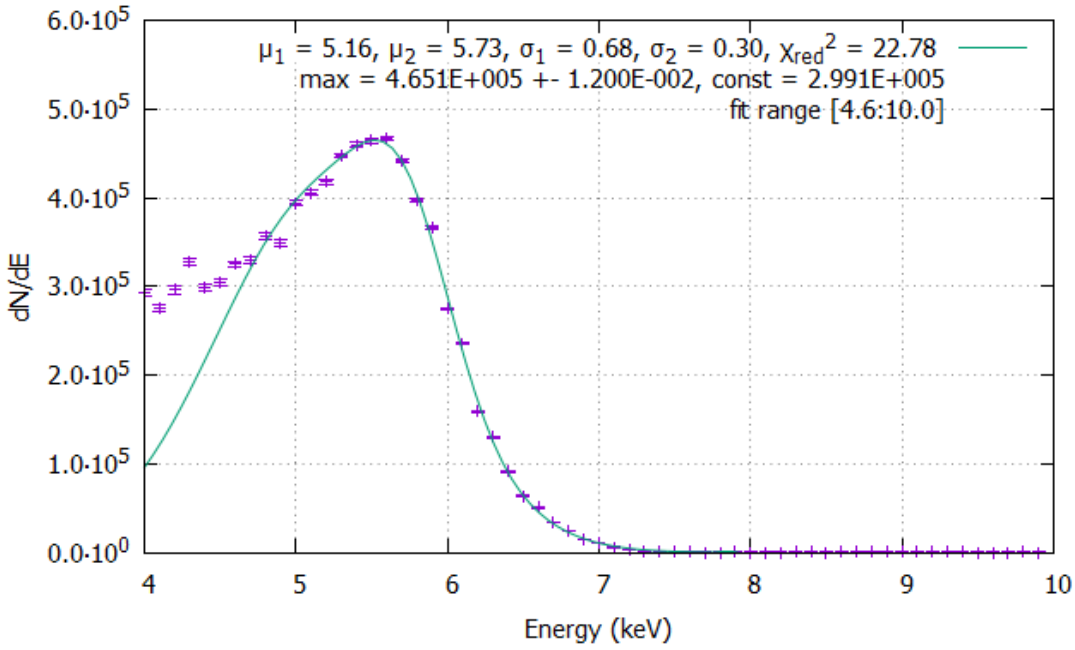

Figure A.25: The differential spectrum of ^{55}Fe, recorded with no collimator, $T_{cooler} = -19\,°C$, $T_{detector} = -30\,°C$ and 1 min time shutter width. The resulting detector temperature displayed by the software is -30 °C. Fit by one function composed of the addition of two Gaussian distributions with independent parameters. The constant value results from a constant fit in the area from 3 keV to 4 keV. The errorbars are plotted as well.

A.4 ^{241}Am

Table A.5: Presented are the means of the Gaussian distributions, which are used to fit the ^{241}Am peaks, in subject of the energy step width.

energy step (keV)	μ_1 (keV)	μ_2 (keV)	μ_3 (keV)	μ_4 (keV)	μ_5 (keV)
0.1	21.70 ± 0.43	25.57 ± 1.74	31.69 ± 0.43	35.04 ± 1.34	58.72 ± 0.10
0.2	21.39 ± 0.47	25.69 ± 0.60	31.63 ± 0.29	35.71 ± 0.49	58.71 ± 0.08
0.5	21.36 ± 0.22	25.99 ± 1.41	31.31 ± 0.46	35.59 ± 0.39	58.48 ± 0.09
1.0		24.08 ± 1.31	31.17 ± 0.34	35.09 ± 0.16	58.13 ± 0.13

Table A.6: Presented are the standard derivations of the Gaussian distributions, which are used to fit the ^{241}Am peaks, in subject of the energy step width.

energy step (keV)	σ_1 (keV)	σ_2 (keV)	σ_3 (keV)	σ_4 (keV)	σ_5 (keV)
0.1	3.38 ± 0.73	3.57 ± 3.13	2.67 ± 0.94	2.94 ± 1.09	1.67 ± 0.06
0.2	3.55 ± 0.68	3.18 ± 1.08	2.75 ± 0.61	2.33 ± 0.70	1.65 ± 0.05
0.5	3.42 ± 0.31	3.54 ± 1.66	3.38 ± 0.89	2.28 ± 0.48	1.67 ± 0.06
1.0		4.52 ± 1.24	2.99 ± 0.52	2.46 ± 0.20	1.74 ± 0.08

B Bibliography

[1] GSI Helmholtzzentrum fuer Schwerionenforschung GmbH. Compressed baryonic matter (cbm). https://www.gsi.de/work/forschung/cbmnqm/cbm.htm. visited 8.30.2016.

[2] Johannes Wessels. Kern- und Teilchenphysik 1. Vorlesungsskript, WS 14/15. WWU Mnster.

[3] E.S. Yang. *Fundamentals of Semiconductor Devices*. McGraw-Hill, New York, 1978.

[4] Glossary of Nanotechnology and related Terms. energy-band theory. http://eng.thesaurus.rusnano.com/upload/iblock/f44/ksezritsyykd%20nuukxfwdaxyg1.jpg. visited 8.30.2016.

[5] HyperPhysics. Bands for doped semiconductors. http://hyperphysics.phy-astr.gsu.edu/hbase/solids/imgsol/dban.gif. visited 8.30.2016.

[6] Pixirad Imaging Counters s.r.l. *Pixirad-1 User Manual*. Pixirad Imaging Counters s.r.l., sez. Pisa Largo B. Pontecorvo, 3 56127 Pisa (Italy), 4 2013.

[7] V. Chist M. B55 fe. http://www.nucleide.org/DDEP_WG/Nuclides/Fe-55_tables.pdf, 2006. visited 8.30.2016.

[8] Pixirad Imaging Counters s.r.l. Pixirad website. http://www.pixirad.com/, 2016. visited 8.30.2016.

[9] N. K. Kuzmenko V. P. Chechev. 241 am. http://www.nucleide.org/DDEP_WG/Nuclides/Am-241_tables.pdf, 2010. visited 8.30.2016.

Originality Statement

I hereby certify that I am the sole author of this thesis and that no part of this thesis has been published or submitted for publication.

I certify that, to the best of my knowledge, my thesis does not infringe upon anyone's copyright nor violate and proprietary rights and that any ideas, techniques, quotations, or any other material from the work of other people included in my thesis, published or otherwise, are fully acknowledged in accordance with the standard referencing practices.

Münster, September 19, 2016

.....
(Johannes Beckhoff)